



AFRL-OSR-VA-TR-2015-0147

---

## Nano-Zirconium Tungstate Reinforced Liquid Crystalline Thermosetting with Near

Kristen Constant  
IOWA STATE UNIVERSITY

---

06/25/2015  
Final Report

DISTRIBUTION A: Distribution approved for public release.

Air Force Research Laboratory  
AF Office Of Scientific Research (AFOSR)/ RTD  
Arlington, Virginia 22203  
Air Force Materiel Command

<b>REPORT DOCUMENTATION PAGE</b>					<i>Form Approved</i> OMB No. 0704-0188	
<small>The public reporting burden for this collection of information is estimated to average 1 hour per response, including the time for reviewing instructions, searching existing data sources, gathering and maintaining the data needed, and completing and reviewing the collection of information. Send comments regarding this burden estimate or any other aspect of this collection of information, including suggestions for reducing the burden, to the Department of Defense, Executive Service Directorate (0704-0188). Respondents should be aware that notwithstanding any other provision of law, no person shall be subject to any penalty for failing to comply with a collection of information if it does not display a currently valid OMB control number.</small>						
<b>PLEASE DO NOT RETURN YOUR FORM TO THE ABOVE ORGANIZATION.</b>						
1. REPORT DATE (DD-MM-YYYY) 05-18-2015		2. REPORT TYPE Final Technical Report			3. DATES COVERED (From - To) 03/15/2012 to 03/14/2015	
4. TITLE AND SUBTITLE  Nano-Zirconium Tungstate Reinforced Liquid Crystalline Thermosetting Composites with Near Zero Thermal Expansion					5a. CONTRACT NUMBER	
					5b. GRANT NUMBER FA9550-12-1-0108	
					5c. PROGRAM ELEMENT NUMBER	
6. AUTHOR(S)  Dr. Michael R. Kessler and Dr. Yuzhan Li					5d. PROJECT NUMBER	
					5e. TASK NUMBER	
					5f. WORK UNIT NUMBER	
7. PERFORMING ORGANIZATION NAME(S) AND ADDRESS(ES) Washington State University, Pullman, WA 99164-2920 & Iowa State University, Ames, IA 50011					8. PERFORMING ORGANIZATION REPORT NUMBER	
9. SPONSORING/MONITORING AGENCY NAME(S) AND ADDRESS(ES) USAF, AFRL DUNS 143574726 AF OFFICE OF SCIENTIFIC RESEARCH 875 N. RANDOLPH ST. ROOM 3112 ARLINGTON VA 22203					10. SPONSOR/MONITOR'S ACRONYM(S)  AFOSR	
					11. SPONSOR/MONITOR'S REPORT NUMBER(S)	
12. DISTRIBUTION/AVAILABILITY STATEMENT Distribution A - Approved for Public Release						
13. SUPPLEMENTARY NOTES						
14. ABSTRACT One crucial factor limiting the performance of polymer matrix composites is their relatively high coefficient of thermal expansion (CTE), which impacts the dimensional stability of these materials. This report described the synthesis and characterization of zirconium tungstate (ZrW <sub>2</sub> O <sub>8</sub> ) nanoparticles with negative CTE and their applications in an epoxy resin to produce low CTE nanocomposites. This work also described the synthesis and characterization of a unique class of thermosets known as liquid crystalline epoxy resins (LCERs) for the development of advanced polymer matrices for high performance composites. Results showed that it was possible to control structure and the resulting functionality of the LCERs by curing the synthesized epoxy monomer with appropriate curing agents. Highly crosslinked LCERs exhibited a self-reinforcing effect because of the self-organized liquid crystalline phase and are promising candidates for the polymer matrices in structural composites. Lightly crosslinked LCERs exhibited a triple shape memory effect and are excellent candidates for the development of multifunctional polymer composites.						
15. SUBJECT TERMS Composite Materials, Thermal Expansion, Zirconium Tungstate, Liquid Crystalline Epoxy Resin						
16. SECURITY CLASSIFICATION OF:			17. LIMITATION OF ABSTRACT	18. NUMBER OF PAGES	19a. NAME OF RESPONSIBLE PERSON	
a. REPORT	b. ABSTRACT	c. THIS PAGE			Michael R. Kessler	
U	U	U	UU	107	19b. TELEPHONE NUMBER (Include area code) 509-335-8654	

Reset

## INSTRUCTIONS FOR COMPLETING SF 298

**1. REPORT DATE.** Full publication date, including day, month, if available. Must cite at least the year and be Year 2000 compliant, e.g. 30-06-1998; xx-06-1998; xx-xx-1998.

**2. REPORT TYPE.** State the type of report, such as final, technical, interim, memorandum, master's thesis, progress, quarterly, research, special, group study, etc.

**3. DATES COVERED.** Indicate the time during which the work was performed and the report was written, e.g., Jun 1997 - Jun 1998; 1-10 Jun 1996; May - Nov 1998; Nov 1998.

**4. TITLE.** Enter title and subtitle with volume number and part number, if applicable. On classified documents, enter the title classification in parentheses.

**5a. CONTRACT NUMBER.** Enter all contract numbers as they appear in the report, e.g. F33615-86-C-5169.

**5b. GRANT NUMBER.** Enter all grant numbers as they appear in the report, e.g. AFOSR-82-1234.

**5c. PROGRAM ELEMENT NUMBER.** Enter all program element numbers as they appear in the report, e.g. 61101A.

**5d. PROJECT NUMBER.** Enter all project numbers as they appear in the report, e.g. 1F665702D1257; ILIR.

**5e. TASK NUMBER.** Enter all task numbers as they appear in the report, e.g. 05; RF0330201; T4112.

**5f. WORK UNIT NUMBER.** Enter all work unit numbers as they appear in the report, e.g. 001; AFAPL30480105.

**6. AUTHOR(S).** Enter name(s) of person(s) responsible for writing the report, performing the research, or credited with the content of the report. The form of entry is the last name, first name, middle initial, and additional qualifiers separated by commas, e.g. Smith, Richard, J, Jr.

**7. PERFORMING ORGANIZATION NAME(S) AND ADDRESS(ES).** Self-explanatory.

**8. PERFORMING ORGANIZATION REPORT NUMBER.** Enter all unique alphanumeric report numbers assigned by the performing organization, e.g. BRL-1234; AFWL-TR-85-4017-Vol-21-PT-2.

**9. SPONSORING/MONITORING AGENCY NAME(S) AND ADDRESS(ES).** Enter the name and address of the organization(s) financially responsible for and monitoring the work.

**10. SPONSOR/MONITOR'S ACRONYM(S).** Enter, if available, e.g. BRL, ARDEC, NADC.

**11. SPONSOR/MONITOR'S REPORT NUMBER(S).** Enter report number as assigned by the sponsoring/monitoring agency, if available, e.g. BRL-TR-829; -215.

**12. DISTRIBUTION/AVAILABILITY STATEMENT.** Use agency-mandated availability statements to indicate the public availability or distribution limitations of the report. If additional limitations/ restrictions or special markings are indicated, follow agency authorization procedures, e.g. RD/FRD, PROPIN, ITAR, etc. Include copyright information.

**13. SUPPLEMENTARY NOTES.** Enter information not included elsewhere such as: prepared in cooperation with; translation of; report supersedes; old edition number, etc.

**14. ABSTRACT.** A brief (approximately 200 words) factual summary of the most significant information.

**15. SUBJECT TERMS.** Key words or phrases identifying major concepts in the report.

**16. SECURITY CLASSIFICATION.** Enter security classification in accordance with security classification regulations, e.g. U, C, S, etc. If this form contains classified information, stamp classification level on the top and bottom of this page.

**17. LIMITATION OF ABSTRACT.** This block must be completed to assign a distribution limitation to the abstract. Enter UU (Unclassified Unlimited) or SAR (Same as Report). An entry in this block is necessary if the abstract is to be limited.

Nano-Zirconium Tungstate Reinforced Liquid Crystalline Thermosetting Composites  
with Near Zero Thermal Expansion

Michael R. Kessler and Yuzhan Li

School of Mechanical and Materials Engineering

Washington State University

201 Sloan Hall

Pullman, WA 99164-2920

Phone: 509-335-8654

Email: [michaelr.kessler@wsu.edu](mailto:michaelr.kessler@wsu.edu)



## **Index**

Abstract/Executive Summary

Chapter 1: Introduction

Chapter 2: Synthesis and characterization of Zirconium Tungstate Nanoparticles with Different Morphology and Negative Thermal Expansivity

Chapter 3: Zirconium Tungstate Nanoparticles Reinforced Epoxy Nanocomposites with Tailored Thermal Expansivity

Chapter 4: Synthesis and Characterization of Highly Crosslinked, Self-reinforcing Liquid Crystalline Epoxy Resins

Chapter 5: Magnetic Field Processing of Highly Crosslinked Liquid Crystalline Epoxy Resins with tailor thermomechanical properties

Chapter 6: Synthesis and Characterization of Lightly Crosslinked Liquid Crystalline Epoxy Resins with Tunable Shape Memory Behavior

Chapter 7: Summary

References

## **Abstract/Executive Summary**

One crucial factor limiting the performance of polymer matrix composites is their relatively high coefficient of thermal expansion (CTE), which impacts the dimensional stability of these materials. This report described the synthesis and characterization of zirconium tungstate ( $\text{ZrW}_2\text{O}_8$ ) nanoparticles with negative CTE and their applications in an epoxy resin to produce low CTE nanocomposites. This work also described the synthesis and characterization of a unique class of thermosets known as liquid crystalline epoxy resins (LCERs) for the development of advanced polymer matrices for high performance composites. Results showed that it was possible to control structure and the resulting functionality of the LCERs by curing the synthesized epoxy monomer with appropriate curing agents. Highly crosslinked LCERs exhibited a self-reinforcing effect because of the self-organized liquid crystalline phase and are promising candidates for the polymer matrices in structural composites. Lightly crosslinked LCERs exhibited a triple shape memory effect and are excellent candidates for the development of multifunctional polymer composites.

## **Cumulative Lists of People Involved in the Research Effort**

1. Michael R. Kessler
2. Yuzhan Li
3. Hongchao Wu

## **Publications Stemming From the Research Effort**

### **Journal Articles**

1. H. Wu, P. Badrinarayanan, M. R. Kessler, "Effect of Hydrothermal Synthesis Conditions on the Morphology and Negative Thermal Expansivity of Zirconium Tungstate Nanoparticles", *Journal of the American Ceramic Society*, 2012, 95(11), 3643-3650.
2. Y. Li, P. Badrinarayana, M. R. Kessler, "Liquid Crystalline Epoxy Resin Based on Biphenyl Mesogen: Thermal Characterization", *Polymer*, 2013, 54(12), 3017-3025.
3. Y. Li, M. R. Kessler, "Liquid Crystalline Epoxy Resin Based on Bisphenol Mesogen: Effect of Magnetic Field Orientation during Cure", *Polymer*, 2013, 54 (21), 5742-5746.
4. H. Wu, M. Rogalski, M. R. Kessler, "Zirconium Tungstate/Epoxy Nanocomposites: Effect of Nanoparticle Morphology and Negative Thermal Expansivity", *ACS Applied Materials and Interfaces*, 2013, 5(19), 9478-9487.

5. Y. Li, M. R. Kessler, "Cure Kinetics of Liquid Crystalline Epoxy Resins Based on Biphenyl Mesogen", *Journal of Thermal Analysis and Calorimetry*, 2014, 117(1), 481-488.
6. Y. Li, M. R. Kessler, "Creep-resistant behavior of self-reinforcing liquid crystalline epoxy resins", *Polymer*, 2014, 55(8), 2021-2027.
7. Y. Li, O. Rios, M. R. Kessler, "Thermomagnetic Processing of Liquid Crystalline Epoxy Resins and Their Mechanical Characterization Using Nanoindentation", *ACS Applied Materials and Interfaces*, 2014, 6(21), 19456-19464.
8. Y. Li, C. Pruitt, O. Rios, L. Wei, M. Rock, J. K. Keum, A. G. McDonald, M. R. Kessler, "Controlled Shape Memory Behavior of a Smectic Main-chain Liquid Crystalline Elastomer", *Macromolecules*, 2015, 48(9), 2864-2874.

#### Invited Workshop Presentations

#### Conference Proceedings

1. Y. Li, M. R. Kessler, and P. Badrinarayanan, "Thermal Characterization of Liquid Crystalline Epoxy Resins", Proceedings of the North American Thermal Analysis Society Annual Conference (NATAS 2011). Aug. 7-10, 2011. Des Moines, IA.
2. H. Wu, P. Badrinarayanan, and M. R. Kessler, "Hydrothermal synthesis of zirconium tungstate nanoparticles with various morphologies and size scales", Proceedings of the North American Thermal Analysis Society Annual Conference (NATAS 2011). Aug. 7-10, 2011. Des Moines, IA.
3. Y. Li, M. R. Kessler, "Thermal analysis and structure characterization of liquid crystalline epoxy resins cured in a magnetic field", Proceedings of the North American Thermal Analysis Society Annual Conference (NATAS 2013). Aug. 4-7, 2013. Bowling Green, KY.

## Chapter 1: Introduction

### 1.1 Project Motivation

Polymer matrix composites (PMCs) are enabling technologies in a wide variety of engineering and structural applications because of their unique combination of low density and high strength. However, one crucial factor limiting the use of PMCs in high performance applications is their relatively high coefficient of thermal expansion (CTE), which impacts the dimensional stability of these materials especially at temperatures in the vicinity of the glass transition temperature ( $T_g$ ) of the polymer matrix. Consequently, when PMCs are used in applications such as dimensionally stable mirrors, apertures, telescope components, or microelectronics, residual stresses may be induced due to their contact with substrates or surfaces with lower values of CTE, such as silicon, alumina, and glass. Hence, the ability to tailor the CTE of the polymer phase in PMCs can enable mitigation of residual stresses in these composites, which in turn would enhance their versatility and service lifetimes. This report describes the synthesis and characterization of zirconium tungstate ( $\text{ZrW}_2\text{O}_8$ ) nanoparticles with negative thermal expansion (NTE) behavior and their applications in an epoxy resin to produce nanocomposites with low thermal expansion. This work also describes the synthesis and characterization of a unique class of polymer matrices known as liquid crystalline epoxy resins (LCERs) for the development of multifunctional composites.

### 1.2 Zirconium Tungstate Nanoparticles

NTE materials exhibit contraction in volume upon heating within certain temperature ranges.  $\text{ZrW}_2\text{O}_8$  has been studied extensively because of its strong and isotropic negative thermal expansion behavior over a broad temperature range (from 0.3 to 1050 K) with a reversible order-disordered transition from the  $\alpha$ -phase ( $P2_13$  space group) to the  $\beta$ -phase ( $Pa-3$  space group) at 430 K, and an irreversible transition between the  $\alpha$ -phase and the  $\gamma$ -phase ( $P2_12_12_1$  space group) under pressures above 0.2 GPa. The NTE behavior of  $\text{ZrW}_2\text{O}_8$  is caused by the transverse vibration of oxygen atoms linking  $\text{WO}_4$  tetrahedra and  $\text{ZrO}_6$  octahedra in the unit cell, leading to polyhedra rotation with rising temperature, shown in **Figure 1.1**. Such rotation causes the structure to recede inward and results in a reduction of unit cell volume.

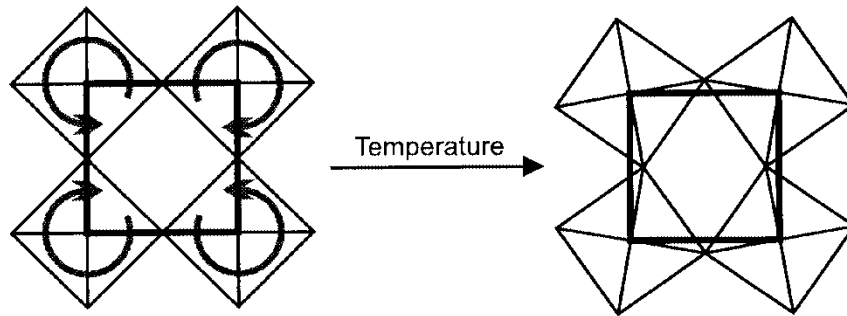


**Figure 1.1** A schematic representation of transverse vibrations of Metal-Oxygen-Metal bonds results in the NTE behavior in open framework of oxides.

ZrW<sub>2</sub>O<sub>8</sub> has attracted a growing research interest for its potential application as a fillers material in composites to control thermal expansion and eliminate residual stress generated under the temperature cycling. Several studies indicated that ZrW<sub>2</sub>O<sub>8</sub> could be incorporated into metal and ceramic-based matrices, however, due to the overall high CTE values of polymer materials, ZrW<sub>2</sub>O<sub>8</sub> has been widely applied in epoxy resins<sup>1-3</sup>, polyimides<sup>4-5</sup>, phenolic resins<sup>6</sup>, and cyanate esters<sup>7-9</sup>. In the recent decades, the development of nano-scale ZrW<sub>2</sub>O<sub>8</sub> opens a new research field. It is reported that nano-sized ZrW<sub>2</sub>O<sub>8</sub> can be synthesized from hydrothermal reaction in acidic medium; the morphologies of nanoparticles can be controlled depending on reaction conditions, such as temperature, acid concentration and type. However, a systematic comparison of the effect of nanoparticle morphology and crystallite size on the NTE behavior of ZrW<sub>2</sub>O<sub>8</sub> nanoparticles has not yet been investigated, and is one of the objectives of this work.

### 1.3 Liquid Crystalline Epoxy Resins

The potential for development of liquid crystalline (LC) networks in polymers through crosslinking of reactive end groups was suggested as early as 1969 by de Gennes<sup>10</sup>. Subsequent research in this area has resulted in a group of materials known as liquid crystalline thermosets (LCTs), whose properties transcend those observed with typical thermosetting resins bereft of any molecular order<sup>11-13</sup>. LCTs have been prepared with a variety of monomers including epoxy<sup>14-22</sup>, acrylate<sup>23-24</sup>, cyanate ester<sup>25-27</sup>, and maleimide<sup>28-29</sup>. LCERs are the most extensively investigated among LCTs due to their excellent thermomechanical properties, especially their good mechanical strength, low dielectric constant, low shrinkage upon curing, and ease of processing<sup>30-36</sup>. LCERs can be formed by curing of low molecular weight, rigid rod epoxy monomers resulting in the retention of a LC phase by the three dimensional crosslinking networks. A typical structure of LCER monomers is shown in **Figure 1.2**, which contains a rigid core and functional end epoxy groups, bridged through alkyl flexible spacers.

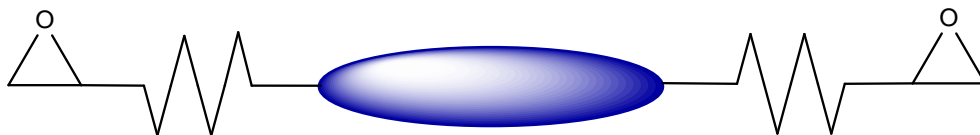


**Figure 1.2** Typical chemical structure of LCER monomers.

Compared with conventional amorphous epoxy resins, LCERs exhibit improved thermal and mechanical properties because of the presence of a rigid and ordered LC phase; therefore, they are regarded as self-reinforcing materials and have shown great potential for the development of high performance composites<sup>37-50</sup>. Another important property of LCERs is their active response to external mechanical<sup>51-60</sup>, electric<sup>61-63</sup>, or magnetic fields<sup>64-73</sup>. In the early stage of the curing reaction the low viscosity allows easy control of mesogen directions through external fields, thereby providing a unique way to tailor structure and properties of the materials. These unique properties make LCERs attractive candidates in a wide variety of applications, e.g. microelectronics, optical wave guides, adhesives, color filters, and matrices for advanced composites.

## Chapter 2: Synthesis and Characterization of Zirconium Tungstate Nanoparticles with different morphologies and physical properties

### 2.1 Introduction

Zirconium tungstate ( $\text{ZrW}_2\text{O}_8$ ) is a unique ceramic material that exhibits isotropic negative thermal expansion behavior, which can be produced at relatively low temperatures using hydrothermal synthesis followed by heat treatment. For bulk  $\text{ZrW}_2\text{O}_8$ , the coefficients of thermal expansion (CTE) for  $\alpha$ - $\text{ZrW}_2\text{O}_8$ ,  $\beta$ - $\text{ZrW}_2\text{O}_8$  and  $\gamma$ - $\text{ZrW}_2\text{O}_8$  are  $-8.8 \times 10^{-6} \text{ }^\circ\text{C}^{-1}$ ,  $-4.9 \times 10^{-6} \text{ }^\circ\text{C}^{-1}$  and  $1.0 \times 10^{-6} \text{ }^\circ\text{C}^{-1}$ , respectively.  $\text{ZrW}_2\text{O}_8$  particles have attracted great attention in recent years because of their potential use as fillers in polymer matrix composites (PMCs) to tailor thermal expansion<sup>5, 8, 74</sup>, which is a crucial factor limiting the use of PMCs for some high performance applications. The particle size and aspect ratio of  $\text{ZrW}_2\text{O}_8$  critically influences the performance and processing of such composites. The properties of nano-scale materials have been shown to be significantly different from bulk properties of the same material. In previous work, Badrinarayanan and coworkers observed differences in thermal expansion behavior between bulk  $\text{ZrW}_2\text{O}_8$  and  $\text{ZrW}_2\text{O}_8$  nanoparticles synthesized through either sol-gel or hydrothermal methods, with the nanoparticles exhibiting larger negative CTE values in the  $\alpha$ -phase than bulk  $\text{ZrW}_2\text{O}_8$ <sup>75</sup>. However, those differences were attributed to differences in adsorbed moisture content due to the significant differences in surface area between bulk and nano-scale particles. In the work reported herein, the effect of nanoparticle morphology and crystallite size on the negative thermal expansion behavior in  $\text{ZrW}_2\text{O}_8$  nanoparticles are systematically investigated.

### 2.2 Methodology

#### 2.2.1 Materials

Zirconium oxynitrate hydrate ( $\text{ZrO}(\text{NO}_3) \cdot x\text{H}_2\text{O}$ ), zirconium acetate ( $\text{Zr}(\text{C}_2\text{H}_3\text{O}_2)_4$ ) solution in dilute acetic acid (Zr 16%), zirconium perchlorate hydrate ( $\text{ZrO}(\text{ClO}_4)_2 \cdot x\text{H}_2\text{O}$ ), sodium tungstate dihydrate ( $\text{Na}_2\text{WO}_4 \cdot 2\text{H}_2\text{O}$ ) were purchased from Sigma-Aldrich (St. Louis, MO).

#### 2.2.2 Synthesis of $\text{ZrW}_2\text{O}_8$ Nanoparticles

Zirconium tungstate hydroxide hydrate was obtained by hydrothermal reaction in acidic solution. The starting material concentration ratio ( $[\text{Zr}]/[\text{W}]$ , M) was 0.08 M Zr/0.10 M W for all experiments, based on the results of by Kozy and coworkers<sup>76</sup>. In order to synthesize particles with different morphologies, several reaction parameters were varied, including raw zirconium compounds, acid types and concentration, reaction time, and reaction temperature.

The raw material compositions for a typical experiment consisted of 0.259 g  $\text{ZrO}(\text{NO}_3) \cdot x\text{H}_2\text{O}$  (or 0.347 g  $\text{ZrO}(\text{ClO}_4)_2 \cdot x\text{H}_2\text{O}$  or 1.544 g  $\text{Zr}(\text{C}_2\text{H}_3\text{O}_2)_4$  solution) and 0.330 g  $\text{Na}_2\text{WO}_4 \cdot 2\text{H}_2\text{O}$ , where each were dissolved separately in a specific amount of deionized

water. Both solutions were then combined slowly and simultaneously in a 23 ml Teflon Parr Bomb to form a mixture. White precipitates formed in the mixture during continuous stirring for several minutes, and acid solution (5 M or 7 M of HCl; 3 M or 5 M of HClO<sub>4</sub>) were slowly added. When HClO<sub>4</sub> was used as the acid, 2.758 g of NaCl was needed to provide a chloride source and to accelerate the reaction kinetics. The total solution occupied ca. 40% of the Teflon Parr Bomb's volume. After fully mixing the solution for several minutes, the Teflon Parr Bomb vessel was sealed and placed in a convection oven to facilitate a reaction at set temperatures (130 °C or 160 °C) and times (12 h or 24 h). After completion of the reaction, white precipitates were removed from the vessel and centrifuged 5 or 6 times with deionized water to remove residual acids. After drying in a vacuum oven at 75 °C for 24 h, fine and white powders of precursor ZrW<sub>2</sub>O<sub>7</sub>(OH)<sub>2</sub>·2H<sub>2</sub>O were obtained by gently grinding with a mortar and pestle. The final product of ZrW<sub>2</sub>O<sub>8</sub> powders were obtained by calcination of the precursor powders at 600 °C for 30 min.

### 2.2.3 Characterization

The X-ray diffraction (XRD) spectra at room temperature were obtained using a Scintag Powder XRD instrument with Cu-K $\alpha$  radiation with wavelength of 1.5418 Å, scanning from 10 to 40° at 40 kV/30 mA with scan step of 0.02°. Jade 6 software was used to fit XRD patterns and to calculate crystallite sizes for both ZrW<sub>2</sub>O<sub>7</sub>(OH)<sub>2</sub>·2H<sub>2</sub>O and ZrW<sub>2</sub>O<sub>8</sub> based on Scherrer's equation, with full width at half maximum (FWHM) values obtained from diffraction peaks. Silicon standard data were employed to correct broadening peaks caused by the instrument. Isothermal XRD measurements were carried out on a PANalytical instrument together with a temperature controllable hot stage. First, the samples were heated to 600 °C at a rate of 20 °C/min to fully dehydrate in the samples and thus eliminate the effects of adsorbed moisture observed in previous work<sup>75</sup>. Then, a cycle of cooling and heating was performed between room temperature and 600 °C in 10 °C temperature steps from 20 to 200 °C, and in 50 °C steps from 200 °C to 600 °C, with heating and cooling rates of 5 °C/min between each measurement temperature. The diffraction data were collected in scan steps of 0.02° from 10° to 90° for 100 s exposure times at each testing temperature. The lattice parameters at different temperatures were obtained by performing Rietveld refinement of each XRD pattern with General Structure Analysis System (GSAS) software. In each refinement, a pseudo-Voigt profile of type II was employed for fitting peak profile and 28 histogram variables were refined, including background terms, scaling factors, cell parameters, profile parameters, as well as atomic displacement parameters. The final results for all the refinements of data obtained from different temperatures are listed here:  $\chi^2$  from 2.1 to 5.2, R(F<sup>2</sup>) from 3.3% to 4.2% , and R-factors (R<sub>wp</sub>) from 4.0% to 6.7%.

The nanoparticle morphologies were characterized with a FEI Quanta 250 field emission scanning electron microscope (SEM) at 10.00 kV under high vacuum. Nanoparticle sizes were measured by the Quartz PCI viewer V5.1 software. The bright field images and electron diffraction patterns were obtained from a JEOL 2100 200 kV scanning and transmission electron microscope (STEM). The extent of hydration or moisture adsorption was characterized with a thermogravimetric analyzer (TA Instruments Q50). In each analysis, about 10 mg of nanoparticles were heated under nitrogen to 190 °C

at a heating rate of 20 °C/min and held for 10 min until no further weight loss was observed. Surface area and pore properties of nanoparticles were characterized by Micromeritics ASAP 2020 Surface Area and Porosity Analyzer.

## 2.3 Results and Discussion

### 2.3.1 Effect of Initial Zirconium Compounds on $\text{ZrW}_2\text{O}_8$ Morphology

Tetragonal  $\text{ZrW}_2\text{O}_7(\text{OH})_2 \cdot 2\text{H}_2\text{O}$  and cubic  $\text{ZrW}_2\text{O}_8$  nanoparticles could be obtained without measurable impurity under all hydrothermal conditions employed in this work and were confirmed by XRD patterns such as the representative data shown in **Figure 2.1**. However, modifications in hydrothermal synthesis conditions led to diffraction patterns with dissimilarities in Bragg's peak intensity and width due to differences in crystallite sizes of the nanoparticles. In general, the crystallite sizes of  $\text{ZrW}_2\text{O}_7(\text{OH})_2 \cdot 2\text{H}_2\text{O}$  were found to range from 20 to 66 nm, depending on experimental parameters.

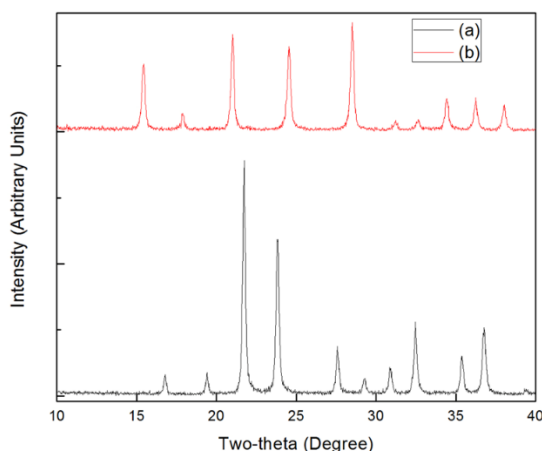


**Figure 2.1** XRD pattern of (a)  $\text{ZrW}_2\text{O}_8$  and (b)  $\text{ZrW}_2\text{O}_7(\text{OH})_2 \cdot 2\text{H}_2\text{O}$  synthesized under the condition:  $\text{ZrO}(\text{NO}_3)_2 \cdot x\text{H}_2\text{O}$  and  $\text{Na}_2\text{WO}_4 \cdot 2\text{H}_2\text{O}$  reacted in 5 M HCl at 160 °C for 12 h.

To investigate the effects of raw materials on morphology, various zirconium initial compounds ( $\text{ZrO}(\text{ClO}_4)_2 \cdot x\text{H}_2\text{O}$ ,  $\text{ZrO}(\text{NO}_3)_2 \cdot x\text{H}_2\text{O}$ , and  $\text{Zr}(\text{C}_2\text{H}_3\text{O}_2)_4$  solution) were chosen to react with  $\text{Na}_2\text{WO}_4 \cdot 2\text{H}_2\text{O}$  under the same experimental conditions. Considerably different morphologies of  $\text{ZrW}_2\text{O}_7(\text{OH})_2 \cdot 2\text{H}_2\text{O}$  nanoparticles were obtained depending on the choice of the raw zirconium compounds, as shown in **Figure 2.2**. When  $\text{ZrO}(\text{ClO}_4)_2 \cdot x\text{H}_2\text{O}$  was used as the precursor, the resulting  $\text{ZrW}_2\text{O}_7(\text{OH})_2 \cdot 2\text{H}_2\text{O}$  particles were obtained as bundle-like rods fused at one end with lengths ranging from 500 to 900 nm and widths between 30 to 80 nm, as shown in **Figure 2.2(a)**. While, large and individual rectangular rods with sizes of 0.8–1.5  $\mu\text{m}$  in length and 70–180 nm in width were obtained when  $\text{ZrO}(\text{NO}_3)_2 \cdot x\text{H}_2\text{O}$  was chosen as the precursor material, as shown in **Figure 2.2(b)**. However, significantly smaller rods with lengths between 200–500 nm and widths of 50–



80 nm were obtained when  $\text{Zr}(\text{C}_2\text{H}_3\text{O}_2)_4$  solution reacted with  $\text{Na}_2\text{WO}_4 \cdot 2\text{H}_2\text{O}$ , as seen in **Figure 2.2(c)**.

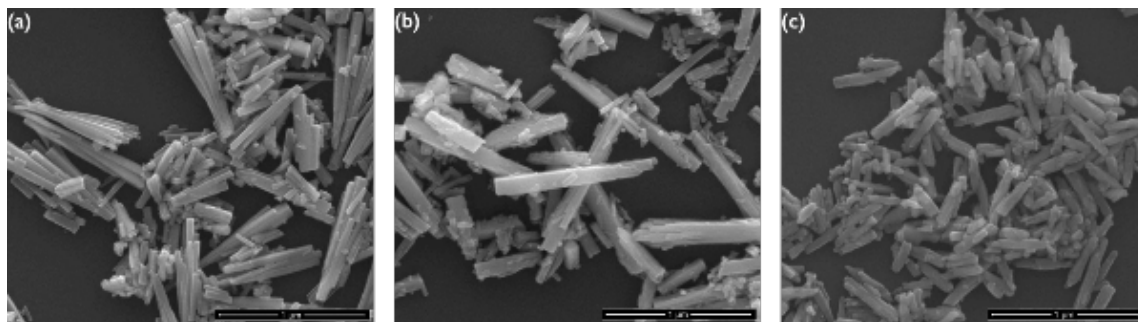


**Figure 2.2** SEM images of  $\text{ZrW}_2\text{O}_7(\text{OH})_2 \cdot 2\text{H}_2\text{O}$  synthesized under the following conditions: 7 M HCl at 130 °C for 12 h with zirconium precursors of (a)  $\text{ZrO}(\text{ClO}_4)_2 \cdot x\text{H}_2\text{O}$ , (b)  $\text{ZrO}(\text{NO}_3)_2 \cdot x\text{H}_2\text{O}$ , and (c)  $\text{Zr}(\text{C}_2\text{H}_3\text{O}_2)_4$  solution.

It was also found that the selected raw compounds significantly affected the crystallite sizes (as calculated from Scherrer's equation) of the resulting  $\text{ZrW}_2\text{O}_7(\text{OH})_2 \cdot 2\text{H}_2\text{O}$  nanoparticles. The crystallite sizes for the nanoparticles obtained using  $\text{ZrO}(\text{ClO}_4)_2 \cdot x\text{H}_2\text{O}$  were smaller than those obtained using  $\text{ZrO}(\text{NO}_3)_2 \cdot x\text{H}_2\text{O}$  ( $45 \pm 3$  vs.  $69 \pm 1$  nm), indicative of slower crystallization kinetics with the former reactant. The use of  $\text{Zr}(\text{C}_2\text{H}_3\text{O}_2)_4$  solution as the Zr source resulted in an even smaller crystallite size of  $30 \pm 3$  nm, under the same reaction conditions. All previous known work in the literature employed  $\text{ZrOCl}_2 \cdot x\text{H}_2\text{O}$  as the Zr source, which typically yielded either “whisker-like” particles or agglomerated rectangular rods with an average crystallite size of  $41 \pm 3$  nm. The results in this work demonstrate that different morphologies can be obtained using other zirconium compounds, which form different counter ions in the acid medium and result in differences in reaction kinetics and interparticle attraction and agglomeration.

### 2.3.2 Effect of Acid Type and Concentration on $\text{ZrW}_2\text{O}_8$ Morphology

Since the hydrothermal synthesis of  $\text{ZrW}_2\text{O}_7(\text{OH})_2 \cdot 2\text{H}_2\text{O}$  nanoparticles can only be achieved in an acidic media, it is important to investigate the effect of acid type and concentration on crystallite size and morphology of the resulting nanoparticles. As reported in prior work<sup>76</sup>, it was found that nanoparticles with different crystallite sizes and morphologies can be achieved by altering the acids. The synthesized  $\text{ZrW}_2\text{O}_7(\text{OH})_2 \cdot 2\text{H}_2\text{O}$  nanoparticles showed crystallite sizes of  $35 \pm 3$  nm and  $17 \pm 5$  nm with 5 M HCl and  $\text{HClO}_4/\text{NaCl}$  solutions. It is noted that well defined rectangular rods can be individually present in HCl acidic medium, as shown in **Figure 2.3(a) and (b)**. However, when the reaction was performed in 5M  $\text{HClO}_4$ , peanut-like and ill-defined particles consisting of several thin particles that agglomerated together were obtained, as shown in **Figure 2.3(c) and (d)**.

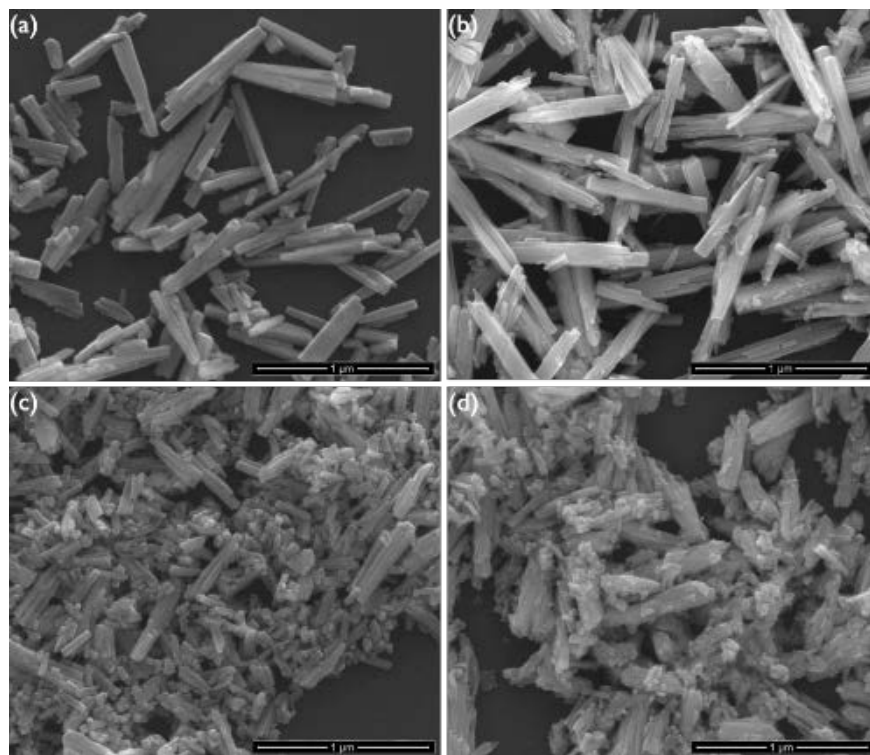


**Figure 2.3** SEM images of  $\text{ZrW}_2\text{O}_7(\text{OH})_2 \cdot 2\text{H}_2\text{O}$  synthesized using  $\text{ZrO}(\text{NO}_3)_2 \cdot x\text{H}_2\text{O}$  and  $\text{Na}_2\text{WO}_4 \cdot 2\text{H}_2\text{O}$  for 24 h at 130 °C, using different acids: (a) 5 M HCl, (b) 7 M HCl, (c) 3 M  $\text{HClO}_4$ , and (d) 5 M  $\text{HClO}_4$ .

There are likely two primary factors influencing the nanoparticle morphology and crystallite size: one is the crystallization kinetics of the  $\text{ZrW}_2\text{O}_7(\text{OH})_2 \cdot 2\text{H}_2\text{O}$  nanoparticles in an acidic medium, as demonstrated in previous work by Colin and coworkers where a higher concentration of counter ions and the presence of chloride ions ( $\text{Cl}^-$ ) significantly improved crystallization kinetics of  $\text{ZrW}_2\text{O}_7(\text{OH})_2 \cdot 2\text{H}_2\text{O}$  in an acidic solution<sup>77</sup>; the other is the interaction between the nanoparticles induced by strong electrostatic attraction. When the synthesis was carried out in HCl medium, the formation and growth of  $\text{ZrW}_2\text{O}_7(\text{OH})_2 \cdot 2\text{H}_2\text{O}$  nanoparticles was faster, as evident from the larger crystallite size, and interparticle interaction did not appear to be a dominant effect, as evident from the lack of significant agglomeration and formation of individual rods. The slower kinetics in  $\text{HClO}_4$  medium could be due to the fact that the  $\text{HClO}_4$  medium had an overall lower concentration of  $\text{Cl}^-$  ions than the HCl medium, in spite of addition of NaCl in both cases. Meanwhile, the strong attractive interaction among the nanoparticles in the  $\text{HClO}_4$  medium resulted in the agglomeration of thinner nanoparticles and overall smaller crystallite sizes compared to nanoparticles obtained in the HCl medium. Consistent with previous work in the literature with  $\text{ZrOCl}_2 \cdot 8\text{H}_2\text{O}$ , an increase in acid concentration resulted in an increase in overall particle dimensions irrespective of the zirconium compounds used<sup>76, 78-80</sup>. For example, in the  $\text{ZrO}(\text{NO}_3)_2 \cdot x\text{H}_2\text{O}$  and  $\text{Na}_2\text{WO}_4 \cdot 2\text{H}_2\text{O}$  system, an increase in HCl concentration from 5 M to 7 M HCl resulted in both an increase in crystallite size from  $50 \pm 3$  nm to  $63 \pm 3$  nm and an overall increase in particle dimensions, as shown in **Figure 2.3(a) and (b)**, respectively.

### 2.3.3 Effect of Reaction Time and Temperature on $\text{ZrW}_2\text{O}_8$ Morphology

The effects of other factors such as reaction time and temperature on controlling morphologies of nanoparticles were also examined. Two different reaction times (12 h and 24 h) were used to determine the effect of reaction time on nanoparticle morphology and crystallite size while keeping other variables the same. As shown in **Figure 2.4**, the average particle length increased from 400 nm to 1  $\mu\text{m}$  when the reaction time increased from 12 h to 24 h. An increasing reaction time also resulted in an increase in crystallite size from  $24 \pm 3$  nm to  $32 \pm 2$  nm when the reaction time was extended due to Ostwald ripening. A similar effect was observed with increasing reaction temperature.

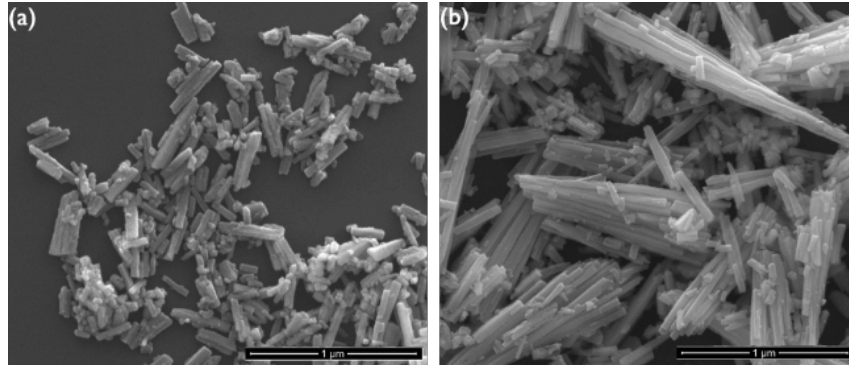


**Figure 2.4** SEM images of  $\text{ZrW}_2\text{O}_7(\text{OH})_2 \cdot 2\text{H}_2\text{O}$  synthesized from  $\text{ZrO}(\text{ClO}_4)_2 \cdot x\text{H}_2\text{O}$  and  $\text{Na}_2\text{WO}_4 \cdot 2\text{H}_2\text{O}$  under the following conditions: 3 M  $\text{HClO}_4$  at 130  $^\circ\text{C}$  for (a) 12 h, and (b) 24 h.

### 2.3.4 Selection of Promising $\text{ZrW}_2\text{O}_8$ Nanoparticles

Following these initial screening synthesis experiments, three types of  $\text{ZrW}_2\text{O}_7(\text{OH})_2 \cdot 2\text{H}_2\text{O}$  nanoparticle candidates, as specified in **Table 2.1**, were selected with different morphologies and crystallite sizes for further characterization of their physical and thermal properties. The morphologies of the three  $\text{ZrW}_2\text{O}_8$  candidates are shown in **Figure 2.5(a), (b), and (c)**.

**Table 2.1** Physical description of three types of  $\text{ZrW}_2\text{O}_8$  nanoparticles.

Nanoparticle type	Materials	Experimental conditions	Morphology	Size-scales (nm)
1	$\text{ZrO}(\text{ClO}_4)_2 \cdot x\text{H}_2\text{O}$ and $\text{Na}_2\text{WO}_4 \cdot 2\text{H}_2\text{O}$	7M HCl, 12 h, 160 $^\circ\text{C}$	Large, bundle-like rods	Length: 900-1400 Width: 80-130
2	$\text{ZrO}(\text{NO}_3)_2 \cdot x\text{H}_2\text{O}$ and $\text{Na}_2\text{WO}_4 \cdot 2\text{H}_2\text{O}$	7M HCl, 12 h, 130 $^\circ\text{C}$	Large, rectangular rods	Length: 600-1200 Width: 70-120
3	$\text{Zr}(\text{C}_2\text{H}_3\text{O}_2)_4$ solution and $\text{Na}_2\text{WO}_4 \cdot 2\text{H}_2\text{O}$	7M HCl, 12 h, 130 $^\circ\text{C}$	Small, short rods	Length: 100-400 Width: 40-60

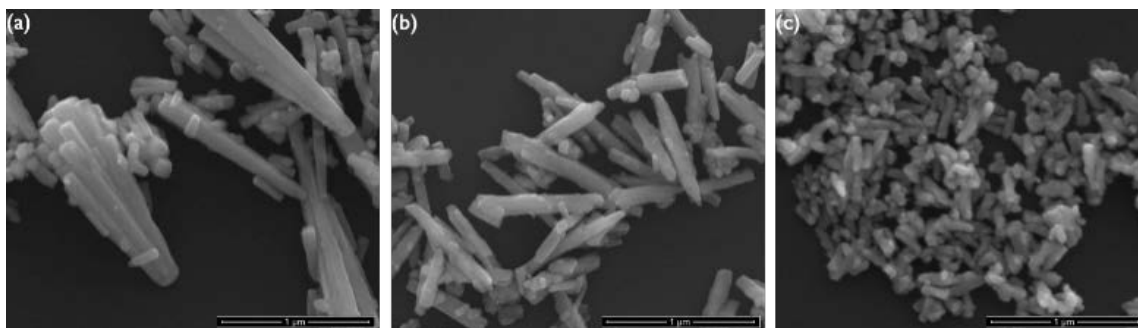


**Figure 2.5** SEM images of  $\text{ZrW}_2\text{O}_8$  particles selected for further characterizations.  $\text{ZrW}_2\text{O}_8$  calcined at 600 °C for 30 min under different hydrothermal conditions: (a) Type 1 –  $\text{ZrO}(\text{ClO}_4)_2 \cdot x\text{H}_2\text{O} / \text{Na}_2\text{WO}_4 \cdot 2\text{H}_2\text{O}$  in 7M HCl at 160 °C for 12h, (b) Type 2 –  $\text{ZrO}(\text{NO}_3)_2 \cdot x\text{H}_2\text{O} / \text{Na}_2\text{WO}_4 \cdot 2\text{H}_2\text{O}$  in 7M HCl at 130 °C for 12 h, and (c) Type 3 –  $\text{Zr}(\text{C}_2\text{H}_3\text{O}_2)_4$  solution/  $\text{Na}_2\text{WO}_4 \cdot 2\text{H}_2\text{O}$  in 7M HCl at 130 °C for 12 h.

It is noted that though there is a change in crystal form from tetragonal to cubic during the calcination process, it is not accompanied by a change in the nanoparticle morphology. The comparison of XRD patterns is shown in **Figure 2.6**. The differences in intensity and width of Bragg's peaks reflect the changes in average crystallite size of the nanoparticles, which can be quantified by Scherrer's equation. The  $\text{ZrW}_2\text{O}_7(\text{OH})_2 \cdot 2\text{H}_2\text{O}$  particles obtained from  $\text{ZrO}(\text{NO}_3)_2 \cdot x\text{H}_2\text{O} / \text{Na}_2\text{WO}_4 \cdot 2\text{H}_2\text{O}$  in 3M  $\text{HClO}_4$  shown in **Figure 2.3(c)** was once to be a candidate for further characterization due to their small particle size. Yet, the  $\text{ZrW}_2\text{O}_8$  calcined from this type of precursor exhibited a wide and heterogeneous size distribution, which was not appropriate for our future intended application, and was not investigated further.

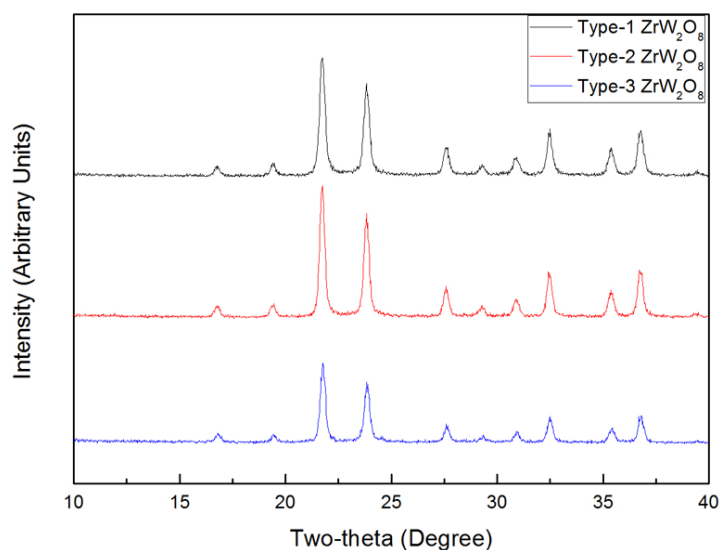


**Figure 2.6** Comparison of XRD patterns for three types of  $\text{ZrW}_2\text{O}_8$  nanoparticles.

### 2.3.5 Physical Properties of Selected ZrW<sub>2</sub>O<sub>8</sub> Nanoparticles

The NTE behavior of the candidate ZrW<sub>2</sub>O<sub>8</sub> nanoparticles were characterized by measuring the CTE values using XRD measurements at different temperatures. The CTE value ( $\alpha$ ) can be derived from the XRD patterns according to equation 1:

$$\alpha = \frac{1}{a_0} \frac{da}{dT} \quad (1)$$

where  $a_0$  is initial lattice parameter and  $da/dT$  is the change in lattice parameter with temperature. The dependence of lattice parameter on temperature for the three chosen ZrW<sub>2</sub>O<sub>8</sub> nanoparticles obtained from isothermal XRD measurements is shown in **Figure 2.7**. The error bar at each data point indicated the standard deviation of two separate measurements at temperature obtained during the first cooling and the following heating procedures. It was found that ZrW<sub>2</sub>O<sub>8</sub> exhibited noticeable reductions in lattice parameters from 9.15 to 9.12 Å with a rise in temperature from 30 to 600 °C for the three studied samples. The relationship between lattice parameter and temperature exhibits a significant change in slope at temperatures between 160 and 170 °C for all three candidates. This can be attributed to a phase transition from the cubic  $\alpha$ -phase to the  $\beta$ -phase, which is characterized by a disordered cubic lattice. In addition, when performing the Rietveld refinement of XRD patterns obtained from 70 to 160 °C, it was necessary to refine both  $\alpha$ -phase and  $\beta$ -phase simultaneously to improve the fitting quality. This means phase transition of ZrW<sub>2</sub>O<sub>8</sub> does not occur in an abrupt way but instead through a gradual process, with the  $\beta$ -phase ZrW<sub>2</sub>O<sub>8</sub> appearing initially at 70 °C as a minor phase and finally becoming the single pure  $\beta$ -phase above 170 °C.

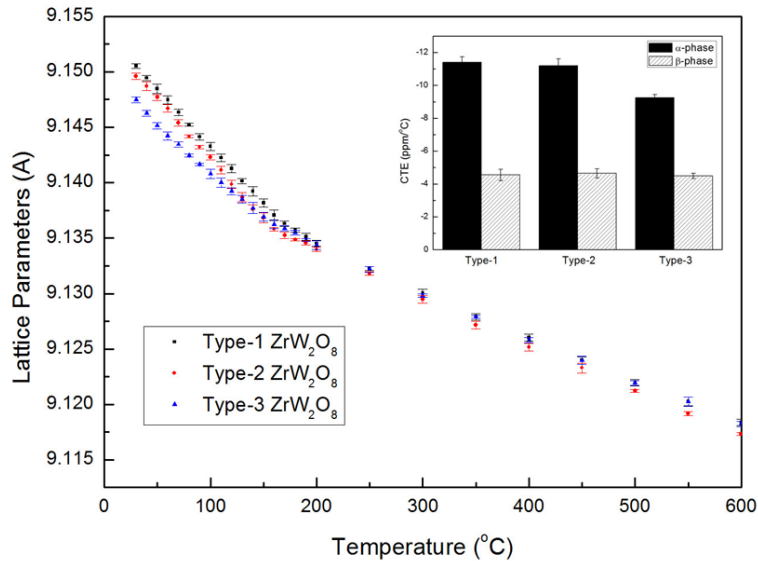


**Figure 2.7** Lattice parameter comparison of three types of ZrW<sub>2</sub>O<sub>8</sub> nanoparticles.

**Table 2.2 CTE values of different types of ZrW<sub>2</sub>O<sub>8</sub> nanoparticles.**

Nanoparticle type	Crystallite size (nm)	$\alpha$ -phase CTE (ppm/°C)	$\beta$ -phase CTE (ppm/°C)
1	50 $\pm$ 4	-11.4 $\pm$ 0.35	-4.55 $\pm$ 0.34
2	46 $\pm$ 4	-11.2 $\pm$ 0.42	-4.65 $\pm$ 0.28
3	32 $\pm$ 5	-9.25 $\pm$ 0.24	-4.94 $\pm$ 0.16

The CTE values of the three types of ZrW<sub>2</sub>O<sub>8</sub> nanoparticles in both the  $\alpha$ - and  $\beta$ -phases are summarized in **Table 2.2**. Since the phase transition occurs over a range of temperatures, the CTE value of the  $\alpha$ -phase ZrW<sub>2</sub>O<sub>8</sub> was determined from the data collected between 30 to 90 °C and the CTE value of the  $\beta$ -phase was calculated from the data collected between 180 to 600 °C. The CTE of  $\alpha$ -phase ZrW<sub>2</sub>O<sub>8</sub> was found to be dependent on the crystallite size of the nanoparticles. To be specific, the type-3 ZrW<sub>2</sub>O<sub>8</sub> nanoparticles with crystallite size of approximate 32 nm showed a CTE of  $-9.25 \times 10^{-6} \text{ }^{\circ}\text{C}^{-1}$ ; however, the magnitude of the negative thermal expansion was lower than the  $\alpha$ -phase CTE exhibited by the nanoparticles of type-1 ( $-11.4 \times 10^{-6} \text{ }^{\circ}\text{C}^{-1}$ ) and type-2 ( $-11.2 \times 10^{-6} \text{ }^{\circ}\text{C}^{-1}$ ) that had relative greater crystallite sizes of about 50 nm. Nonetheless, the CTE of three types of ZrW<sub>2</sub>O<sub>8</sub> in their  $\beta$ -phase exhibited similar values of  $4.55 \times 10^{-6} \text{ }^{\circ}\text{C}^{-1}$ ,  $4.65 \times 10^{-6} \text{ }^{\circ}\text{C}^{-1}$  and  $4.94 \times 10^{-6} \text{ }^{\circ}\text{C}^{-1}$ .

Characterization of the crystalline structure of individual nanoparticles is essential to understand the relationship between CTE and nanoparticle type. Bright field TEM images and electron diffraction patterns of different nanoparticles shown in **Figure 2.8** reveal that both type-1 and type-2 nanoparticles are characterized by a single crystalline structure, as evident from the presence of only one set of periodical lattice patterns, as shown in **Figure 2.8(a)** and **Figure 2.8(b)**, respectively. On the other hand, type-3 nanoparticles are characterized by a polycrystalline structure, as shown in the electron diffraction pattern in **Figure 2.8(c)**, where more than one set of lattice patterns can be observed. The constraints and stress generated among the multiple crystal boundaries in the poly-crystalline type-3 nanoparticles may reduce the propensity for the crystal structure to recede inward, leading to lower magnitude of negative CTE for type-3 particles compared to type-1 and type-2 nanoparticles. Other work in the literature has shown that presence of defects in the crystal boundaries can lead to an increase in the CTE values for nanocrystalline materials<sup>81</sup>. Hence, the presence of defects, which may contribute to a higher CTE to counteract with the NTE behavior of ZrW<sub>2</sub>O<sub>8</sub>, could be another possible reason for the overall lower negative CTE in type-3 particles. Interestingly, this does not appear to be a constraint in the high temperature  $\beta$  phase, where all three types of particles have the same values of negative CTE.

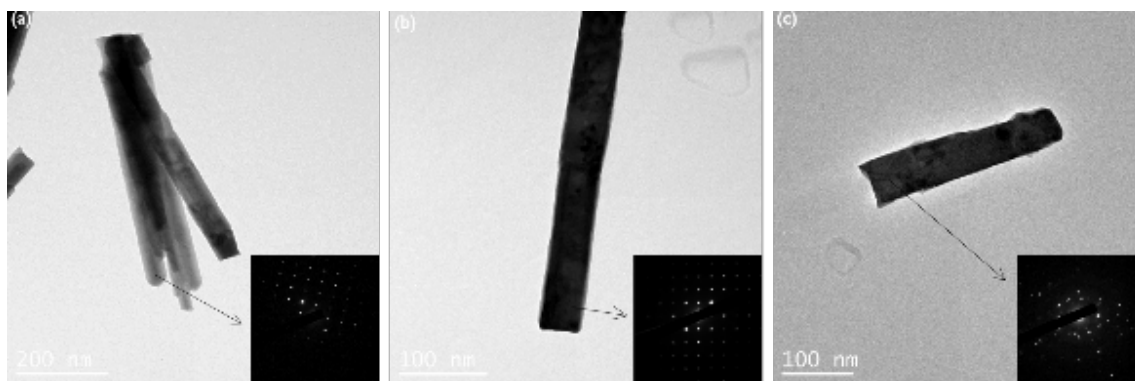


**Figure 2.8** TEM images of (a) Type-1  $\text{ZrW}_2\text{O}_8$  nanoparticle, (b) Type-2  $\text{ZrW}_2\text{O}_8$  nanoparticle, (c) Type-3  $\text{ZrW}_2\text{O}_8$  nanoparticle.

The propensity of the  $\text{ZrW}_2\text{O}_8$  nanoparticles to undergo hydration could have a detrimental effect on negative CTE behavior and impact their performance as negative CTE fillers, so understanding the relationship between particle morphology and tendency for hydration is important. Hence, in this work, the three types of  $\text{ZrW}_2\text{O}_8$  nanoparticles were sealed in ambient conditions and placed in 20 mL vials for two weeks and two months, respectively. Subsequently, TGA was employed to characterize the extent of hydration based on weight loss at 190 °C. As shown in **Figure 2.9**, an increase in storage time from two weeks to two months resulted in more hydration and greater weight loss. Furthermore, for any given storage time, three types of  $\text{ZrW}_2\text{O}_8$  nanoparticles displayed different extents of hydration. For example, among the powders stored for a duration of 2 months, type-1 nanoparticles showed the lowest weight loss (1.36 wt%) followed by type-2  $\text{ZrW}_2\text{O}_8$  with 1.75 wt% weight loss, while type-3 nanoparticles exhibited the most severe hydration p, and exhibited a total weight loss of 2.26 wt%.

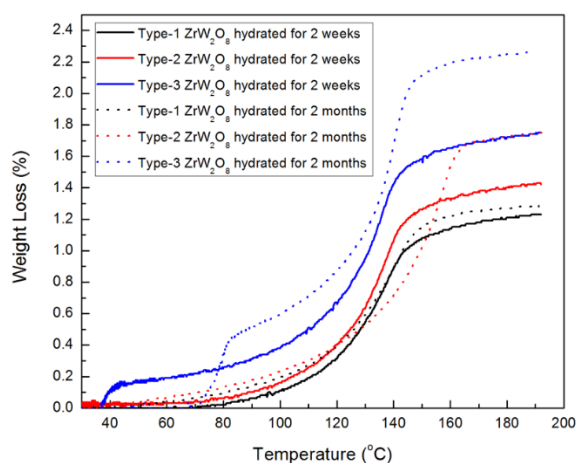


**Figure 2.9** Comparison of weight loss of hydration contents in  $\text{ZrW}_2\text{O}_8$  nanoparticles synthesized under different experimental conditions.

To investigate differences in extent of hydration for different types of  $\text{ZrW}_2\text{O}_8$  nanoparticles, it is necessary to understand the differences in the particle surfaces. Pore structures of  $\text{ZrW}_2\text{O}_8$  nanoparticles were characterized by isotherm curves of  $\text{N}_2$  adsorption-desorption shown in **Figure 2.10**. At low pressures ( $P/P_0 < 0.8$ ), absorption of  $\text{N}_2$  is restricted to the surface of particles to form thin multilayers resulting in a slow linear increase of  $\text{N}_2$  adsorption with increasing pressure. At higher pressures ( $P/P_0 > 0.8$ ), the  $\text{N}_2$  adsorption-desorption curves of the three types of synthesized  $\text{ZrW}_2\text{O}_8$  nanoparticles exhibited significant increases in  $\text{N}_2$  absorption due to capillary condensation. In addition, it was found that all three types of  $\text{ZrW}_2\text{O}_8$  nanoparticles exhibited similar type V isotherm curves with hysteresis loops but noticeable differences in extent of  $\text{N}_2$  adsorption. Since the amount of  $\text{N}_2$  adsorption represents the pore volume in the samples, and type-1  $\text{ZrW}_2\text{O}_8$  showed the lowest quantity of adsorbed  $\text{N}_2$  and thus the lowest pore volumes; while, type-3  $\text{ZrW}_2\text{O}_8$  exhibited the highest level of adsorbed  $\text{N}_2$  and greater total pore volumes.

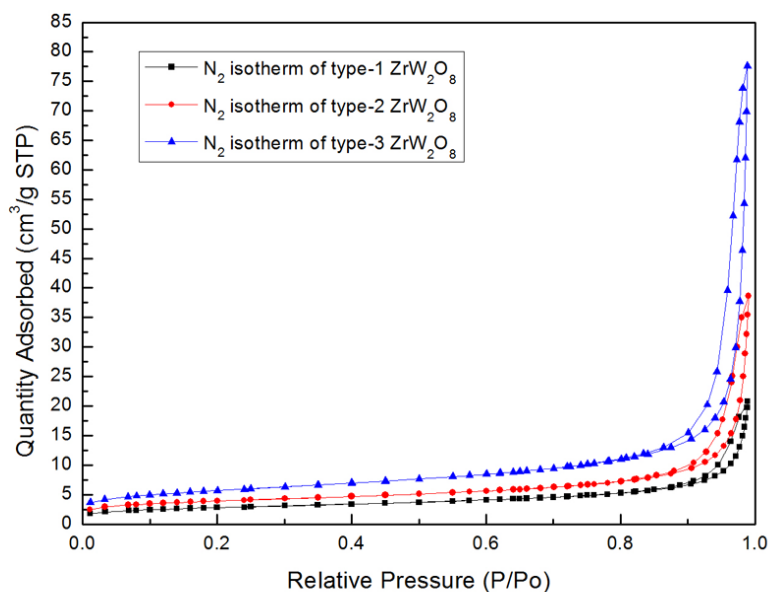


**Figure 2.10** Comparison of  $\text{N}_2$  adsorption-desorption isotherms of  $\text{ZrW}_2\text{O}_8$  nanoparticles synthesized under different experimental conditions.

The pore size distribution curves were obtained by Barret-Joyner-Halenda (BJH) desorption of  $\text{N}_2$  isotherms. As shown in **Figure 2.11**, the three types of nanoparticles exhibited a broad pore size distribution ranging from 10 to 100 nm with the majority of pore volumes concentrated at approximately 50 nm pore in diameters, which are characterized as mesopores. In addition, a significantly higher pore volume was observed for type-1 nanoparticles in comparison to type-2 and type-3 particles, which is in good agreement with the result obtained from **Figure 2.10**.



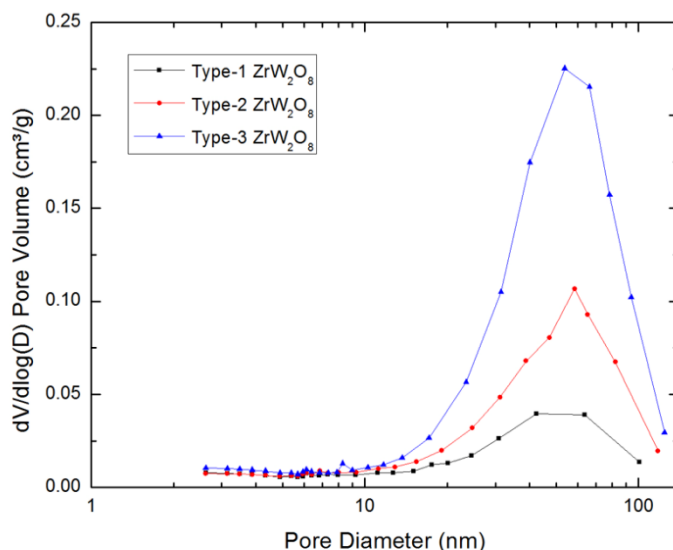


**Figure 2.11** Comparison of BJH pore size distribution of  $\text{ZrW}_2\text{O}_8$  nanoparticles synthesized under different experimental conditions.

**Table 2.3** Pore structures and hydrate weight loss of different types of  $\text{ZrW}_2\text{O}_8$  nanoparticles.

Nanoparticle type	Particle size (nm)	BET surface area ( $\text{m}^2/\text{g}$ )	BJH cumulative pore volume ( $\text{cm}^3/\text{g}$ )	BJH desorption average pore diameter (nm)	Weight loss 2 weeks (wt%)	Weight loss 2 months (wt%)
1	Length: 900-1400 Width: 80-130	9.96	0.0280	18.5	1.23	1.36
2	Length: 600-1200 Width: 70-120	13.9	0.0541	25.5	1.43	1.75
3	Length: 100-400 Width: 40-60	20.3	0.114	30.5	1.73	2.26

**Table 2.3** summarizes pore properties and TGA weight loss for the three selected  $\text{ZrW}_2\text{O}_8$  nanoparticle types. It was found that overall dimensions of the nanoparticles influenced the pore structures significantly. Type-1  $\text{ZrW}_2\text{O}_8$ , which exhibited a morphology resembling large bundle rods, showed the smallest BET surface area ( $9.96 \text{ m}^2/\text{g}$ ), the smallest total pore volume ( $0.0280 \text{ cm}^3/\text{g}$ ), and the smallest average pore size (18.5 nm). In comparison to type-1 particles, type-2  $\text{ZrW}_2\text{O}_8$  was characterized by a morphology resembling long individual rods, and showed a larger BET surface area ( $13.9 \text{ m}^2/\text{g}$ ), higher pore volume ( $0.0541 \text{ cm}^3/\text{g}$ ), and higher pore diameter (25.5 nm). Among the three types of particles, the type-3  $\text{ZrW}_2\text{O}_8$  with the smallest particles sizes exhibited the largest surface area ( $20.3 \text{ m}^2/\text{g}$ ), total pore volume ( $0.114 \text{ cm}^3/\text{g}$ ), and pore diameter

(30.5 nm) as well. The correlation between the particle dimensions Due to the tendency of nano-sized particles to agglomerate together as a consequence of electrostatic attraction, smaller particles tend to form pores with larger volumes and sizes.

The pore volumes and diameters played a crucial role in adsorbing moisture from the environment during storage. The observation of lowest degree of hydration for type-1 nanoparticles among the three types of samples could be explained by the fact that the moisture was less likely to be adsorbed and stored by particles with lower total pore volumes and smaller average pore diameters. On the other hand, type-3  $\text{ZrW}_2\text{O}_8$  nanoparticles showed the largest pore volumes and diameters and consequently exhibited the highest extent of hydration. In all cases, as the adsorbate molecules began to occupy pores, less space was left for further adsorption from the environment, leading to a reduction in hydration rate that with time as compared in **Figure 2.9**.

## 2.4 Conclusions

In this work, the relationship between synthesis variables, morphology, crystallite size, and thermal and physical properties of  $\text{ZrW}_2\text{O}_8$  nanoparticles was investigated. The morphology of hydrothermally synthesized  $\text{ZrW}_2\text{O}_7(\text{OH})_2 \cdot 2\text{H}_2\text{O}$  and  $\text{ZrW}_2\text{O}_8$  nanoparticles can be controlled by varying experimental parameters, including choice of zirconium compounds, acids and their concentrations, reaction time, and temperature. Three types of  $\text{ZrW}_2\text{O}_8$  nanoparticles with distinct morphologies and crystallite sizes were selected to investigate thermal and physical properties including CTE values, pore structures and level of hydration. The magnitude of the negative CTE was found to be larger in type-1 and type-2 nanoparticles, which were characterized by a single crystalline structure. On the other hand, in the case of type-3 particles, which had a polycrystalline structure, the presence of multiple grain boundaries and defects in the boundaries could potentially lead to the lower magnitude of NTE behavior in type-3 particles. However, this did not appear to result in a significant difference in the high temperature  $\beta$ -phase where all three types of particles exhibited similar values of negative CTE.  $\text{ZrW}_2\text{O}_8$  nanoparticle dimensions essentially determined the pore structures, which resulted from agglomeration of the nanoparticles. The  $\text{ZrW}_2\text{O}_8$  nanoparticles with larger crystallite and particle sizes, and subsequently smaller pore diameters appear to be the most promising candidates for fillers in nanocomposites due to their higher magnitude of negative CTE in the  $\alpha$ -phase and lower propensity for hydration.

## **Chapter 3: Zirconium Tungstate Nanoparticles Reinforced Epoxy Nanocomposites with Tailored Thermal Expansivity**

### **3.1 Introduction**

The ability to tailor the coefficient of thermal expansion (CTE) of a polymer is essential for mitigating thermal residual stress and reducing micro-cracks caused by CTE mismatch of different components in electronic applications. Zirconium tungstate ( $\text{ZrW}_2\text{O}_8$ ), characterized by a cubic crystal structure and space group  $\text{P}2_13$  in the  $\alpha$ -phase, exhibits strong and isotropic negative thermal expansion (NTE) behavior over a wide temperature range (from 0.3 to 1050 K). In recent years,  $\text{ZrW}_2\text{O}_8$  has attracted growing research interest for its potential use as a filler in composite materials to control thermal expansivity and eliminate residual thermal stress. Although several reports revealed that  $\text{ZrW}_2\text{O}_8$  can also be incorporated into metal and ceramic-based composites, the majority of matrix materials used are polymeric, including epoxy resins, polyimides, phenolic resins, and cyanate esters. The CTEs of polyester/ $\text{ZrW}_2\text{O}_8$  and epoxy/ $\text{ZrW}_2\text{O}_8$  composites with 30 vol. % of filler loading were reduced from 94 and 54  $\text{ppm}/^\circ\text{C}^{-1}$  to 56 and 18  $\text{ppm}/^\circ\text{C}^{-1}$ , respectively. Tani and coworkers found that the CTE of phenolic resin composites decreased from  $46 \times 10^{-6}$  to  $14 \times 10^{-6} \text{ }^\circ\text{C}^{-1}$  by incorporating up to 52 vol. % of  $\text{ZrW}_2\text{O}_8$  filler<sup>6</sup>. Badrinarayanan and coworkers observed that the CTE of bisphenol E cyanate ester (BECy) decreased by 92 % in its glassy phase with 65 vol. % filler loading<sup>7</sup>. However, the effect of the  $\text{ZrW}_2\text{O}_8$  nanoparticle morphology on the performance of polymer matrix nanocomposites has not yet been studied. In the work reported herein, three types of  $\text{ZrW}_2\text{O}_8$  nanoparticles were synthesized under different hydrothermal conditions and their distinct properties were characterized, including morphology, particle size, aspect ratio, surface area, and CTE. The effect of morphology and thermal expansivity of zirconium tungstate nanoparticles on the rheological, thermo-mechanical, dynamic-mechanical, and dielectric properties of  $\text{ZrW}_2\text{O}_8$ /Epoxy nanocomposites were investigated.

### **3.2 Methodology**

#### **3.2.1 Materials**

The chemicals used for the synthesis of  $\text{ZrW}_2\text{O}_8$  nanoparticles with different morphologies included: zirconium oxynitrate hydrate ( $\text{ZrO}(\text{NO}_3)_2 \cdot x\text{H}_2\text{O}$ ), zirconium acetate ( $\text{Zr}(\text{C}_2\text{H}_3\text{O}_2)_4$ ) solution in dilute acetic acid (Zr 16 %), zirconium perchlorate hydrate ( $\text{ZrO}(\text{ClO}_4)_2 \cdot x\text{H}_2\text{O}$ ), and sodium tungstate dihydrate ( $\text{Na}_2\text{WO}_4 \cdot 2\text{H}_2\text{O}$ ). The chemicals were all purchased from Sigma-Aldrich (St. Louis, MO). The epoxy resin used in this experiment was bisphenol A diglycidyl ether (EPON 828), purchased from Hexion Specialty Chemicals, Inc. The curing agent was a fatty polyamide formed by tall-oil fatty acids with triethylenetetramine (Versamid 140), purchased from Cognis/BASF (Germany).

#### **3.2.2 Synthesis of $\text{ZrW}_2\text{O}_8$ Nanoparticles**

During hydrothermal synthesis of  $\text{ZrW}_2\text{O}_8$  nanoparticles with varying morphologies the experimental conditions were controlled, as described extensively in the

previous chapter. Three types of precursor nanoparticles ( $\text{ZrW}_2\text{O}_7(\text{OH})_2 \cdot 2\text{H}_2\text{O}$ ) were obtained under the following hydrothermal conditions (using a 125 ml Parr pressure vessel): 0.08 M  $\text{ZrO}(\text{ClO}_4)_2 \cdot x\text{H}_2\text{O}$  and 0.10 M  $\text{Na}_2\text{WO}_4 \cdot 2\text{H}_2\text{O}$  reacted in 7 M HCl at 160 °C for 12 h; 0.08 M  $\text{ZrO}(\text{NO}_3)_2 \cdot x\text{H}_2\text{O}$  and 0.10 M  $\text{Na}_2\text{WO}_4 \cdot 2\text{H}_2\text{O}$  reacted in 7 M HCl at 130 °C for 12 h; 0.08 M  $\text{Zr}(\text{C}_2\text{H}_3\text{O}_2)_4$  solution and 0.10 M  $\text{Na}_2\text{WO}_4 \cdot 2\text{H}_2\text{O}$  reacted in 7 M HCl at 130 °C for 12 h. After the reactions were completed, white precipitates were removed from the vessel and centrifuged 5-6 times with deionized water to remove residual acids. After drying in a vacuum oven at 75 °C for 24 h, fine white powders of  $\text{ZrW}_2\text{O}_7(\text{OH})_2 \cdot 2\text{H}_2\text{O}$  were obtained by gently grinding with a mortar and pestle. The final  $\text{ZrW}_2\text{O}_8$  powders were obtained by calcination of the precursor powders at 600 °C for 30 min.

### 3.2.3 Preparation of $\text{ZrW}_2\text{O}_8$ /Epoxy Nanocomposites

$\text{ZrW}_2\text{O}_8$ /Epoxy nanocomposites were processed by blending the non-surface functionalized nanoparticles directly into the epoxy resin at a mixing ratio of 70 wt. % EPON 828 and 30 wt. % Versamid 140 to investigate the thermal and physical properties of pristine nanoparticles influence on the performance of epoxy resin. Initially,  $\text{ZrW}_2\text{O}_8$  nanoparticles were ground gently with a mortar and pestle several times to break the fine powders apart after they were heated to 150 °C for 30 min to remove the residual hydrates observed in previous work. Then, the  $\text{ZrW}_2\text{O}_8$  nanoparticles were manually mixed with the epoxy resin in a silicone rubber mold (20 mm × 20 mm × 3.5 mm) and placed into a planetary mixer for high speed mixing and deaeration. Finally, after all air bubbles were removed, the mold filled with the uniform nanocomposite suspension was moved to a convection oven and cured at 120 °C for 15 h. The rectangular samples were then removed from the mold and used for further characterization.

### 3.2.4 Characterization

The morphology of the synthesized  $\text{ZrW}_2\text{O}_8$  nanoparticles was characterized using an FEI Quanta 250 field emission scanning electron microscope (FE-SEM) at 10.00 kV under high vacuum. Ultra-thin film samples with a thickness of ca. 50 nm were sliced using an ultra-microtome in order to measure the dispersion of nanoparticles in the epoxy resin utilizing a JEOL 2100 scanning and transmission electron microscope (STEM) with an accelerating voltage of 200 kV. X-ray Diffraction (XRD) patterns of synthesized  $\text{ZrW}_2\text{O}_8$  nanoparticles and prepared epoxy nanocomposites were obtained by using Scintag powder XRD instrument with Cu-K $\alpha$  radiation ( $\lambda=1.5418 \text{ \AA}$ ) at 40 kV/30 mA with scan step of 0.01° scanning from 10° to 40°. The effects of loading and nanoparticle morphology on viscosity were characterized using an AR2000EX rheometer (TA Instruments). Using parallel plate rheology, the shear rate was increased continuously from 0 to 100 s<sup>-1</sup> at room temperature. The effect of filler loading and morphology on the gel point of the epoxy resin was also studied using parallel plate oscillatory rheology measurements. The environmental control chamber was equilibrated at a temperature of 60 °C under nitrogen purge. The test mode involved two steps: initially the oscillatory strain was set at 5 % until the oscillatory stress reached 1000 Pa; once this point was reached, the oscillatory stress was held at 1000 Pa.

A Q50 thermogravimetric analyzer (TGA) from TA Instruments was employed to determine the thermal stability of the epoxy resin and the residual weight of the nanoparticulate  $\text{ZrW}_2\text{O}_8$  at different loading levels. Alumina pans were loaded with approximately 8 mg of bulk samples and heated from room temperature (25 °C) to 800 °C at a rate of 20 °C/min under air flow. Analysis of the thermal-mechanical behavior was performed on a Q400 thermo-mechanical analyzer (TMA) from TA Instruments. To prepare samples, the  $\text{ZrW}_2\text{O}_8$ -reinforced epoxy resin samples were cut into five cubic specimens (3 mm  $\times$  3 mm  $\times$  3 mm). The specimens were first heated up to 130 °C at a rate of 10 °C/min to erase the thermal history and the effect of the generated  $\gamma$ -phase  $\text{ZrW}_2\text{O}_8$  during polymerization of the nanocomposites; subsequently, they were cooled to 35 °C at a rate of 3 °C/min. The CTE values were determined after the second heating cycle, up to 125 °C at a rate of 3 °C/min. The dynamic-mechanical properties of the nanocomposites were determined using a Q800 dynamic mechanical analyzer (DMA) from TA Instruments. Three more specimens with dimensions of 6 mm  $\times$  3 mm  $\times$  1 mm were cut and tested in three-point bending mode. These specimens were first cooled to -20 °C and then heated to 200 °C at a rate of 3 °C/min. Data were collected between -20 to 200 °C at an amplitude of 10  $\mu\text{m}$  and a frequency of 1 Hz.

The dielectric properties, including relative permittivity, loss factor, and dielectric breakdown strength, of the nanocomposites were characterized using a broadband dielectric spectrometer from Novocontrol Inc. and a dielectric rigidity instrument from CEAST/Instron at room temperature. To determine the dielectric constant, the prepared samples (20 mm  $\times$  20 mm  $\times$  1 mm) were first sputtered with a silver coating in the shape of a 20 mm diameter circle on both surfaces of the samples. The sputtering was performed under argon purge on an Edwards Pirani coater. The samples were fixed between two disk electrodes before the test was performed within a frequency range from 1 to  $10^6$  Hz. To characterize the dielectric breakdown strength, the bottom side of the samples (20 mm  $\times$  20 mm  $\times$  0.5 mm) was fully sputtered by silver while ten small spots were sputtered on the top side using the same coating instrument. The samples were then placed between the probes of a dielectric rigidity instrument, where the upper probe was positioned directly on the sputtered spots. The breakdown voltage for each testing spot was measured as the voltage was increased by 0.5 kV/s and the current was maintained at 10 mA.

### 3.3 Results and Discussion

#### 3.3.1 Structure and Rheological Properties

Based on previous work, three types of  $\text{ZrW}_2\text{O}_7(\text{OH})_2 \cdot 2\text{H}_2\text{O}$  nanoparticles with distinct morphologies were synthesized under different hydrothermal experimental conditions. **Figures 3.1** compares the morphologies of the three types of  $\text{ZrW}_2\text{O}_8$  nanoparticles calcined from the precursor  $\text{ZrW}_2\text{O}_7(\text{OH})_2 \cdot 2\text{H}_2\text{O}$ . As highlighted in the **Figure 3.1**, it is shown that Type-1 and Type-2  $\text{ZrW}_2\text{O}_8$  exhibited morphologies resembled bundles consisting by 3-5 nano-rods and single individual rods, respectively, with larger particle size and higher aspect ratio than Type-3  $\text{ZrW}_2\text{O}_8$ . Several other important properties of the nanoparticles characterized in previous work, including the crystallite size, BET surface area, and CTE value, are listed in **Table 3.1**. In addition to lower surface area

shared by Type-1 and Type-2 nanoparticles, both exhibited more negative thermal expansivities in the  $\alpha$ -phase than Type-3  $\text{ZrW}_2\text{O}_8$ .

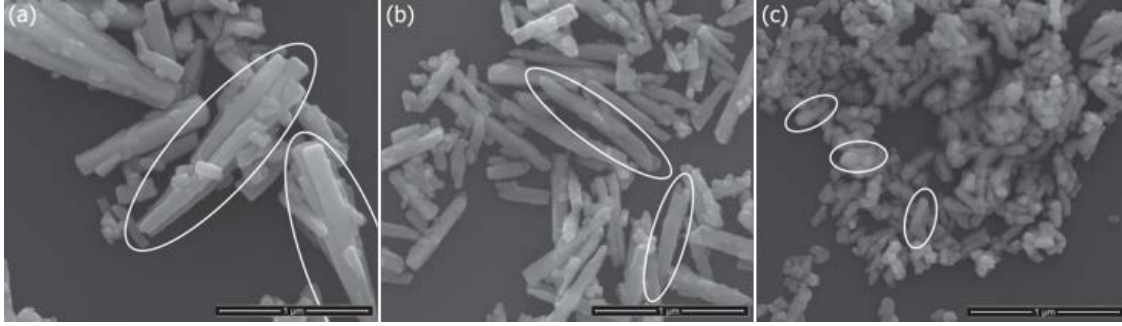


**Figure 3.1** SEM images of three types of  $\text{ZrW}_2\text{O}_8$  nanoparticles with different morphologies: (a) Type-1  $\text{ZrW}_2\text{O}_8$  nanoparticles, (b) Type-2  $\text{ZrW}_2\text{O}_8$  nanoparticles, (c) Type-3  $\text{ZrW}_2\text{O}_8$  nanoparticles.

**Table 3.1** Physical properties of three types of  $\text{ZrW}_2\text{O}_8$  nanoparticles.

Nanoparticle type	Morphology	Size scale (nm) and aspect ratio	Crystallite size (nm)	Surface area ( $\text{m}^2/\text{g}$ )	$\alpha$ -phase CTE ( $\text{ppm}/^\circ\text{C}$ )	$\beta$ -phase CTE ( $\text{ppm}/^\circ\text{C}$ )
1	Large, bundle-like rods	L: 900-1400 W: 80-130 L/W: ~13	$50 \pm 4$	9.96	$-11.4 \pm 0.352$	$-4.55 \pm 0.341$
2	Large, rectangular rods	L: 600-1200 W: 70-120 L/W: ~10	$46 \pm 4$	13.9	$-11.2 \pm 0.420$	$-4.65 \pm 0.283$
3	Small, capsule-like, short rods	L: 100-400 W: 40-60 L/W: ~6	$32 \pm 5$	20.3	$-9.25 \pm 0.243$	$-4.94 \pm 0.161$

**Figure 3.2** shows the dispersion of  $\text{ZrW}_2\text{O}_8$  nanoparticles with different morphologies and loading levels in the cured epoxy resin. The nanoparticles were homogeneously distributed in the polymer matrix independent of loading level, which can be attributed to proper mixing procedures applied during the preparation of the specimens. It is worthwhile to note that some small fragments were observed in the matrix, especially in **Figures 3.2(a)** and **3.2(c)**. They can be explained by the fact that long nano-rods were more vulnerable to be torn into smaller pieces under the high shear stress generated during the high-speed mixing procedure than smaller nanoparticles. The white spots and voids seen in the images are the result of filler materials that were removed from the resin during sectioning ultra-thin films for TEM characterization, which may due to the weak interfacial interaction between the untreated nanoparticles and epoxy resin.



**Figure 3.2** TEM images of  $\text{ZrW}_2\text{O}_8$ /Epoxy nanocomposites with different types and volume fractions of nanoparticles: (a) 10 vol. % Type-1  $\text{ZrW}_2\text{O}_8$ , (b) 20 vol. % Type-1  $\text{ZrW}_2\text{O}_8$ , (c) 10 vol. % Type-2  $\text{ZrW}_2\text{O}_8$ , (d) 20 vol. % Type-2  $\text{ZrW}_2\text{O}_8$ , (e) 10 vol. % Type-3  $\text{ZrW}_2\text{O}_8$ , (f) 20 vol. % Type-3  $\text{ZrW}_2\text{O}_8$ .

The representative powder XRD patterns of Type-1  $\text{ZrW}_2\text{O}_8$  nanoparticles, neat epoxy resin and Type-1  $\text{ZrW}_2\text{O}_8$ /Epoxy nanocomposites at two different volume fractions are given in **Figure 3.3**. The synthesized  $\text{ZrW}_2\text{O}_8$  nanoparticles from hydrothermal reaction exhibited no measurable impurity such as tungsten oxide. The  $\text{ZrW}_2\text{O}_8$ /Epoxy nanocomposites displayed the feature peaks of pure  $\alpha$ - $\text{ZrW}_2\text{O}_8$  compared with the amorphous characteristic of neat epoxy. Due to the incorporation of nano-fillers in an amorphous matrix, the XRD patterns of nanocomposites showed the reduction in overall intensity of  $(hkl)$  peaks and the absence of several small peaks such as (111), (221) and (310) compared to the XRD of  $\text{ZrW}_2\text{O}_8$  nanopowders.

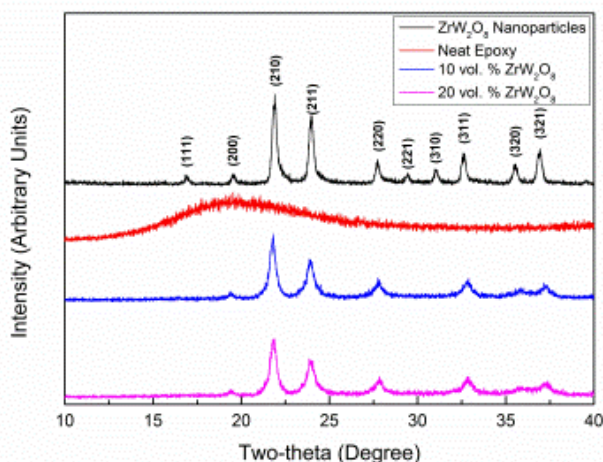


**Figure 3.3** XRD patterns of  $\text{ZrW}_2\text{O}_8$ , neat epoxy, and  $\text{ZrW}_2\text{O}_8$ /Epoxy nanocomposites.



The effects of nanoparticle properties and loading levels on the viscosity of the epoxy matrix nanocomposites were investigated under shear rates ranging from 1 to 100 s<sup>-1</sup>. **Figure 3.4** shows that the viscosity of the nanocomposites increased with increasing filler loading, which indicated intensive interaction between higher numbers of nanoparticles with the epoxy resin. Interestingly, the rheological properties of the epoxy suspension were influenced by the morphology of incorporated nano-fillers as well. For instance, the epoxy resins contained Type-1 and Type-2 ZrW<sub>2</sub>O<sub>8</sub> (characterized by larger particle size and aspect ratio) showed the higher initial viscosities (approximately 3000 and 5000 Pa·s, respectively), and exhibited a noticeable shear thinning behavior, which was a result of the alignment of nano-rods with high aspect ratio in epoxy under increment of shear rate.

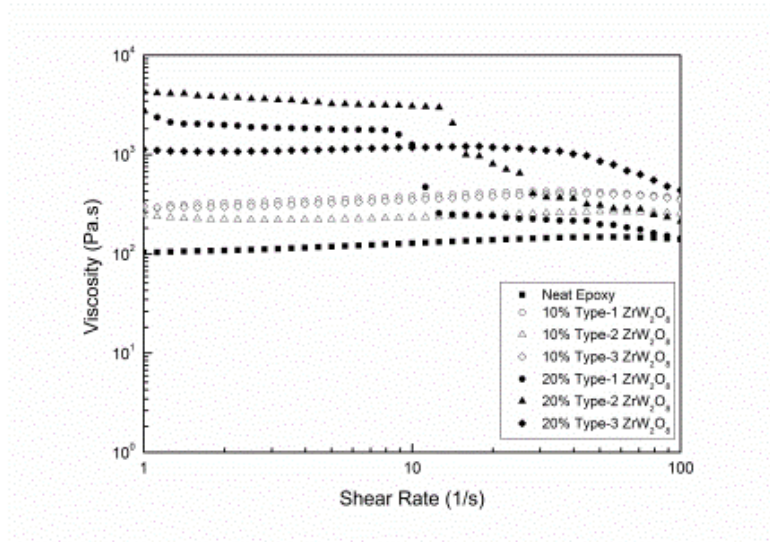


**Figure 3.4** Comparison of viscosity of ZrW<sub>2</sub>O<sub>8</sub>/Epoxy suspensions.

The gelation is identified as the point at which the storage shear modulus ( $G'$ ) and the loss shear modulus ( $G''$ ) intersects, as represented in the inset in **Figure 3.5**. A comparison of the gelation time of the neat epoxy and the nanocomposites containing different types and loadings of nanoparticles shows that the gel time diminished with increasing volume fraction of all three types of nanoparticles. As indicated in previous work, the reduction in gel time may be attributed to two factors: (1) a cross-linking reaction was promoted by the “catalytic effect” between the hydroxyl groups terminated on the surface of the nanoparticles and the epoxy resin; and (2) ZrW<sub>2</sub>O<sub>8</sub> nanoparticles affect the rheological properties of pre-polymer epoxy suspensions by increasing the elastic response of the composites. Type-3 ZrW<sub>2</sub>O<sub>8</sub> characterized by higher surface area led to a higher numbers of hydroxyl groups available, which facilitated to “catalytic effect” in the network formation of epoxy, and thus further reduces the time for gelation as present in **Figure 3.5**.



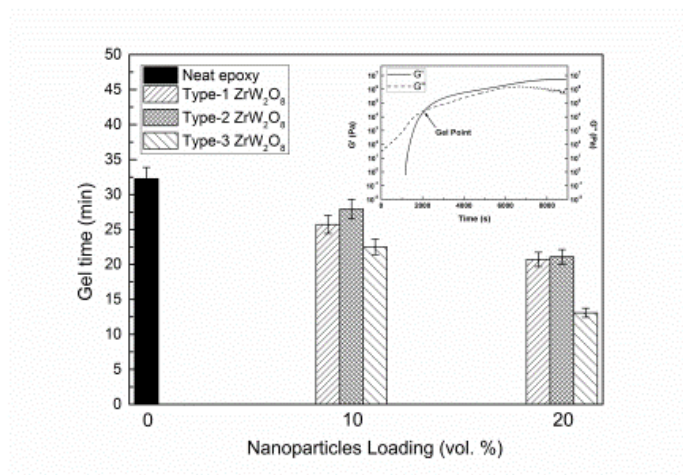


**Figure 3.5** Representation of gel point determination and comparison of gelation time of the neat epoxy resin and the  $ZrW_2O_8$ /Epoxy nanocomposites.

### 3.3.2 Thermomechanical Properties

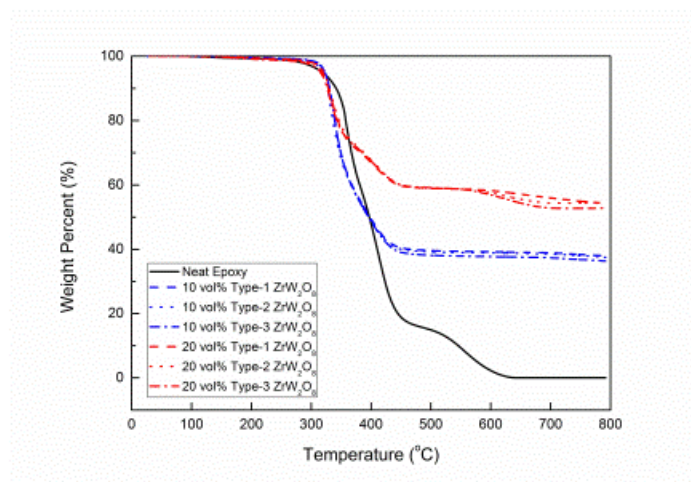


**Figure 3.6** Comparison of TGA measurements for  $ZrW_2O_8$ /Epoxy nanocomposites

**Figure 3.6** shows a neat epoxy resin which underwent thermal degradation in a temperature range from approximately 300 to 650  $^{\circ}C$ . The weight loss of the nanocomposite after complete degradation at 800  $^{\circ}C$  was used to determine the filler loading for each specimen. The weight residues of the epoxy nanocomposites containing the three types of  $ZrW_2O_8$  at different loadings are summarized in **Table 3.2**. It can be seen that they were in agreement with the calculated weight percent for both 10 vol. % (37 wt. %) and 20 vol. % (54 wt. %). The thermal stability of the samples was determined from the onset temperature at which 5 % weight loss was observed. No obvious change in the onset temperature between neat epoxy resin and the  $ZrW_2O_8$ /Epoxy nanocomposites was detected, suggesting that the addition of  $ZrW_2O_8$  has no detrimental effect on the thermal stability of the nanocomposites.

**Table 3.2** Weight residue and onset thermal-degradation temperature of epoxy resin and ZrW<sub>2</sub>O<sub>8</sub>/Epoxy nanocomposites.

Sample	Neat epoxy	Type-1 ZrW <sub>2</sub> O <sub>8</sub> 10 vol. %	Type-1 ZrW <sub>2</sub> O <sub>8</sub> 20 vol. %	Type-2 ZrW <sub>2</sub> O <sub>8</sub> 10 vol. %	Type-2 ZrW <sub>2</sub> O <sub>8</sub> 20 vol. %	Type-3 ZrW <sub>2</sub> O <sub>8</sub> 20 vol. %	Type-3 ZrW <sub>2</sub> O <sub>8</sub> 20 vol. %
Weight percent (%)	0	37.90	54.30	37.50	54.34	36.3	52.74
Temperature at 5% weight loss (°C)	318.59	323.05	319.87	318.96	320.99	323.11	316.25

Type-2 ZrW<sub>2</sub>O<sub>8</sub> nanoparticles were selected to study the effect of filler loading on thermal strain in epoxy nanocomposites. **Figure 3.7** shows that all specimens exhibited a gradual change in slope of thermal strain vs. temperature curves, which represented the onset of glass transition between a glassy and a rubbery region. Furthermore, the magnitude of thermal strain gradually decreased as the filler loading increases, which was an obvious consequence of the specimens' lower thermal expansivity caused by the inclusion of the negative CTE ZrW<sub>2</sub>O<sub>8</sub> nanoparticles. Consequently, ZrW<sub>2</sub>O<sub>8</sub>/Epoxy nanocomposites improved the dimensional stability compared to neat epoxy resin.

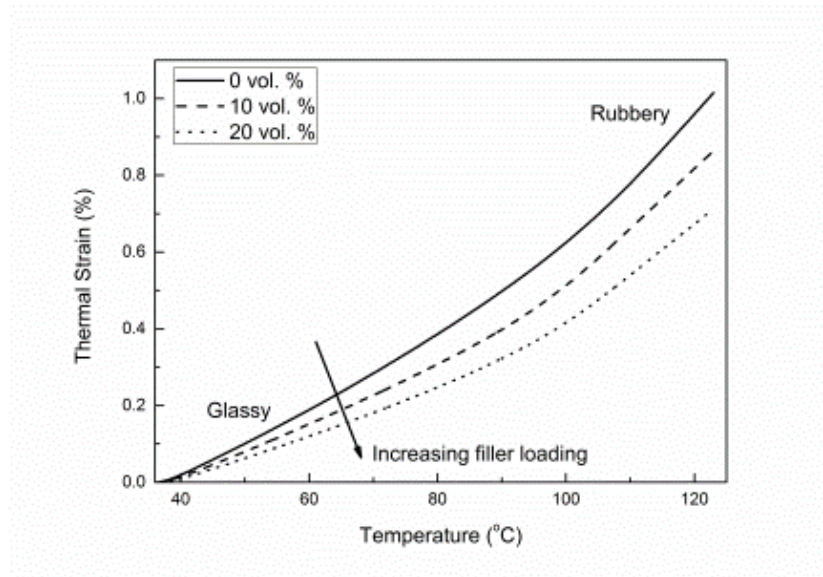


**Figure 3.7** Comparison of the effect of filler loading levels on thermal strain in ZrW<sub>2</sub>O<sub>8</sub>/Epoxy nanocomposites reinforced with Type-2 nanoparticles.

The CTE value of the glassy region was determined by the slope of the linear regression between 50 and 70 °C, while the CTE value of the rubbery region was measured from the slope of the linear regression from 105 to 120 °C, based on Equation 1:

$$\alpha = \frac{L}{L_0} \frac{dL}{dT} \quad (1)$$

where  $L_0$  is the initial length of the sample and  $L$  is the length at temperature  $T$ . **Figure 3.8(a)** shows the CTE values of the nanocomposites reinforced by three types of  $\text{ZrW}_2\text{O}_8$  nanoparticles at two filler-loading levels in the glassy region. The neat epoxy resin had a CTE of  $87.8 \pm 1.60$  ppm/°C. Addition of 10 vol. %  $\text{ZrW}_2\text{O}_8$  decreased the CTEs of the nanocomposites by different amounts depending on the types of nanoparticles. Specifically, the Type-1, Type-2 and Type-3 nano-  $\text{ZrW}_2\text{O}_8$  reduced CTE of epoxy resin by 18%, 17%, and 11% respectively. At higher loading levels (20 vol. %) of nano-fillers the decrease in CTE was more pronounced. Here, with Type-1 nanoparticles the CTE decreased approximately by 29 %, with Type-2 nanoparticles it decreased by 27 %, while a 23 % CTE reduction was achieved with Type-3 nanoparticles. As expected, the CTE of the nanocomposites in the rubbery region decreased with increasing loadings for all three types of nano-fillers as shown in **Figure 3.8(b)**. Specimens reinforced by Type-1  $\text{ZrW}_2\text{O}_8$  exhibits the highest CTE reduction with 29% at a loading level of 20 vol. %, followed by specimens reinforced by Type-2 and Type-3 nanoparticles that had CTE reduction for 21% and 19%, respectively. The differences in CTE reduction for composites containing different types of  $\text{ZrW}_2\text{O}_8$  nanoparticles can be explained by examining the thermal expansivities of the individual nanoparticles. As earlier paper reported, we showed by wide angle X-ray scattering experiments over a range of temperatures that Type-1 and Type-2  $\text{ZrW}_2\text{O}_8$  particles have lower CTE values ( $-11.2$  and  $-11.4$  ppm/°C, respectively) than Type-3 nanoparticles ( $-9.3$  ppm/°C) in the  $\alpha$ -phase (see Table 3.1). As a result, the Type-1 and Type-2 nanoparticles had a greater CTE reduction on both glassy and rubbery regions the composites than epoxy resin reinforced with Type-3 nanoparticles at equal loading fractions.

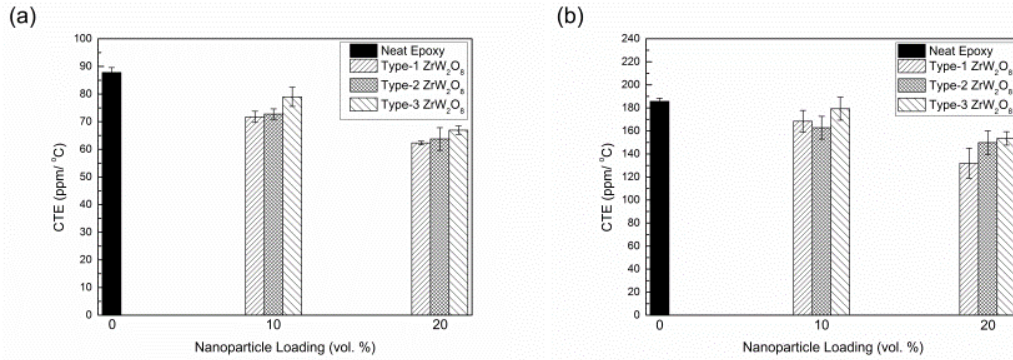


**Figure 3.8** Comparison of the CTE values of neat epoxy resin and  $\text{ZrW}_2\text{O}_8$ /Epoxy nanocomposites in the (a) glassy region and (b) rubbery region. The error bars represent standard deviations, based on five samples.

Nanocomposites containing Type-3  $\text{ZrW}_2\text{O}_8$  nanoparticles were used to examine the impact of filler volume fraction on dynamic-mechanical properties. As presented in **Figure 3.9**, the reinforcement of  $\text{ZrW}_2\text{O}_8$  nanoparticles is recognized from an increase of dynamic storage modulus ( $E'$ ) in both glassy and rubbery regions upon increasing filler loadings.

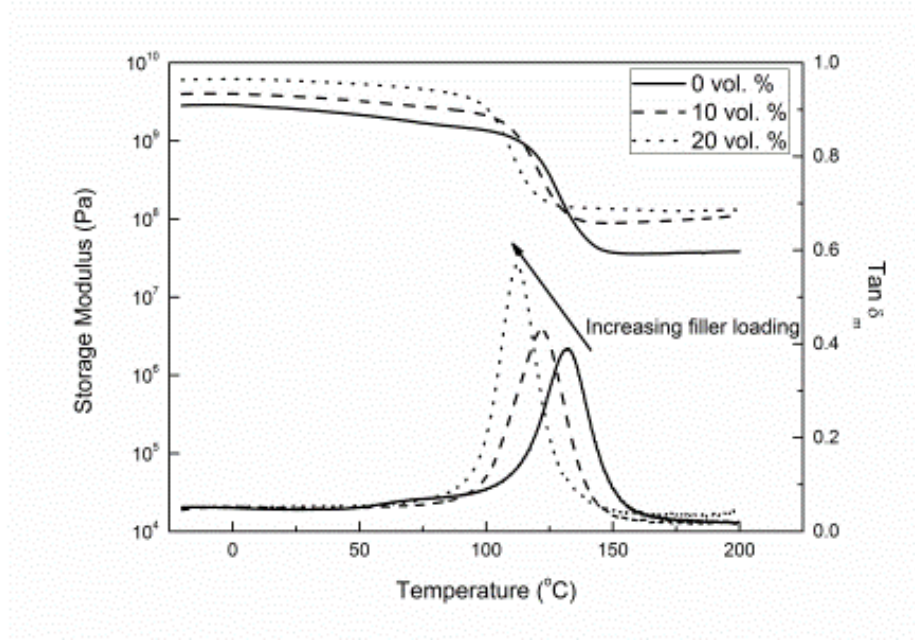


**Figure 3.9** Comparison of dynamic-mechanical properties of ZrW<sub>2</sub>O<sub>8</sub>/Epoxy nanocomposites.

The effects of different types and loadings of nanoparticles on the  $E'$  at 25 °C are compared in **Figure 3.10(a)**. Each nanoparticle-reinforced epoxy resin showed elevated  $E'$  values due to the higher Young's modulus of ZrW<sub>2</sub>O<sub>8</sub> (88.3 GPa). In addition, the overall enhancement in  $E'$  of nanocomposites was nearly equal regardless the types of reinforced nano-ZrW<sub>2</sub>O<sub>8</sub> at identical composition. The specimen reinforced by Type-2 nanoparticles exhibited a higher increase by 59% compared with Type-1 and Type-3 nano-ZrW<sub>2</sub>O<sub>8</sub> contained samples (44% and 41%, respectively) at 10 vol. %, the improvement extents were almost equivalent among the epoxy nanocomposites at 20 vol. %. This indicated that the morphology of nanoparticles had no considerable influence on the overall reinforcement effect in epoxy matrix. Besides the variation of  $E'$ , the comparison in loss factor ( $\tan \delta_m$ ) of ZrW<sub>2</sub>O<sub>8</sub>/Epoxy nanocomposites is illustrated in **Figure 3.9** as well. The magnitude of  $\tan \delta_m$  manifests the damping effect in polymer chains network, which is determined using Equation 2:

$$\tan \delta_m = \frac{E''}{E'} \quad (2)$$

where  $E''$  is the dynamic loss modulus. Upon increasing filler loadings, the observed increase in height of  $\tan \delta_m$  relaxation peak can be associated with a decrease in the crosslink density of the epoxy resin, and the peak position shift to lower temperature can be demonstrated the decreasing in glass transition temperatures ( $T_g$ ). According to previous studies, several factors may affect the  $T_g$  including tacticity and molecular weight of polymer. In this experiment, both neat epoxy and ZrW<sub>2</sub>O<sub>8</sub>/Epoxy nanocomposites were processed under same condition, therefore the introduction of plasticizer (nanoparticles)



was mainly responsible for influencing  $T_g$ . Furthermore, during sample preparation, the nano-powders were dried to eliminate any moisture effects and the specimens to be characterized were prepared with 1 mm thickness rather than as ultrathin polymer films. Therefore, such phenomena can be explained as follow: due to the weak interfacial interaction between untreated nanoparticles and epoxy resin, the introduced nanoparticles mitigated the entanglement of the molecular chain by inhibition of the network formation and enhanced the mobility of the polymer chains in the resin system, decreasing the crosslink density of epoxy.

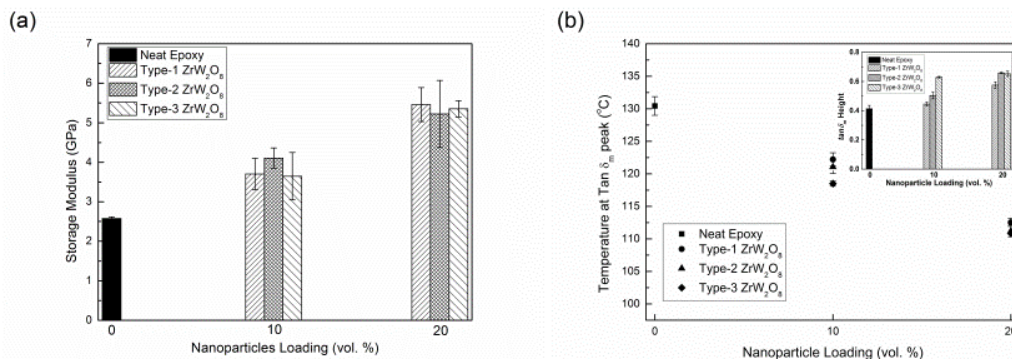


**Figure 3.10** Comparison of (a) the storage modulus ( $E'$ ) at 25 °C; (b)  $T_g$  and crosslinking density measured from the  $\tan \delta_m$  peaks of ZrW<sub>2</sub>O<sub>8</sub>/Epoxy nanocomposites. The error bars represent standard deviations based on three samples.

While it has already been established that the decreasing of  $T_g$  is correlated with the incorporated nanoparticles, it is important to explore the effect of ZrW<sub>2</sub>O<sub>8</sub> physical properties on  $T_g$ . As seen in **Figure 3.10(b)**, all three types of nanoparticles facilitated a reduction in  $T_g$  as filler loading increased. Whereas, it is interesting to observe that the nanocomposites reinforced by Type-3 ZrW<sub>2</sub>O<sub>8</sub> showed a reduction in  $T_g$  by 9.1% compared with the other samples containing Type-1 (6.3%) and Type-2 (7.1%) nanoparticles at 10 vol. % loading level. Furthermore, a higher value of  $\tan \delta_m$  (0.63) also suggested lower crosslink density formed in 10 vol. % Type-3 ZrW<sub>2</sub>O<sub>8</sub> reinforced nanocomposite as provided in the inset of **Figure 3.10(b)**. A similar relationship between  $T_g$  and maximum value of  $\tan \delta_m$  was also noticed at 20 vol. %. Based on the previous study, smaller nanoparticle with higher surface area was assumed to either exert more effective network disruption or create more interphase with repulsive interfacial interaction in epoxy matrix, both of which were responsible for a pronounced diminishing in crosslinking density and  $T_g$ .

### 3.3.3 Dielectric Properties

The effect of the morphologies and volume fractions of the ZrW<sub>2</sub>O<sub>8</sub> nanoparticles on the dielectric constant ( $\epsilon'$ ) and the dissipation factor ( $\tan \delta_e$ ) of the epoxy composites was also characterized. Because the orientation of dipole in polymer chains is dependent on frequency, the  $\epsilon'$  of neat epoxy decreased as the frequency changes from 1 to 10<sup>6</sup> Hz in **Figure 3.11(a)**. The incorporated ZrW<sub>2</sub>O<sub>8</sub> nano-fillers steadily increased the relative

permittivity over a wide frequency range without changing the frequency dependence trend, which was the consequence of the higher permittivity of  $\text{ZrW}_2\text{O}_8$  ( $\epsilon' \sim 10$ ) and the accumulation of electric charge at the extended interfaces between nanoparticles and epoxy resin induced by interfacial polarization. At lower loading, no significant difference in  $\epsilon'$  of the nanocomposites was observed for all three types of  $\text{ZrW}_2\text{O}_8$ . However, the nanocomposite reinforced by Type-1 nanoparticles exhibited a slightly higher permittivity by 0.2 than the specimens from the other two types at 20 vol. % within the same frequency range. This is likely resulted from the less amount of microscopic voids or defects created in the sample. **Figure 3.11(b)** shows  $\tan \delta_e$  as a function of  $\text{ZrW}_2\text{O}_8$  type and loading. The dielectric loss tangent is defined as:

$$\tan \delta_e = \frac{\epsilon''}{\epsilon'} \quad (3)$$

where  $\epsilon''$  is the dielectric loss. Because the dielectric loss of  $\text{ZrW}_2\text{O}_8$  is dependent on the frequency at room temperature, the increasing trend of  $\tan \delta_e$  for nanocomposites upon increasing volume fraction was more significant at low frequency ( $1 \sim 10^3$  Hz) than high frequency ( $10^3 \sim 10^6$  Hz). The slightly increase in  $\tan \delta_e$  with increasing nano-filler's loading in the epoxy composite could be originated from the combination of interfacial loss induced by excessive polarized interface and conduction loss originated from the presence of charge carriers introduced by  $\text{ZrW}_2\text{O}_8$ . However, the morphology of nanoparticle did not substantially influence the dielectric properties of epoxy nanocomposites.

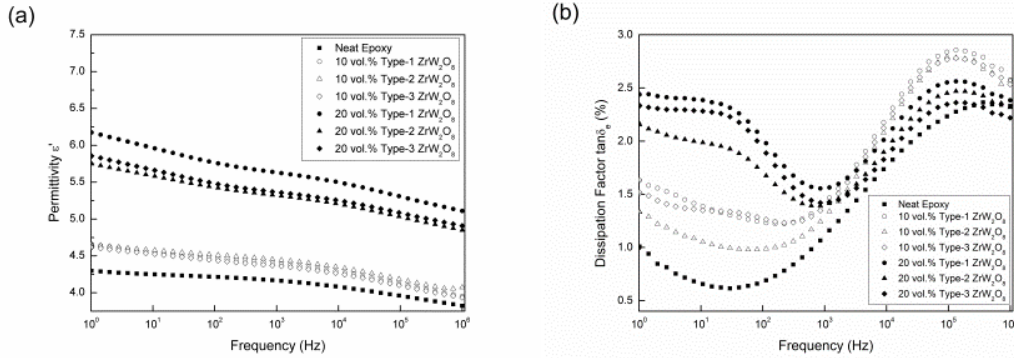


**Figure 3.11** Comparison of (a) dielectric constant and (b) dissipation factor of  $\text{ZrW}_2\text{O}_8$ /Epoxy nanocomposites.

The dielectric breakdown strength represents the capability of an insulator to withstand electrical stress before electrical failure occurs. It is measured using electrical breakdown voltage with respect to sample thickness. **Figure 3.12** shows that the breakdown strength was not deteriorated for any  $\text{ZrW}_2\text{O}_8$ /Epoxy nanocomposite compared to neat epoxy resin ( $23.46 \pm 3.198$  MV/m). However, the error bars determined from the standard deviation based on ten measured points were not identical among the tested samples. In order to identify the distribution of electrically weak points that are randomly present on identical samples, applying a statistical analysis of the measured breakdown strength data of the  $\text{ZrW}_2\text{O}_8$ /Epoxy nanocomposites is necessary.

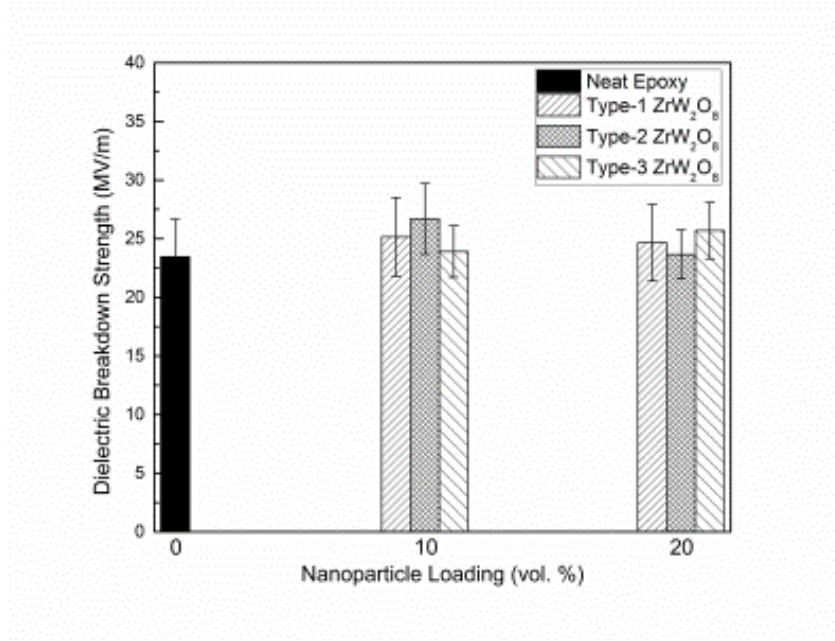


**Figure 3.12** Comparison of the dielectric breakdown voltage of ZrW<sub>2</sub>O<sub>8</sub>/Epoxy nanocomposites. The error bars represent standard deviations based on ten measurements.

The cumulative distribution function (CDF) of the dielectric breakdown strength with Weibull method was applied to investigate the distribution of dielectric breakdown behavior of identical specimens as studied in previous work. The CDF for a two-parameter Weibull distribution is determined using Equation 4:

$$F(E; \alpha, \beta) = 1 - \exp\left[-\left(\frac{E}{\alpha}\right)^\beta\right] \quad (4)$$

where  $F$  is the probability of the sample exhibiting electrical failure,  $E$  is the measured dielectric breakdown strength, and  $\alpha$  and  $\beta$  represent the scale and shape of the sample and are obtained by least-squares regression. With  $Y_i$  and  $X_i$  given by Equations 5 and 6, respectively:

$$X_i = \ln\{-\ln[1 - F(i, N)]\} \quad (5)$$

$$Y_i = \ln(E_i) = mX_i + c \quad (6)$$

CDF of the probability of breakdown  $F(i, N)$  is estimated by Equation 7:

$$F(i, N) = \frac{i - 0.3}{N + 0.4} \quad (7)$$

where,  $N$  is the total number of tested dielectric breakdown voltages and  $i$  is the assigned order for dielectric strengths, ranking from smallest to largest. The slope ( $m$ ) and intercept ( $c$ ) are defined as:

$$m = \frac{\sum_i^N (X_i - \bar{X})(Y_i - \bar{Y})}{\sum_i^N (X_i - \bar{X})^2}, \quad c = \bar{Y} - m\bar{X} \quad (8)$$

Using Equation 9:

$$\alpha = \exp(c), \quad \beta = \frac{1}{m} \quad (9)$$

both the slope and intercept can be obtained.

According to CDF of breakdown strength points shown in **Figure 3.13(a)**, the data collected from ten dielectric breakdown strength points for each testing specimen varied between 19 and 32 MV/m. The linear slope of the CDFs, which is the determination of the dispersity of breakdown strengths on identical sample, are given in **Figure 3.13(a)** and compared in **Figure 3.13(b)**. By comparing with neat epoxy, the higher gradient value of CDF curve revealed the more homogeneous distribution of breakdown strength in Type-1 particulate-reinforced nanocomposites, which was also in good agreement with higher permittivity at 20 vol. % loading (**Figure 3.11a**) by existence of less substantial microvoids. On the other hand, the slopes of CDFs were lower and similar to the value of neat epoxy regarding the specimen containing 20 vol. % Type-2  $\text{ZrW}_2\text{O}_8$  and 10 vol. % Type-3 nanoparticles, suggesting the greater disparity among the measured breakdown strengths. Such observation was attributed to the presence of micro-defects and agglomerated nanoparticles in the prepared samples, which was reflected by the large standard deviation of storage modulus in these specimens as well (**Figure 3.10a**).

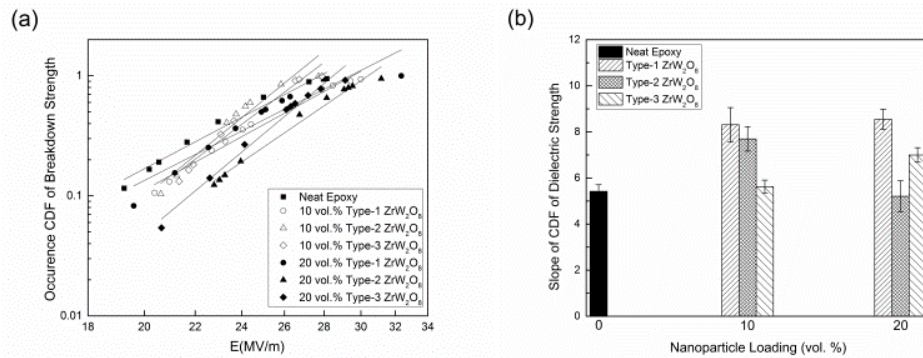


**Figure 3.13** Comparisons of (a) the CDF of the measured dielectric strength with linear fitting slopes and (b) slope value obtained from the linear fitting of  $\text{ZrW}_2\text{O}_8$ /Epoxy nanocomposites.



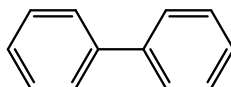
### 3.4 Conclusions

In this work, epoxy-based nanocomposites reinforced by three types of  $\text{ZrW}_2\text{O}_8$  nanoparticles with distinct physical and thermal properties and loading levels of 10 and 20 vol. % were successfully prepared. The homogenous dispersion of  $\text{ZrW}_2\text{O}_8$  nanoparticles in the polymer matrix did not negatively affect the thermal stability of the composite. The viscosity of the suspension exhibited a more significant increase when reinforced by the larger nanoparticles than with the smaller ones. The gel time of the nanocomposites decreased as  $\text{ZrW}_2\text{O}_8$  loading increased, indicating a catalytic effect of the nanoparticles on the formation of a cross-linking network. Importantly, the greatest reduction in CTEs in the glassy region was found in the specimens with 20 vol. % of those  $\text{ZrW}_2\text{O}_8$  nanoparticles that exhibited the most negative CTE values. At 25 °C, all three types of nanoparticles facilitated an overall equivalent enhancement in storage modulus of the epoxy with increasing filler loadings. However, the lowering of crosslinking density and  $T_g$  were attributed to the disruption of fully dense network and formation of repulsive interphase by presence of nanoparticles in polymer matrix. With slightly increasing nano-filler composition, both dielectric constant and dissipation factor of the nanocomposites increased slightly over the frequency range between 1 and  $10^6$  Hz due to the introduction of interfacial polarization effect between nanoparticles and epoxy matrix under AC electric field. Finally, the  $\text{ZrW}_2\text{O}_8$  nanoparticles improved dielectric breakdown strength slightly, and lowered the variation of breakdown strength according to the Weibull statistical distribution analysis. In summary, epoxy reinforced with 20 vol. % Type-1  $\text{ZrW}_2\text{O}_8$ /Epoxy nanocomposites achieved excellent CTE reduction, a pronounced improvement in dynamic mechanical properties, and preserved the advantageous dielectric properties of epoxy resins, making them prospective candidates for applications in the microelectronic insulation industry.

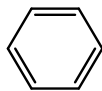
## Chapter 4: Synthesis and Characterization of Highly Crosslinked, Self-reinforcing Liquid Crystalline Epoxy Resins

### 4.1 Introduction

Liquid crystalline thermosets (LCTs) are a unique class of thermosetting materials formed upon curing of low molecular weight, rigid rod, multifunctional monomers resulting in the retention of a liquid crystalline phase by the three dimensional crosslinking networks<sup>12</sup>. A great number of LCTs based on different functional end groups have been synthesized and studied, including epoxy, acrylate, maleimide, and cyanate ester. Liquid crystalline epoxy resins (LCERs) are of great interest to scientists and engineers because of their unique properties, e.g. low shrinkage upon curing, good thermal stability, and excellent thermomechanical properties. Compared with conventional amorphous epoxy resins, LCERs exhibit improved thermal and mechanical properties because of the presence of a rigid and ordered liquid crystalline (LC) phase; therefore, they are regarded as self-reinforcing materials and have shown great potential in applications as polymer matrices in high performance composites. In the work reported herein, an epoxy monomer of 4,4'-diglycidyloxybiphenyl (BP) was synthesized and cured with a tetra-functional amine, sulfanilamide (SAA), to produce highly crosslinked LCERs. The structure, thermal properties, LC morphologies, and cure kinetics of the LCERs were studied. The effects of curing condition on the glass transition temperature, coefficient of thermal expansion (CTE), and dynamic mechanical properties of the LCERs were investigated. The chemical structures of the epoxy monomer and the curing agent are illustrated in **Figure 4.1**.



4,4'-diglycidyloxybiphenyl (BP)



Sulfanilamide (SAA)

**Figure 4.1** Chemical structures of the epoxy monomer and the curing agent.

### 4.2 Methodology

#### 4.2.1 Materials

Benzyltrimethylammonium bromide, 4,4'-dihydroxybiphenyl, and sulfanilamide were purchased from Sigma-Aldrich (Milwaukee, WI). Epichlorohydrin with 99% purity

was obtained from Acros Organics (Belgium). Sodium hydroxide, isopropyl alcohol, chloroform, methanol, hydrochloric acid, and acetone were supplied by Fisher Scientific (Fair Lawn, NJ). All chemicals were used as received without further purification.

#### **4.2.2 Synthesis of 4,4'-diglycidylxybiphenyl**

A mixture of 4,4'-dihydroxybiphenyl (57.26 g), benzyltrimethylammonium bromide (2.09 g) and epichlorohydrin (481 ml) was placed in a three-neck flask and refluxed for 40 min. NaOH (24.6 g) was dissolved in 139 ml of water to prepare 15 % NaOH aqueous solution. Then the solution was added into the flask dropwise over a period of 3 hours under reflux. The reaction was carried out for an additional hour at room temperature. The excess epichlorohydrin was removed by vacuum distillation and the final product was washed with water and methanol. A white powder was obtained by recrystallization from isopropanol/chloroform (2:1).

#### **4.2.3 Preparation of LCER and Non-LCER**

Uncured resin samples were prepared by dissolving BP and SAA in tetrahydrofuran (THF) in a stoichiometric ratio. Then the solvent was removed at room temperature and the mixture was dried under vacuum for 24 hours to prevent further reaction. To study the curing behavior, the mixture was loaded into aluminum differential scanning calorimeter (DSC) pans and hermetically sealed. A small hole was made in the center of the lids to prevent pressure buildup. To prepare bulk LCERs, the epoxy monomer was placed in a beaker and heated in an oil bath. Once the monomer was completely melted, the curing agent was added in a stoichiometric ratio, followed by vigorous stirring for approx. 1 min. The mixture was then placed in a pre-heated convection oven at a selected temperature. Because the formation of the LC phase is sensitive to the curing temperature, different curing schedules were used to produce resins with and without LC phases. The LCERs were prepared by curing the mixture at 170 °C, 180 °C, and 190 °C for 12 h; while the non-LCER was prepared by curing the mixture at 200 °C for 12 h. After the initial curing process, all samples were post-cured at 230 °C for 2 h. The solid bulk samples were machined into small pieces with appropriate size for thermomechanical tests using a diamond blade saw.

#### **4.2.4 Characterization**

The chemical structure of BP was characterized using fourier transform infrared spectroscopy (FTIR) and nuclear magnetic resonance (NMR). The FTIR spectrum was recorded on a Bruker's IFS66V FTIR with a resolution of 2 cm<sup>-1</sup> from 400 to 4000 cm<sup>-1</sup> at room temperature. The <sup>1</sup>H NMR spectrum was obtained by means of a Varian VXR-300 NMR instrument at room temperature, in the presence of CDCl<sub>3</sub> as the solvent.

The epoxy equivalent weight (EEW) of BP was determined by titration using the hydrohalogenation method. Concentrated hydrochloric acid was added into dimethylformamide to produce hydrochlorination reagent. Cresol red solution was used as acid-base indicator and was prepared by dissolving cresol red in a mixture of acetone and

distilled water. A small amount of BP was dissolved in the hydrochlorination reagent. Then the excess acid was titrated with a 0.1N sodium hydroxide solution.

Reaction kinetics of BP with SAA was investigated using a TA Instruments Q2000 DSC with a liquid nitrogen cooling system. The temperature and heat capacity calibration of the DSC were carried out using indium and sapphire standards respectively. A dry helium flow of 25 ml/min was used as the purge gas for all DSC experiments. The powder mixture was loaded into aluminum DSC pans and hermetically sealed. A small hole was made in the center of the lids to prevent pressure buildup. The sample mass was controlled between 7-9 mg. Tests were performed in a dynamic mode at various heating rates: 1, 2, 3, 4, 10, 15, 20, 25 °C/min. TMDSC experiments were carried out at 2 °C/min under a modulation amplitude of  $\pm 0.5$  °C and a period of 60 s using the same instrument. The kinetic analysis was performed utilizing the Netzsch Thermokinetics program.

The thermal properties of BP and the fully cured resins were studied using the Q2000 DSC. The DSC cell was purged with helium gas at a flow rate of 25 mL/min. The epoxy monomer was tested at a heating and cooling rate of 10 °C/min. For the fully cured resins, the first heating scan was used to erase the thermal history. While the second heating scan was recorded to evaluate  $T_g$ .

Morphologies of BP were investigated using a polarized optical microscope (POM) from Olympus (model BX51-TRF equipped with a Linkam LTS-350 hot stage and TMS-94 temperature controller). Small amounts of BP (2~3 mg) was pre-melted on a microscope slide then covered with a piece of cover glass to form a uniform thin film. The samples were heated and cooled repeatedly from room temperature to 170 °C at a rate of 1 °C/min to investigate the change of birefringence. The isothermal cure of BP with SAA was also monitored using POM. The formation and development of the LC phase were examined under polarized light.

Wide angle X-ray diffraction (WAXD) was used to explore the crystal structure of BP and the fully cured LCERs. For the epoxy monomer, a high temperature XRD experiment was carried out using Rigaku Rint 2000 diffractometer equipped with a high temperature furnace. The diffraction patterns were collected at 30 °C, 100 °C, 140 °C on heating process and 100 °C, 30 °C on cooling process respectively with a Zr-filtered MoK $\alpha$  radiation. In the experiment, a platinum plate was used as a sample holder, and the scan rate was 0.15°/min over a scan angle from 0° to 40°. For the fully cured resins, the diffraction patterns were collected using Scintag XDS2000 powder diffractometer with Kevex Peltier cooled silicon detector and Ni-filtered CuK $\alpha$  radiation. The scan rate was 2°/min over a scan angle from 0° to 40°.

Dynamic mechanical properties of the fully cured resins were studied using a model Q800 dynamic mechanical analyzer (DMA, TA Instruments, Inc.). All the samples were heated from room temperature to 280 °C at 3 °C/min, at 1Hz frequency and 25 $\mu$ m amplitude in a three-point bending mode. Creep tests were also carried out using the Q800 DMA in a three-point bending mode. Creep and creep recovery tests were performed at isotherms from 200 °C to 295 °C in intervals of 5 °C. An equilibrium time of 5 min was

used for each interval before the load was applied. A constant stress of 0.35 MPa was applied for 20 min, followed by a 20 min recovery period. The creep data were fitted using the four-parameter Burgers model. The fitting process was performed using the nonlinear curve fit function in OriginPro 9.0 (OriginLab Corporation).

The CTE of the fully cured resins was measured with a model Q400 thermomechanical analyzer (TMA, TA Instruments, Inc.) in expansion mode with a heat-cool-heat cycle at a rate of 5 °C/min-3 °C/min-3 °C/min. The second heating scan was recorded to calculate the value of CTE.

Thermal stability of the fully cured LCERs was investigated using thermogravimetric analyzer (TGA) on a model Q50 TGA (TA Instruments, Inc.). About 10 mg of resins was placed in an alumina pan and heated from room temperature to 800 °C at a rate of 20 °C/min under an air purge of 60 ml/min.

## 4.3 Results and Discussion

### 4.3.1 Chemical Structure of BP

The FTIR and NMR spectra of BP are shown in **Figure 4.2**. The characteristic FTIR peaks at 2927  $\text{cm}^{-1}$ , 1606  $\text{cm}^{-1}$ , 1500  $\text{cm}^{-1}$ , 1244  $\text{cm}^{-1}$ , 1037  $\text{cm}^{-1}$  and 910  $\text{cm}^{-1}$  can be assigned to the stretching of ( $\text{CH}_2$ ), stretching of ( $\text{C}=\text{C}$ ), bending of ( $\text{C}=\text{C}$ ), stretching of ( $\text{C}-\text{O}$ ) on aromatic rings, stretching of ( $\text{C}-\text{O}$ ) on aliphatic chain, and epoxy group, respectively. The  $^1\text{H}$  NMR spectrum was obtained at room temperature and in the presence of  $\text{CDCl}_3$  as the solvent.  $^1\text{H}$  NMR ( $\text{CDCl}_3$ ):  $\delta$ 2.78(2H, dd,  $\text{CH}_2$  of epoxy),  $\delta$ 2.93(2H, dd,  $\text{CH}_2$  of epoxy),  $\delta$ 3.38(2H, m, CH of epoxy),  $\delta$ 4.01(2H,  $\text{CH}_2$  dd, of glycidyl),  $\delta$ 4.25(2H, dd,  $\text{CH}_2$  of glycidyl),  $\delta$ 6.96(4H, d, biphenyl),  $\delta$ 7.45(4H, d, biphenyl).

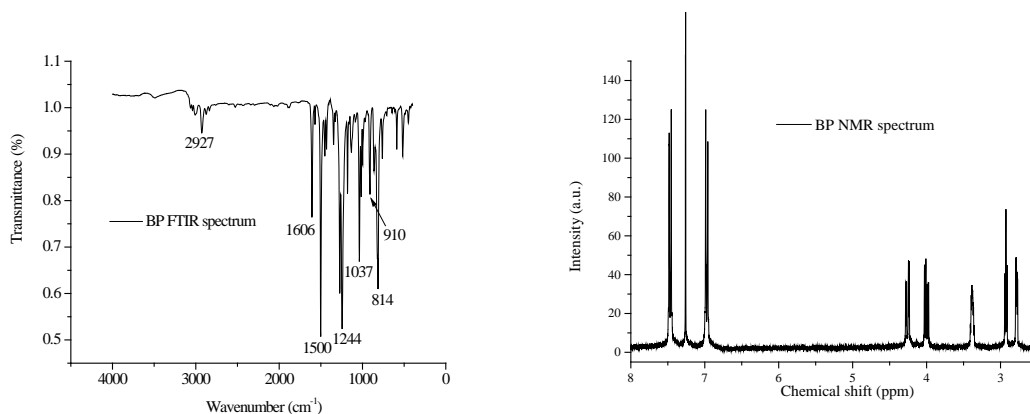


**Figure 4.2** FTIR (left) and NMR (right) spectra of BP.

### 4.3.2 Thermal Behavior and Morphology of BP

The DSC thermogram of the epoxy monomer is shown in **Figure 4.3**. Two endothermic peaks were observed in the first heating scan, while in the second heating scan,

the first peak was absent. The second peak and the shoulder attached are the melting of BP and its low molecular weight fraction, which was confirmed by gel permeation chromatography studies. The monomer was further studied using NMR and high temperature XRD to explore the different thermal behavior in the first and second heating DSC scans. In order to study the effect of the small endothermic peak in the first heating DSC scan on the chemical structure of BP, room temperature NMR spectra of the monomer dried at 100 °C and 140 °C were collected and compared. The two NMR spectra have identical peak position and area, indicating that the small endothermic peak in the DSC curve does not have any influence on the chemical structure of the monomer. A change of crystal structure could be a possible explanation for the different thermal behavior observed in the DSC scans. Therefore, a high temperature XRD experiment was carried to explore the possibility of a structural change. The full diffraction patterns are shown in **Figure 4.3**. The peaks at around 18°, 21°, 29°, 35°, and 36° are the diffraction from platinum sample holder. The shape and position of these peaks remains essentially identical. The slight shift is due to the change of lattice parameter of platinum at different temperatures. However, for the peaks in the region highlighted with dotted line, a distinct change of peak shape and position can be seen, which indicates that the crystal structure of BP at 100 °C and 140 °C are different. Furthermore, this crystal structure transition is irreversible, which is in agreement with the DSC data. Nevertheless, we were unable to identify the exact crystal structure of BP since it is not a pure compound. Based on the DSC and XRD data, we could conclude that the small endothermic peak in the first heating DSC scan is related to the change of crystal structure of BP and the transition process is irreversible.

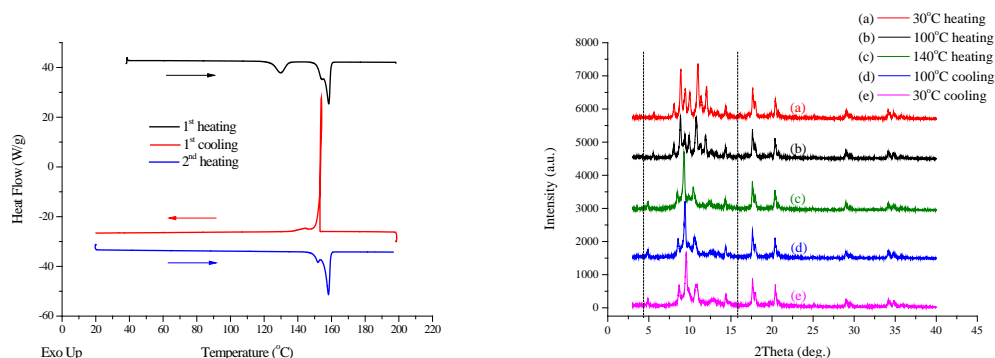


**Figure 4.3** DSC thermograms of BP (left) and XRD spectra of BP upon heating and cooling (right).

In order to clarify the LC properties of BP, we examined the morphologies at different temperatures under polarized light since it is well known that POM is a powerful tool for characterization of LC phases. POM results shown in **Figure 4.4** indicate that the monomer starts to melt at 158 °C, in a good agreement with the DSC data. At 164 °C, all the crystallites are melted and the POM image is completely dark. In the cooling process, small crystallites start to grow at about 162 °C and morphologies of the crystallites do not change much after 154 °C. Nematic LC phase usually displays schlieren texture while smectic LC phase usually shows a fan-shaped focal-conic texture. In our studies, no LC

birefringence can be observed under polarized light in both heating and cooling processes, indicating that BP is not a LC epoxy monomer.

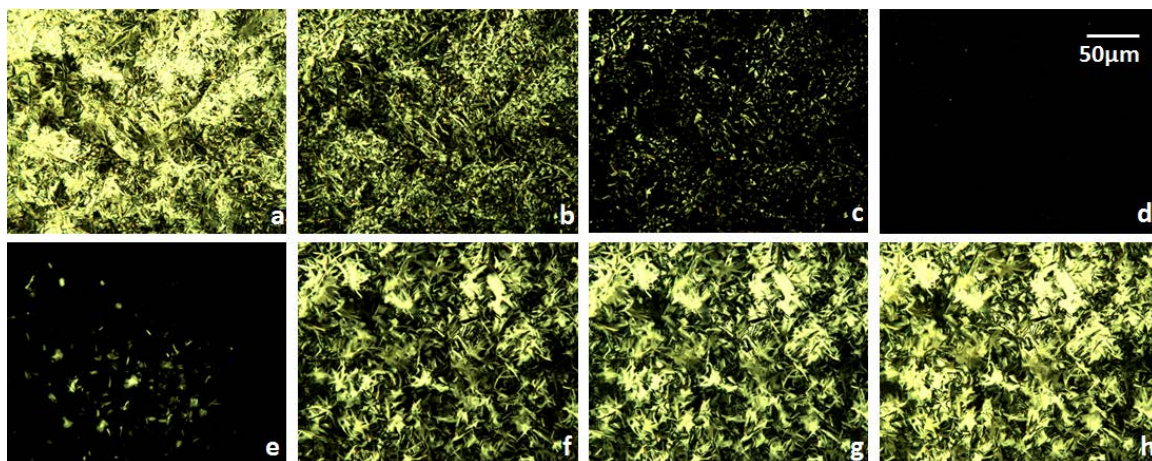


**Figure 4.4** POM images of BP upon heating and cooling. Heating process: (a) 25 °C, (b) 158 °C, (c) 162 °C, (d) 164 °C and cooling process: (e) 162 °C, (f) 158 °C, (g) 154 °C, (h) 25 °C.

#### 4.3.3 Cure Behavior and Reaction Kinetics of BP and SAA

A dynamic DSC scan was performed to study the reaction heat, onset temperature, and peak temperature of the curing reaction, which is important for determining the isothermal curing conditions. As shown in the DSC dynamic scan in **Figure 4.5**, the exothermic curing reaction of BP and SAA starts immediately after the endothermic melting of the two components. The curing reaction has a wide temperature range from 150 °C to 260 °C. When the temperature exceeds 260 °C, the resin starts to decompose, which is indicated by the onset of an exothermic peak shown in the DSC thermogram. **Figure 4.5** also shows a series of isothermal DSC curing studies of uncured resins. An additional exothermic peak indicated by arrows in the figure was observed for cure temperatures from 150 °C to 190 °C. For cure temperatures of 200 °C and higher, this peak was absent. The first exothermic peak represents the reaction between the first epoxy group of the monomer and the aromatic amine group of the curing agent. SAA is a tetra-functional curing agent and the two amine groups have different reactivity. The aromatic amine tends to react first due to the electron donating effect of the benzene ring, which results in an extension of the pre-polymer chain. If the cure temperatures can be properly chosen, the chain will keep growing without extensive branching. According to Flory's lattice theory of liquid crystalline polymers, when the aspect ratio of the polymer chain is greater than 6.4, the LC phase will be relatively stable and can be detected by POM or other experimental techniques<sup>82-83</sup>. In our case, for cure temperatures from 150 °C to 190 °C, the curing reaction does not proceed fast; therefore the pre-polymer chain has enough time to extend. After a certain period of time, LC phase becomes more stable with respect to the isotropic phase. At this time, the resins change from transparent to opaque, indicating the existence of the LC phase. The second exothermic peak in the isothermal DSC scans is a result of the rate acceleration of the cure reaction when the system undergoes a phase

transition from amorphous phase to LC phase. In the BP-SAA system examined in this work, the rate acceleration was observed for cure temperatures from 150 °C to 190 °C. At this stage of cure, the residual amine reacts with the epoxy group, leading to the formation of a crosslinked network. The LC phase formed previously is still present in the system so that it can be locked by the crosslinking process. At higher cure temperatures, reaction proceeds fast and the pre-polymer chain does not have time to extend. The crosslinking process happens before the aspect ratio of the polymer chain reaches the above mentioned critical value. The formation of the LC phase will be interrupted and the resins will be cured in the amorphous phase. This could explain the absence of the additional exothermic peak for cure temperatures higher than 200 °C.

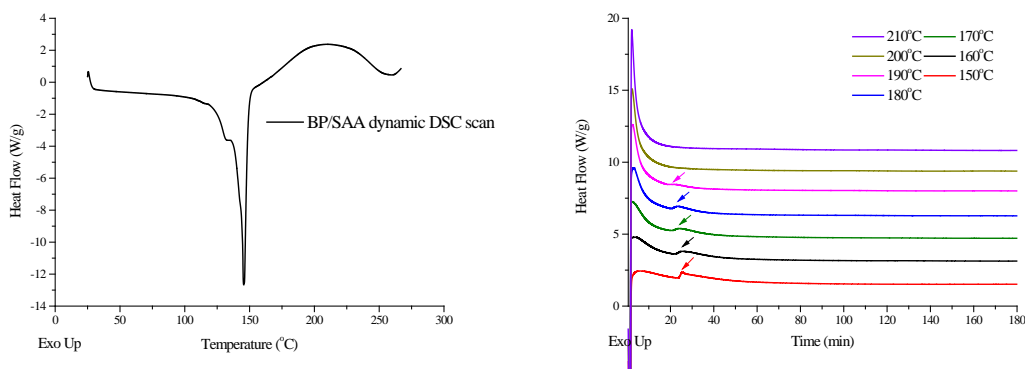


**Figure 4.5** Cure behavior of BP and SAA. Left: dynamic DSC scan. Right: isothermal DSC scan.

The curing behavior and the LC properties of the resins were also studied using POM. Based on the DSC data, the isothermal temperature was fixed at 170 °C and the whole curing process was recorded in the microscope to examine the formation of the LC phase. **Figure 4.6** shows several POM images taken at different reaction times. All the pictures were taken from the same area of the same sample. The LC birefringence starts to appear after 19 minutes of the cure reaction, which is close to the time when the second exothermic peak starts to form in the DSC scan. The isothermal curing studies were also carried out for cure temperatures at 180 °C, 190 °C, and 200 °C under POM. The sample was continuously heated at different temperatures for 2 hours to complete the cure reaction, and then morphologies of the fully cured resins were analyzed. The POM images are shown in **Figure 4.7**. The fan-shaped focal-conic texture for the cure temperatures from 170 °C to 190 °C in the figure is a characteristic of the smectic LC phase. The results prove that the LC phase formed in the early stage of the cure reaction has been successfully retained by the crosslinking networks. The results also show that as the cure temperature increases, the smectic LC phase gradually loses its fan-shaped focal-conic texture. For the cure temperature of 200 °C, the POM image is completely dark, indicating the amorphous structure of the resin. The POM study also revealed that the resins cured in LC phase exhibit a polydomain structure with individual LC domain distributed in an amorphous resin matrix.



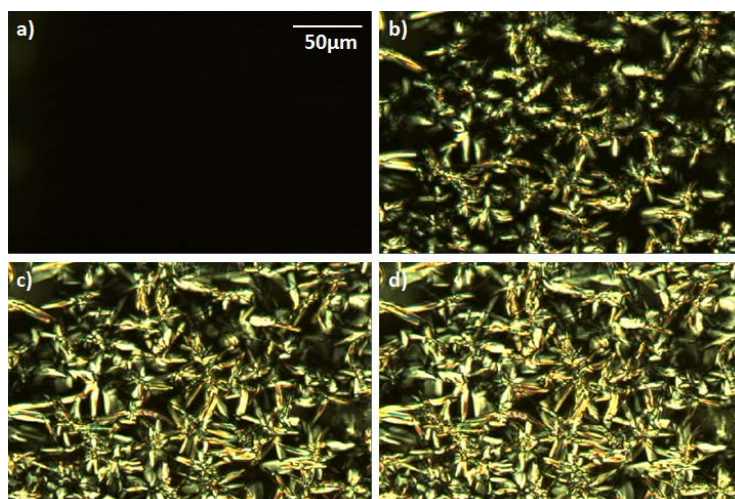


**Figure 4.6** POM images of isothermal curing study of BP with SAA at 170 °C. (a) 18 min; (b) 20 min; (c) 22 min; (d) 24 min

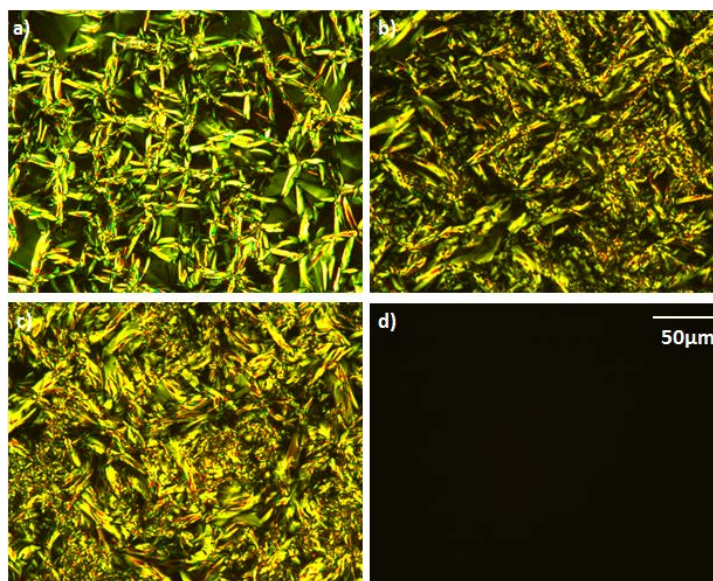


**Figure 4.7** POM images after 2h of isothermal cure of BP with SAA at different temperatures. (a) 170 °C; (b) 180 °C; (c) 190 °C; (d) 200 °C.

The reaction mechanisms of epoxy resins are complicated and the formation of an LC phase introduces further complexity into the overall cure kinetics. DSC is commonly used to investigate the curing process of thermosets<sup>84-85</sup>. In recent years, temperature modulated DSC (TMDSC) was recognized as a useful technique for characterizing the curing reaction, that can separate reversible and non-reversible heat flow signals, allowing the investigation of processes with complex kinetic mechanism<sup>86</sup>. The DSC data can be analyzed using both model-free isoconversional methods and model-fitting methods. The isoconversional kinetics analysis methods (ICM) describe the kinetics of a reaction process by using multiple single-step kinetics equations. If changes in the mechanism are

associated with changes in the activation energy, they can be detected. Therefore, the ICM is capable of detecting multi-step reactions and can provide reasonable estimations of the kinetic parameters of each step<sup>87-90</sup>. Such kinetic information can then be used as initial parameters in the model-fitting process. To further understand this material, the reaction kinetics was studied using both conventional and modulated DSC experiments. Both model-free ICM and model-fitting methods were utilized to analyze the cure kinetics. The effects of the formation of an LC phase on the overall reaction kinetics were examined using different techniques.

The dynamic DSC scans at different heating rates are shown in **Figure 4.8** and **Figure 4.9**, indicating a complex dependence of curing behavior on heating rates. In both cases, multiple endothermic peaks were observed. Of particular note is that the temperatures of these peaks were considerably lower than the melting temperature of either pure BP (156 °C) or pure SAA (165 °C). Therefore, it is thought that the sample mixing step may result in the formation of a eutectic system, leading to the complex melting behavior of the mixture. The curing reaction starts immediately after the melting of the mixture and is characterized by the broad exothermic peak. For the resins cured at 1, 2, 3, and 4 °C/min, two exothermic peaks were observed, while for the resins cured at 10, 15, 20, and 25 °C/min, only one was observed, suggesting that the curing condition has a dramatic influence on the reaction kinetics.

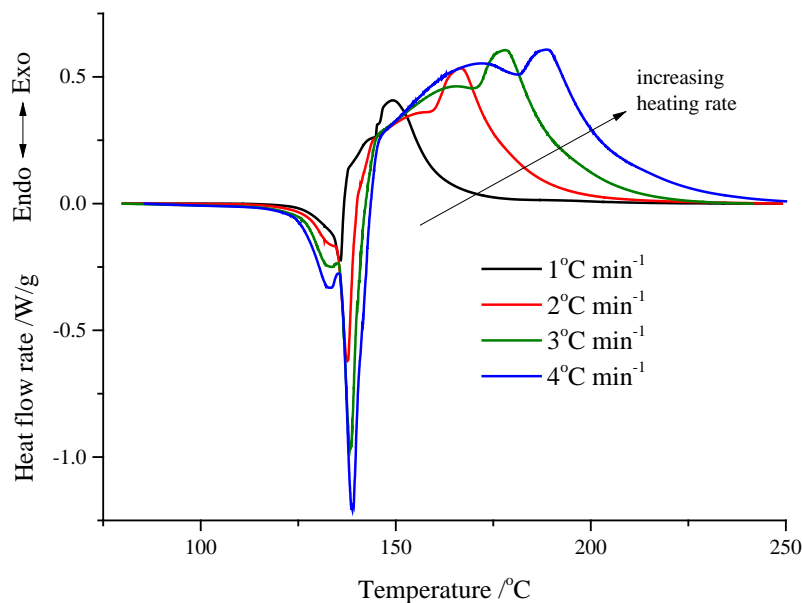


**Figure 4.8** Dynamic DSC curing curves of BP and SAA at low heating rates of 1, 2, 3, and 4 °C/min, respectively.

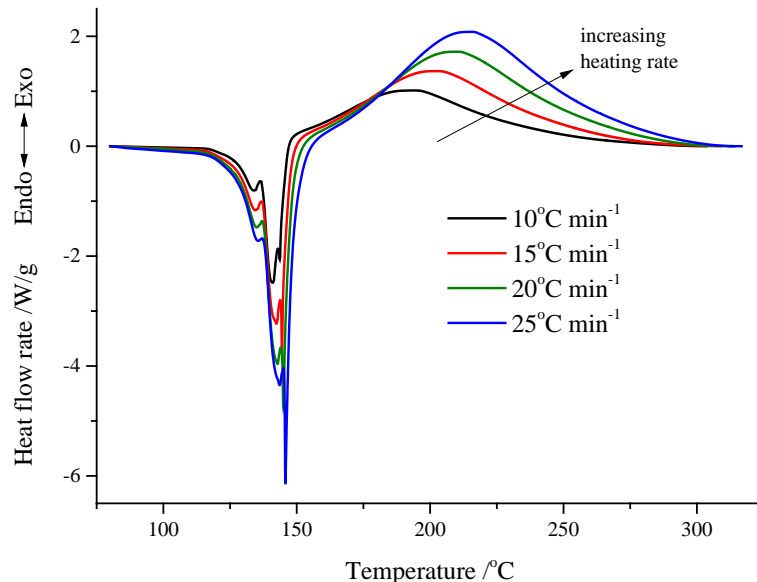


**Figure 4.9** Dynamic DSC curing curves of BP and SAA at high heating rates of 10, 15, 20, and 25 °C/min, respectively.

Subsequently, dynamic curing experiments under the same conditions were carried out using POM to monitor the formation of the LC phase. The POM images of the resins cured at 1, 4, and 10 °C/min are shown in **Figure 4.10**. At low heating rates, bright birefringence was observed, indicating the polycrystalline structure of the resins. However, for the resins cured at high heating rates, 15, 20, and 25 °C/min, the POM image is completely dark, indicating the absence of an LC phase. The initial and final sample sizes and the total enthalpy of the curing reaction measured for each sample are summarized in **Table 4.1**. The resins exhibiting a LC phase after curing show significantly higher values of reaction enthalpy, which may be attributable to the higher degree of reaction as a result of the LC formation.

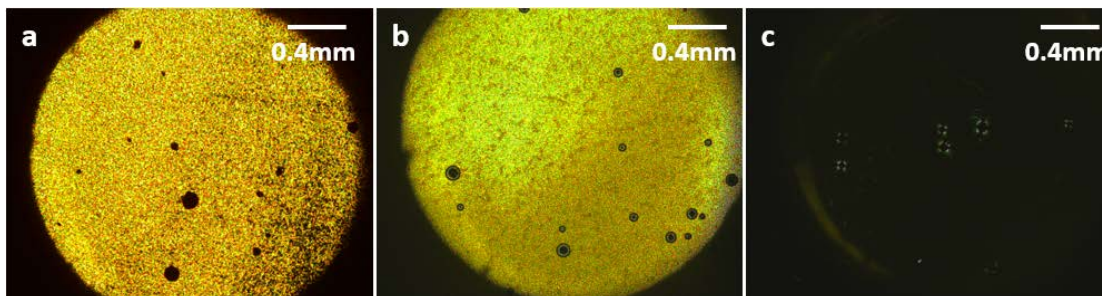


**Figure 4.10** POM images of resins cured at 1, 4, and 10 °C/min, respectively at the magnification of 50x.

**Table 4.1** Sample size and total enthalpy of reaction.

Heating Rate (°C/min)	Initial weight (mg)	Final weight (mg)	Total Enthalpy of Reaction (J/g)	Remarks
1	8.07	8.11	352	LCERs
2	7.79	7.81	358	LCERs
3	7.57	7.61	356	LCERs
4	8.36	8.39	325	LCERs
10	7.42	7.49	212	Non-LCERs
15	7.60	7.66	219	Non-LCERs
20	7.75	7.84	226	Non-LCERs
25	7.02	7.07	237	Non-LCERs

In order to investigate the effect of LC formation on the cure kinetics, TMDSC was utilized to separate the reversible and non-reversible heat flow of the curing reaction. The TMDSC curve of the resin cured at  $2\text{ }^{\circ}\text{C min}^{-1}$  with temperature modulation of  $\pm 0.5\text{ }^{\circ}\text{C}$  is shown in **Figure 4.11**. In the reversible heat flow curve, two endothermic peaks were observed with peak temperatures of  $142\text{ }^{\circ}\text{C}$  and  $163\text{ }^{\circ}\text{C}$ , respectively, as indicated by the arrows in **Figure 4.11**. The first peak represented the melting process of the initial reactant, while the second peak was related to the formation of the LC phase. Of particular note is that the LC phase transition is an endothermic process, which might be a result of the negative entropy change caused by the formation of an ordered LC phase from an isotropic phase. In the non-reversible heat flow curve, two endothermic peaks were observed, which was unexpected and could be related to the irreversible melting of the eutectic system. Two exothermic peaks were also present in the non-reversible heat flow curve, which can be attributed to a ring-opening reaction of epoxy group and the rate acceleration of the curing reaction caused by the LC formation, respectively.

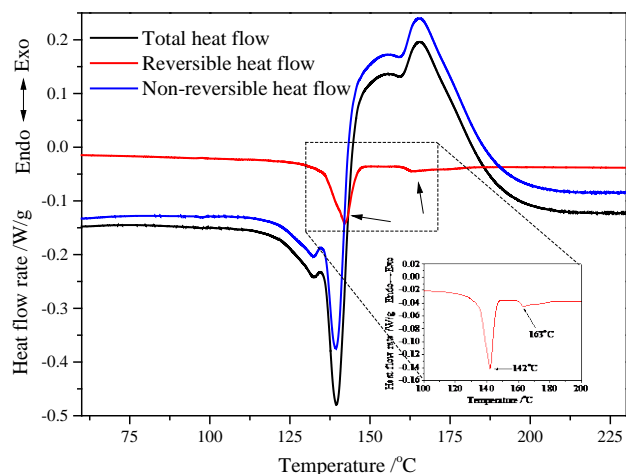


**Figure 4.11** Total heat flow, reversible and non-reversible heat flow of the curing reaction measured by TMDSC at a heating rate of  $2\text{ }^{\circ}\text{C/min}$ .

In kinetic analysis, the rate of reaction can be described by Equation 1

$$\frac{d\alpha}{dt} = k(T) f(\alpha) = A \exp\left(-\frac{E}{RT}\right) f(\alpha) \quad (1)$$

where  $k(T)$  is the temperature-dependent rate constant, and  $f(\alpha)$  is the reaction model,  $k(T)$  is commonly described by the Arrhenius equation in which  $R$  is the universal gas constant,  $E$  is the activation energy, and  $A$  is the pre-exponential factor. The heat flow rate  $dH/dt$  measured by DSC is directly related to the reaction rate by the following equation and  $\Delta H$  can be determined from integration of the DSC peak.

$$\frac{d\alpha}{dt} = \frac{dH/dt}{\Delta H} \quad (2)$$

In this study, the Friedman differential ICM was used to analyze the DSC data, which can be derived by taking the logarithm of Equation 1.

$$\ln\left(\frac{d\alpha}{dt}\right)_{\alpha,i} = \ln(A_a f(\alpha)) - \frac{E_a}{RT_{\alpha,i}} \quad (3)$$

For a specific  $\alpha$  at each heating rate  $\beta_i$ , the value of  $(d\alpha/dt)_{\alpha,i}$  and  $T_{\alpha,i}$  are determined from the DSC curves. The activation energy is then calculated from the plots of  $\ln(d\alpha/dt)_{\alpha,i}$  vs  $1/T_{\alpha,i}$ . The advantage of the Friedman method is that the DSC data can be readily used in the calculation. The Friedman plots determined from Equation 3 for both LCERs and non-LCERs are shown in **Figure 4.12**, respectively. The straight lines correspond to the linear fits for  $\alpha$  values ranging from 0.02 to 0.98.

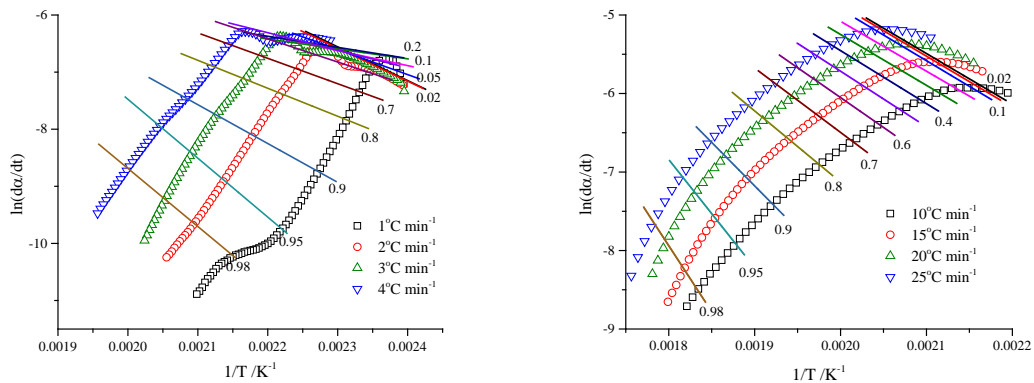


**Figure 4.12** Friedman plot for LCERs (left) and non-LCERs (right).

The variation in activation energy with degree of cure for both LCERs and non-LCERs determined from the Friedman plots are shown in **Figure 4.12**. For both systems, a dramatic increase in activation energy was observed in the later stage of curing ( $\alpha > 0.8$ ),

which indicated the presence of diffusion-controlled cure when the system approached the vitrification point caused by the increase in the glass transition temperature as a result of the curing reaction. However, it can be seen that the two systems show completely different extents of change in activation energy before the degree of cure reaches 0.8. For non-LCERs, a gradual increase of activation energy from 72 to 90 kJ mol<sup>-1</sup> was observed. While for LCERs, the activation energy exhibited a complex dependence on the degree of cure. The activation energy showed a significant decrease in the conversion range from 0 to 0.3. As mentioned previously, the formation of the LC phase at an early stage of curing led to a decrease in viscosity of the system, which facilitated the reaction between epoxy and amine, thereby lowering the activation energy. Another possible explanation is that when the LC phase transforms from an isotropic phase to a more ordered smectic LC phase, the alignment of the LC mesogens created an advantageous situation for their crosslinking, resulting in an acceleration of the overall reaction rate. As the curing reaction proceeded, the activation energy showed a gradual increase, which can be attributed to the increase in viscosity of the reacting system.

The kinetic parameters obtained from Friedman isoconversional analysis were then used to develop a multi-step reaction model. Based on the results of the original DSC scans and the activation energy plots, a five-step reaction model was designed to model the curing of LCERs, as shown in **Table 4.2**. Here, the LC formation (A→B) step was regarded as an independent reaction step and was modelled using a function based on n-dimensional nucleation growth according to the Avrami-Erofeev equation. The two endothermic melting processes and the two exothermic curing processes were modelled using a function based on n<sup>th</sup>-order reaction with autocatalysis. The curing of non-LCERs was also modelled using a five-step model, with the difference that the LC phase formation step was removed and the whole curing process was considered to be the combination of three melting processes and two curing processes in a consecutive manner.

**Table 4.2** Multi-step models used to model the curing reaction.

LCERs		Non-LCERs	
Model	$A \xrightarrow{A_n} B$	Model	$A \xrightarrow{C_n} B \xrightarrow{C_n} C \xrightarrow{C_n} D \xrightarrow{C_n} E \xrightarrow{C_n} F$
	$C \xrightarrow{C_n} D \xrightarrow{C_n} E \xrightarrow{C_n} F \xrightarrow{C_n} G$		
$A \xrightarrow{A_n} B$	LC formation	$A \xrightarrow{C_n} B \xrightarrow{C_n} C \xrightarrow{C_n} D$	Melting processes
$C \xrightarrow{C_n} D \xrightarrow{C_n} E$	Melting processes	$D \xrightarrow{C_n} E \xrightarrow{C_n} F$	Curing processes
$E \xrightarrow{C_n} F \xrightarrow{C_n} G$	Curing processes		
$A_n$	n-dimensional nucleation based on Avrami-Erofeev equation, where		
	$f(\alpha) = n\alpha(-\ln \alpha)^{(n-1)/n}$		
$C_n$	n <sup>th</sup> order reaction with autocatalysis, where		
	$f(\alpha) = (1-\alpha)^n(1+K_{cat}\alpha)$		

In kinetic modeling, for the experiments carried out at a constant heating rate, Equation 1 can be rearranged so that



$$\frac{d\alpha}{dT} = \frac{A}{\beta} \exp\left(-\frac{E}{RT}\right) f(\alpha) \quad (4)$$

where  $\beta = dT/dt$  is the heating rate. In the model-fitting method, a multivariate version of the Borchardt and Daniels method was used for the evaluation of dynamic DSC data. The kinetics parameters were obtained by a linearizing transformation of Equation 4 so that

$$\ln \frac{d\alpha / dT}{f(\alpha)} = \ln \left( \frac{A}{\beta} \right) - \frac{E}{RT} \quad (5)$$

This linear equation can be used to determine the optimal fit of the kinetic parameters by multiple linear regression. The fitting results are shown in **Figure 4.13** and the kinetic parameters extracted from the modelling were listed in **Table 4.3** and **Table 4.4** for LCERs and non-LCERs, respectively. In both cases, the experimental data are well fitted, suggesting that the multi-step model provides a good description of the curing process of BP with SAA. It should be noted that the models cannot completely simulate the complex melting behavior of the system; however, as far as the curing reactions are concerned, the models are capable of simulating the curing reaction of the system and providing information of the effects of the LC phase formation on the overall cure kinetics.

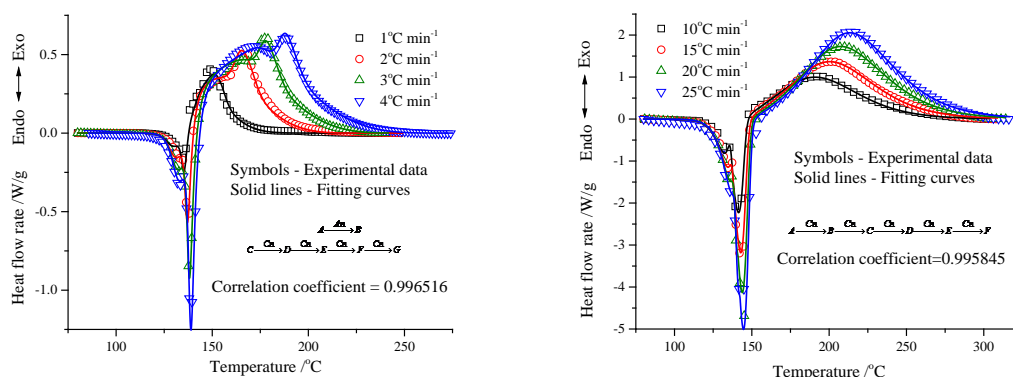


**Figure 4.13** Fitting results of LCERs (left) and non-LCERs (right).

**Table 4.3** Kinetic parameters for LCERs.

Reaction steps	Model	Log[A] (s <sup>-1</sup> )	E (kJ/mol)	n	Log[K <sub>cat</sub> ]	Contribution
1	An	1.82±2.38E-2	41.93±0.15	14.11±1.58	N/A	-0.11±4.89E-3
2	Cn	67.99±0.18	540.72±1.62	1.61±0.31	-3.99±2.72	-0.10±8.15E-3
3	Cn	66.30±8.2E-2	540.50±0.56	3.54±0.23	1.37±9.77E-2	-0.29±1.15E-2
4	Cn	-0.16±0.13	21.38±1.17	0.87±1.95E-2	-3.98±10.2	0.79±2.28E-2
5	Cn	0.36±7.16E-2	28.84±0.83	0.70±7.28E-2	0.91±5.76E-2	0.71±1.19E-2

**Table 4.4** Kinetic parameters for non-LCERs.

Reaction steps	Model	Log[A] (s <sup>-1</sup> )	E (kJ/mol)	n	Log[K <sub>cat</sub> ]	Contribution
1	Cn	31.22±4.3E-2	254.04±0.36	0.61±1.9E-2	-3.91±0.30	-0.23±6.27E-3
2	Cn	50.72±0.73	413.04±5.88	0.95±8.7E-2	-3.90±3.39	-2.87E-5±3.9E-2
3	Cn	89.20±1.67	693.38±12.06	3.55±0.56	-3.92±9.2E-4	-0.43±3.32E-2
4	Cn	6.31±0.30	75.58±2.38	1.69±5.9E-2	-3.90±4.32	2.66E-6±0.32
5	Cn	3.57±0.43	45.65±3.96	0.77±0.12	-0.18±0.26	1.66±5.28E-3

#### 4.3.4 Thermal and mechanical properties of LCERs

Bulk samples were cured in a convection oven at 170 °C, 180 °C, and 190 °C for 12 hours to produce LCERs with different LC content. Non-LCERs were also prepared by curing the resin at 200 °C for 12 hours. After the initial cure, all the samples were post-cured at 230 °C for 2 hours to complete the cure reaction as well as to relax any internal residual stress. A visual comparison between the resins cured at different temperatures is provided in **Figure 4.14**.

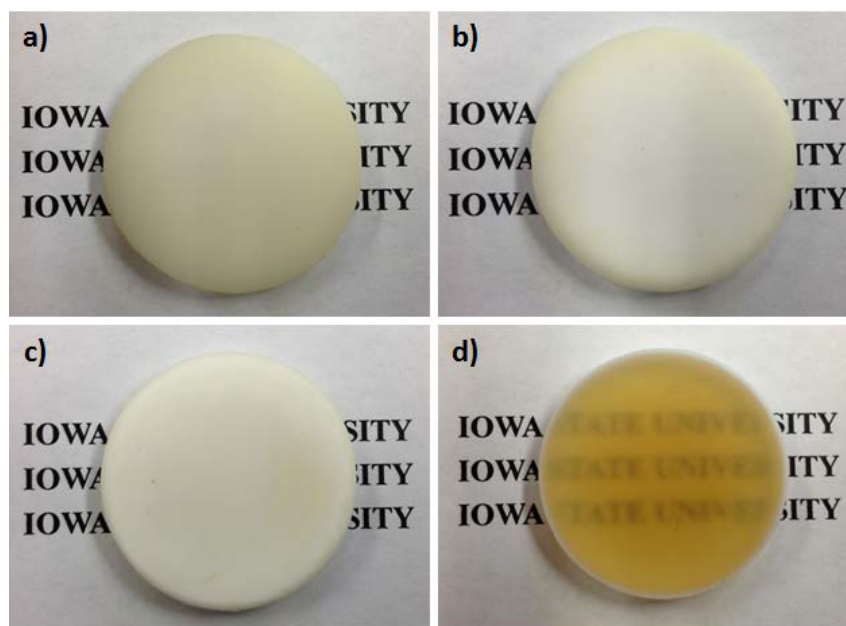


**Figure 4.14** Photos of the resins cured at different temperatures showing different optical properties. (a) 170 °C; (b) 180 °C; (c) 190 °C; (d) 200 °C.

The resins with LC domains are opaque due to the light scattering at the boundaries of the liquid crystalline and amorphous regions whereas non-LCERs, which were completely amorphous, are transparent, as shown in the same figure. XRD was also used to confirm the existence of LC phases. The XRD spectra of the LCERs and non-LCERs are compared in **Figure 4.15**. A small peak at 4.365° having d-spacing of 20.225Å was observed for LCERs while this peak is absent in the case of non-LCERs. The smectic LC phase is characterized by its layered structure. The d-spacing calculated from the XRD spectra indicates that the LCERs have layer spacing about 20Å and have a smectic LC



structure. The chemical structure of the mesogen in LCERs was simulated using ChemBio3D software as shown in **Figure 4.16**. The mesogenic length was found to be 20.4Å which was measured by calculating the bond length after minimizing the energies of the molecules. The distance between two sulfur atoms was used as the mesogenic length. Good agreement between the experimental data and the simulation was obtained, adding further evidence to the presence of a smectic phase in the LCERs.

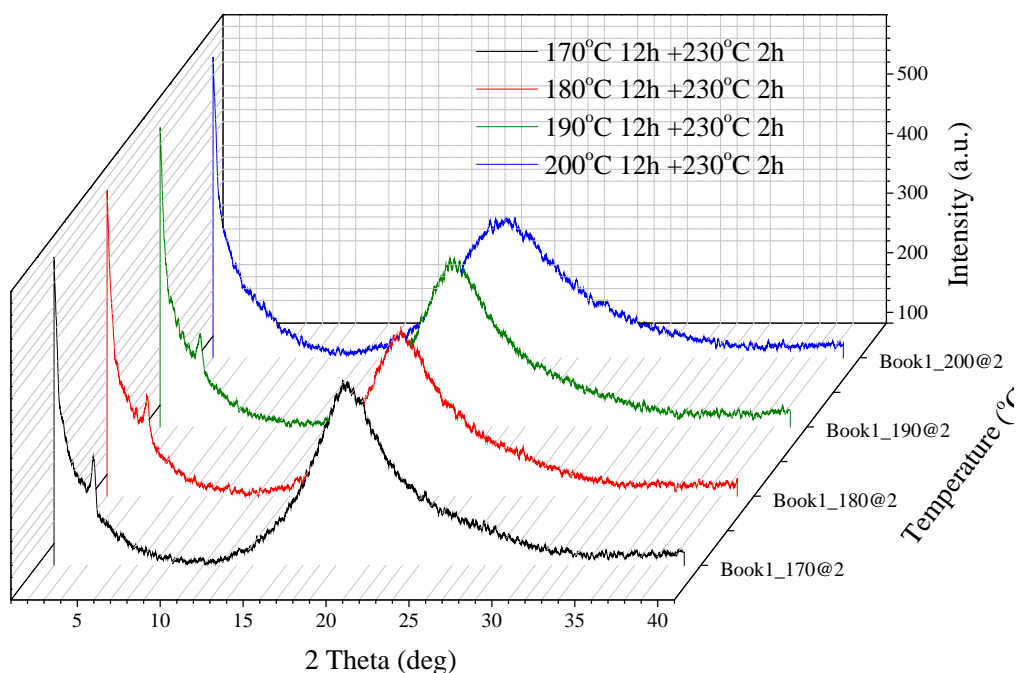


**Figure 4.15** XRD spectra of the resins cured at different temperatures.

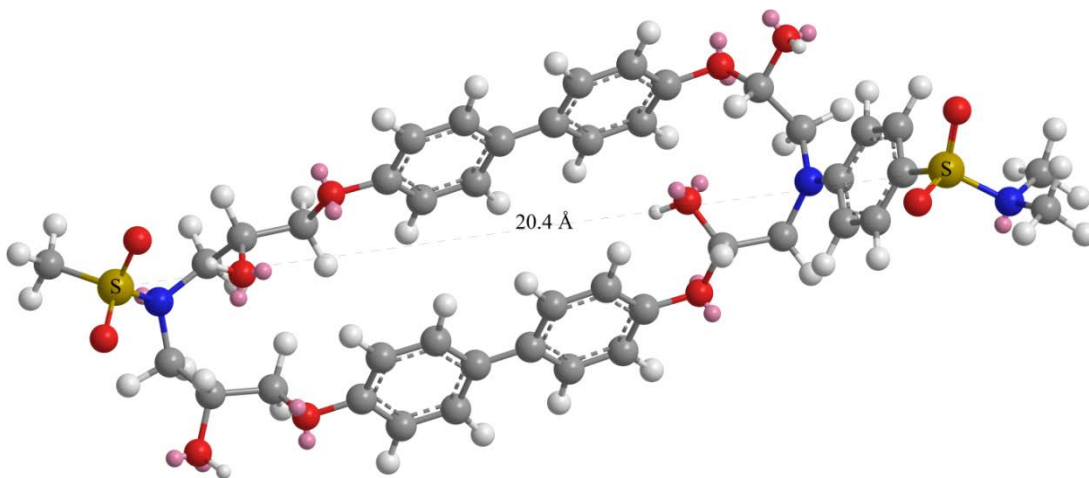


**Figure 4.16** Chemical structure simulation of the mesogen of LCERs.

The dynamic mechanical properties, as well as the glass transition temperature of the resins were investigated using dynamic mechanical analysis (DMA). The storage modulus ( $E'$ ) and loss modulus ( $E''$ ) were determined from the in-phase and out-of-phase response of the resins to an applied strain, representing the elastic and viscous portions respectively. Moreover, the  $T_g$  was measured from the peak of the mechanical damping curve ( $\tan\delta$ ) which was the ratio of  $E''$  to  $E'$ . The DMA curves of the resins cured at different temperatures are shown in **Figure 4.17** and the DMA data is summarized in **Table 4.5**.

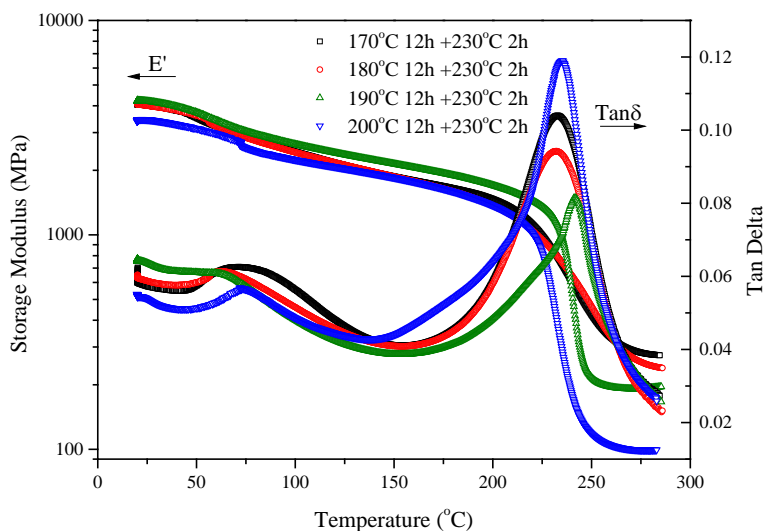


**Figure 4.17** Temperature dependence of dynamic mechanical properties of the resins cured at different temperatures.

**Table 4.5** Thermomechanical data obtained from DMA, DSC and TMA.

Cure schedule	$E'$ at 35 °C (MPa)	$E'$ at 270 °C (MPa)	$T_g^a$ (°C)	$T_g^b$ (°C)	$T_g^c$ (°C)	CTE <sup>d</sup> (°C)	$T_d^e$ (°C)	Remarks
170°C 12h plus 230°C 2h	3975±55	270±8	232.6	206.2	190.8	63.7	306.3	LCER
180°C 12h plus 230°C 2h	3940±14	244±2	231.5	205.2	191.4	69.6	307.0	LCER
190°C 12h plus 230°C 2h	4159±34	196±2	241.2	209.2	191.6	64.9	307.7	LCER
200°C 12h plus 230°C 2h	3422±20	99±0.3	233.3	196.9	183.3	61.1	309.5	Non-LCER

<sup>a</sup> Taken from the peak of  $\tan\delta$  (DMA).

<sup>b</sup> Taken from the intercept of the slopes of glassy region and rubber region (TMA).

<sup>c</sup> Taken from dynamic scans at 20°C/min (DSC).

<sup>d</sup> Measured in the temperature range from 50°C to 70°C via TMA.

<sup>e</sup> At 5% weight loss (TGA)

For semicrystalline polymers, crystallites have a great influence on the elastic modulus of the materials. As shown in **Table 4.5**, LCERs have higher storage moduli in the glassy region (35 °C) compared to non-LCERs, which is due to the presence of LC domains. The rigid and ordered structure of the LC domains has higher moduli compared to the amorphous parts, so they behave as rigid fillers in the resin matrix. LCERs also show higher storage moduli in the rubbery plateau region, which can be attributed to two reasons. First, in addition to the filler effect mentioned earlier, the LC domains also act as crosslinks, tying segments of the polymer chain together. They do not relax or become soft at temperatures higher than  $T_g$ , and therefore the movements of the polymer chains are restricted by these rigid LC domains. Second, the higher rubbery moduli of LCERs could be a result of the reduced viscosity and the accelerated reaction rate when the curing process proceeds in the LC phase, as mentioned previously, which leads to a higher crosslink density for LCERs. The  $T_g$  measured from the peak of the  $\tan\delta$  curve also shows that LCERs have higher  $T_g$  compared to non-LCERs. Both of the rigid filler effect and the crosslink effect are responsible for the high  $T_g$  observed in LCERs. The free volume of the LCERs is significantly reduced due to the presence of LC domains, thereby decreasing the mobility of the segments in response to an applied thermal energy. The  $T_g$  of the resins were also measured using DSC and TMA which is in agreement with the DMA results. In DSC, the  $T_g$  is characterized by a step change in the heat capacity of the material, while in TMA the  $T_g$  is determined in terms of the change in CTE when the material undergoes a change from glass to rubber. Although measured through three different experimental techniques, LCERs always show higher  $T_g$  than non-LCERs. It is noted that the absolute values of  $T_g$  measured in each technique is different, which is not unexpected since the underlying property being monitored is not the same. For example, the  $T_g$  measurement in DSC involves monitoring a thermodynamic property (heat capacity) whereas the  $T_g$  in DMA is obtained from a viscoelastic property ( $\tan \delta$ ).

Thermal expansivity of the LCERs and non-LCERs were evaluated using thermomechanical analysis. Results are summarized in **Table 4.5**. Since thermal history has a great effect on the thermomechanical properties of polymers, all the samples were heated to 250 °C to erase the thermal history and release any internal residual stress. Second heating scans were recoded to examine the CTE of the resins. As shown in **Table 4.5**, the CTE of the resins cured in LC and non-LC state are quite close, which can be attributed to the random distribution of the LC domains in the amorphous matrix.

Thermal stability of the LCERs and non-LCERs was also investigated. **Figure 4.18** shows the TGA curves for all the samples. The thermal decomposition temperature ( $T_d$ ) was defined as the temperature when the samples lost 5% of its initial weight, and the results are summarized in **Table 4.5**. TGA data shows that the presence of LC domains

does not have a significant influence on the thermal stability of the resins, which indicates that the most important factor that affects the thermal decomposition of a polymeric material is the chemical bonding rather than morphology.

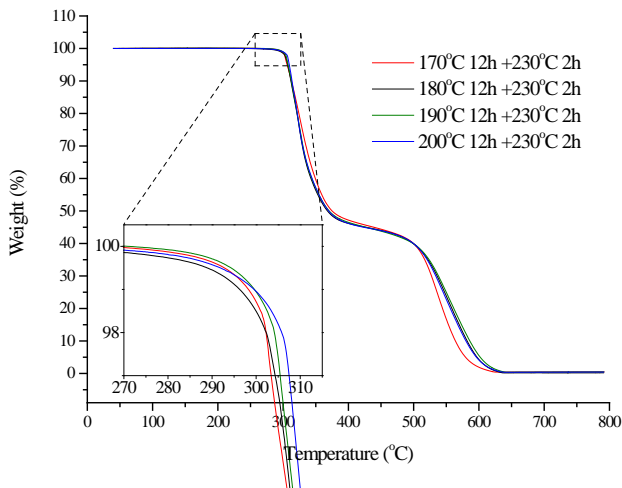


**Figure 4.18** Thermogravimetric analysis of resins cured at different temperatures.

#### 4.3.5 Creep behavior of LCERs

In order to fully understand the reinforcing mechanism of the LC phase, creep behaviors of the LCER and non-LCER were also studied using short-term creep experiments at various elevated temperature isotherms. The Burgers model was utilized to simulate the creep performance of both systems. Parameters extracted from the model were analyzed to explain the reinforcing effect of the LC phase. In addition, the long-term mechanical performance of the material was evaluated by constructing a master curve using the time-temperature-superposition principle.

The time-dependent creep strain values for all resin systems at different temperature intervals are shown in **Figure 4.19**. As can be seen, the creep strain values increased with increasing temperature independent of the type of resin, illustrating the response of the resin networks to applied thermal energy. At temperatures below  $T_g$ , the movement of the polymer networks was greatly restricted by the crosslinking sites; therefore, all systems exhibited limited strain behavior. At high temperatures, on the other hand, the networks were thermally activated and became soft, allowing larger deformation. It was also seen that the creep behaviors of the LCER and the non-LCER were not identical, especially at higher creep temperatures, indicating the influence of the LC phase on the viscoelastic properties of the resins.

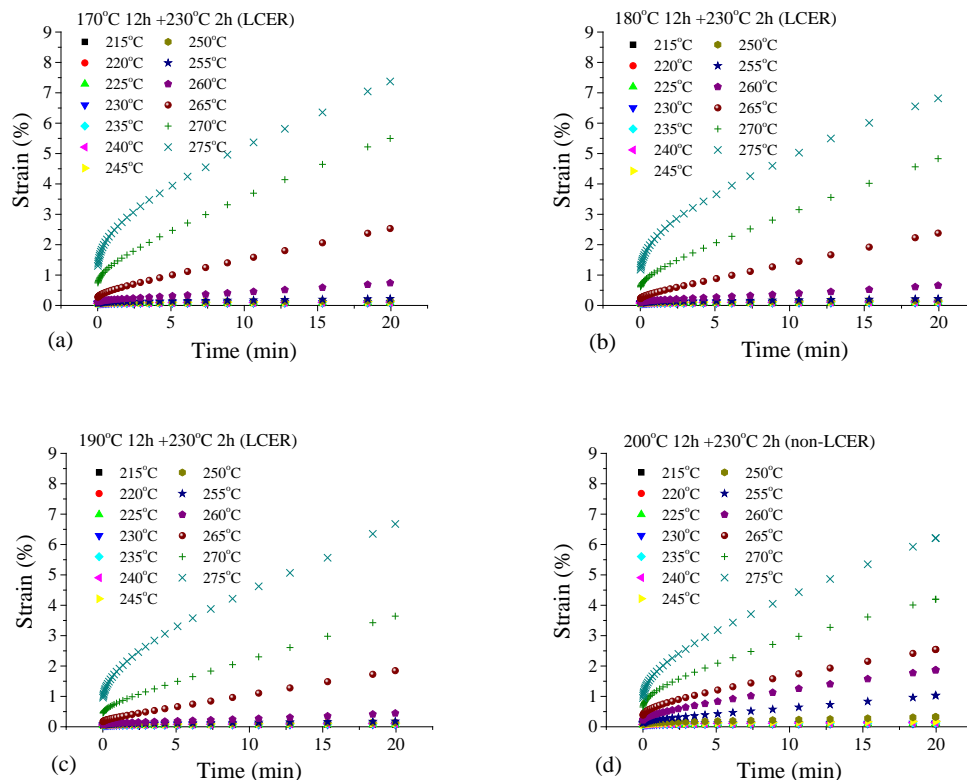


**Figure 4.19** Time-dependent creep strain of the resins at different temperature intervals. (a) LCER cured at 170 °C; (b) LCER cured at 180 °C; (c) LCER cured at 190 °C; (d) non-LCER cured at 200 °C.

In addition to creep strain, the creep strain rate is another important factor that determines the dimensional stability of a material. In general, the creep behavior of polymers can be divided into four stages: instantaneous response, primary creep, secondary creep, and tertiary creep. The instantaneous response is a result of the elastic deformation of a material. Primary creep is caused by the slippage and orientation of the polymer chains. Secondary creep is characterized by a steady-state creep evolution, where a balance between thermal softening and work hardening is established. Tertiary creep involves the rupture or necking of a material, and is accompanied by large deformation. Characterized by a relative linear strain-time relationship, the secondary creep stage is often used to determine the creep strain rate of a material.

In order to relate the different responses of the LCER and non-LCER systems to the applied load, the secondary creep stage in the original creep curves was fitted with a linear line to determine the creep strain rate of each system. The fitting region was carefully selected to ensure that the creep behavior reached a steady state. The fitting results were then plotted as a function of temperature ranging from 215 °C to 275 °C. Four different temperature regions were identified based on  $T_g$  of the resins as shown in **Figure 4.20**. In general, an increase of creep strain rate with temperature was observed, suggesting the increased mobility of the resin networks at elevated temperatures. However, the LCER systems exhibited lower creep strain rate values than the non-LCER system for

temperatures lower than 265 °C as shown in **Figure 4.20(a), (b), and (c)**, indicating improved creep resistance of the LCER systems.

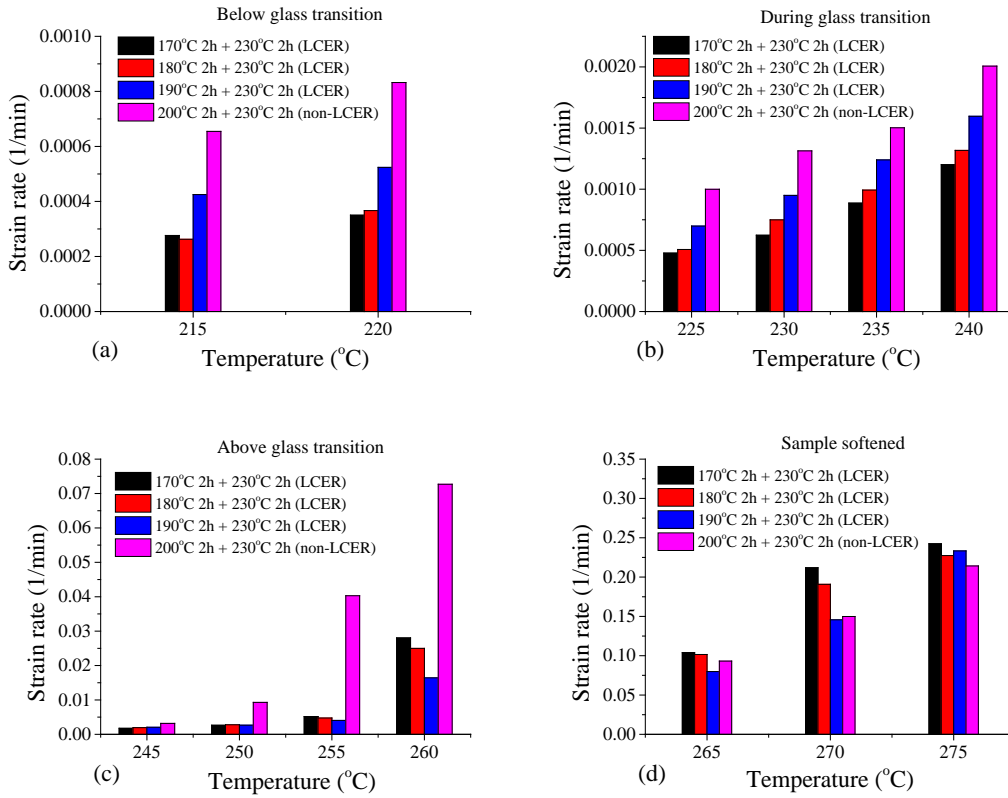


**Figure 4.20** Temperature dependence of creep strain rate. (a) Below glass transition; (b) During glass transition; (c) Above glass transition; (d) Sample softened.

Furthermore, this difference in creep strain rate between two systems exhibited a temperature dependence as shown in **Table 4.6**, suggesting that the reinforcing mechanism of the LC phase might be different at different temperature regions. For instance, below glass transition (from 215 °C to 220 °C), the ratio of average creep strain rate value of LCER to non-LCER was 0.503, while during glass transition (from 225 °C to 240 °C), the ratio increased to 0.652, indicating that the creep-resistant effect of the LC phase became less effective. However, above glass transition (from 245 °C to 260 °C), the ratio decreased to 0.273, suggesting that the reinforcing effect of the LC phase was particularly strong after  $T_g$ . At temperatures higher than 265 °C, the two systems exhibited similar creep strain rates, because the resins softened at these temperatures. The presence of the LC phase was no longer able to restrict the motion of the resin networks, and thus lost its reinforcing effect.

**Table 4.6** Average creep strain rate values of LCER and non-LCER systems at different temperature regions.

Temperature regions	Average creep strain rate value of LCER (1/min)	Average creep strain rate value of non-LCER (1/min)	Ratio of creep strain rate value of LCER to non-LCER
Below glass transition	0.000349	0.000695	0.503
During glass transition	0.000900	0.001380	0.652
Above glass transition	0.008291	0.030415	0.273
Sample softened	0.162933	0.142167	1.146

The Burgers model, also known as the four-parameter model, is widely used to simulate the creep behavior of polymers. It consists of a consecutively connected Maxwell and a Kelvin unit, as illustrated in **Figure 4.21**.

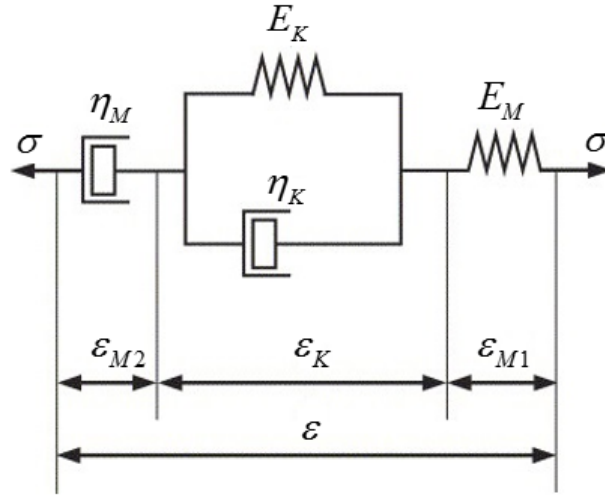


**Figure 4.21** Schematic representation of the Burgers model.

Under a constant applied stress, the total strain of the system is the sum of the strains resulting from the Maxwell spring, the Maxwell dashpot, and the Kelvin unit shown in the figure:

$$\varepsilon = \varepsilon_{M1} + \varepsilon_{M2} + \varepsilon_K \quad (1)$$

where  $\varepsilon_{M1}$ ,  $\varepsilon_{M2}$ , and  $\varepsilon_K$  are the strains of the Maxwell spring, Maxwell dashpot, and the Kelvin unit, respectively. The strain-time relationship can be expressed by the four parameters in Burgers model:

$$\varepsilon = \frac{\sigma_0}{E_M} + \frac{\sigma_0}{E_K}(1 - e^{-t/\tau}) + \frac{\sigma_0}{\eta_M}t \quad (2)$$

where,  $\tau = \eta_K / E_K$  is the retardation time of the Kelvin unit;  $E_M$  and  $\eta_M$  are the modulus and viscosity of the Maxwell spring and dashpot;  $E_K$  and  $\eta_K$  are the modulus and viscosity of the Kelvin spring and dashpot. The three terms in the equation represent the instantaneous deformation, delayed deformation, and viscous flow of a material, respectively.

The four parameters in Equation 2 can be extracted through direct modeling of the experimental creep data, which provide valuable insight into the viscoelastic properties and related deformation mechanisms of a material. The fitting process was accomplished using the nonlinear curve fit function provided by Origin software and the results are shown in **Figure 4.22**. The creep behavior of the resins was well simulated by the Burgers model at all temperatures examined with a correlation coefficient, R, greater than 0.99. Similar to the results of the creep strain rate, a decrease in creep strain value was observed for all LCER systems at temperatures lower than 265 °C. The reinforcing effect of the LC phase was dependent on temperature, as discussed in the previous section; therefore the four parameters extracted from the Burgers model are plotted as functions of temperature for all resin systems, and the results are shown in **Figure 4.23**.

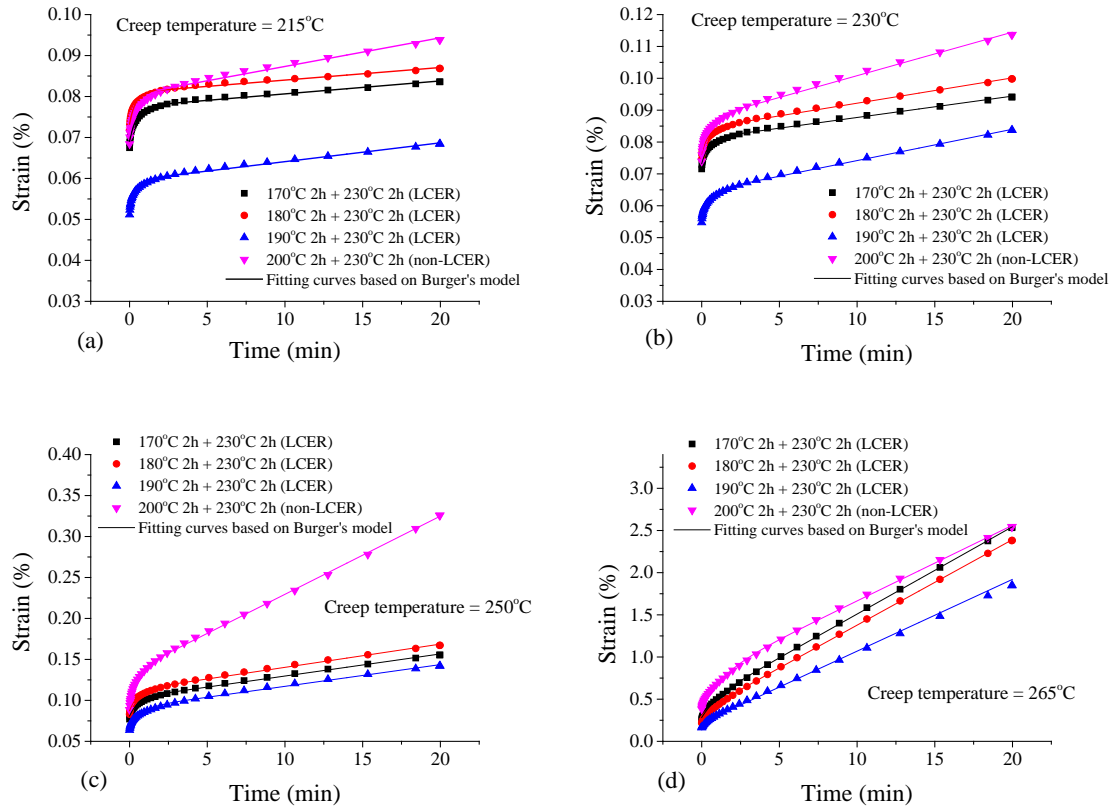


**Figure 4.22** Modeling results of creep behavior at different creep temperatures. (a)  $T_{\text{creep}}=215\text{ }^{\circ}\text{C}$  (below glass transition); (b)  $T_{\text{creep}}=230\text{ }^{\circ}\text{C}$  (during glass transition); (c)  $T_{\text{creep}}=250\text{ }^{\circ}\text{C}$  (above glass transition); (d)  $T_{\text{creep}}=265\text{ }^{\circ}\text{C}$  (sample softened).



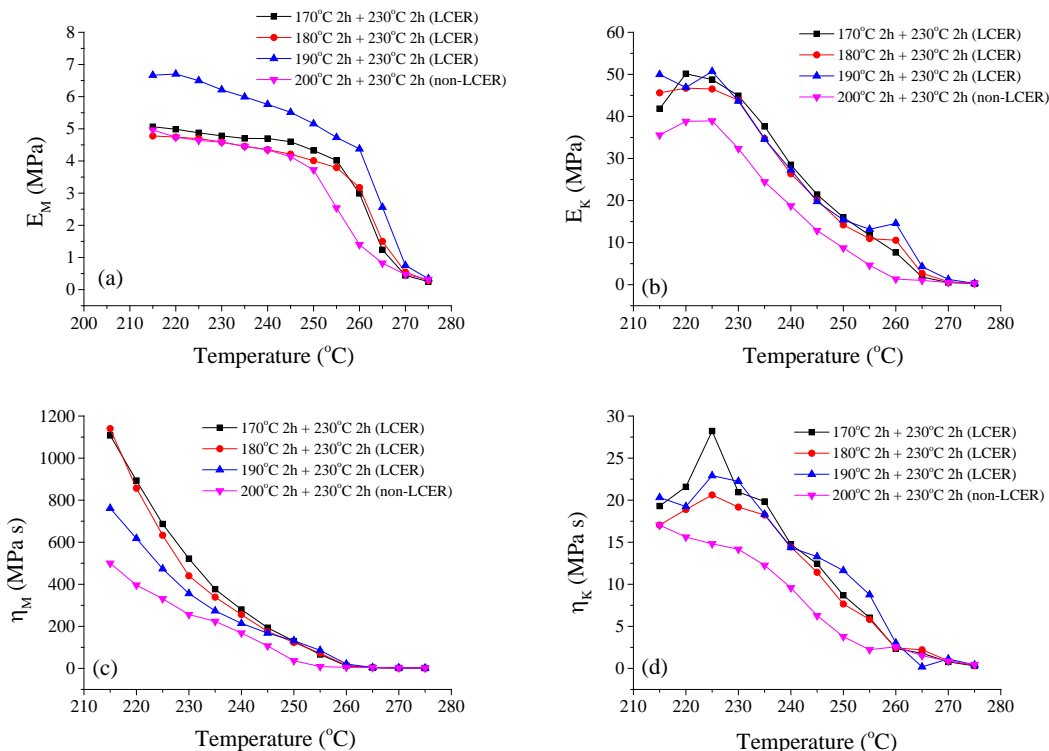


**Figure 4.23** Temperature dependence of the four parameters in the Burgers model. (a) Instantaneous elasticity  $E_M$ ; (b) Retardant elasticity  $E_K$ ; (c) Permanent flow viscosity  $\eta_M$ ; (d) Retardant viscosity  $\eta_K$ .

The parameter  $E_M$  represents the modulus of the Maxwell spring and reflects the instantaneous elasticity of the material. As shown in **Figure 4.23(a)**,  $E_M$  values decreased with increasing temperature for all resin systems, which again illustrated the thermal softening process of the resin networks at elevated temperatures. It was also seen that the LCER systems generally exhibited higher  $E_M$  values than the non-LCER system, indicating the reinforcing effect of the LC phase on the instantaneous elasticity of the resins. Our previous investigation showed that the LCER system had a polydomain structure with individual smectic LC domains randomly distributed in the amorphous networks. These smectic LC domains were composed of rigid LC mesogens that were closely packed in a layered manner. It is believed that the modulus of the LC domains was higher than that of the amorphous regions, and thus behaved as rigid fillers in the resin matrix. In addition, the simulation results were in good agreement with our earlier findings from dynamic mechanical analysis (DMA), in which higher storage moduli ( $E'$ ) were observed for the LCER systems in the glassy region, an indication of increased elastic modulus of the LCER. However, it should be noted that at temperatures higher than 265 °C, the LC phase lost their reinforcing effect because at these temperatures the networks were extremely softened. Another interesting observation is that although  $E_M$  curve and  $E'$  curve shared similarities, they showed different transition temperatures, which was considered to be related with the underlying properties they are representing. In DMA, storage modulus is a measure of the

energy stored and recovered in cyclic loadings. In addition to the contribution of liquid crystalline phases to the stored elastic energy, regions with highly crosslinked networks will also have in-phase response under cyclic loadings. While in Burgers model,  $E_M$  represents the elastic modulus of the Maxwell spring, which is mainly associated with the liquid crystalline regions. Therefore,  $E'$  curve exhibits a sharp drop at 230 °C - 250 °C, whereas  $E_M$  curve shows a sharp drop at 260 °C - 270 °C. However, both parameters ( $E'$  and  $E_M$ ) are closely related with the time-independent elastic response of the resin to external forces, and thus exhibited similar temperature responses.

The parameters  $E_K$  and  $\eta_K$  represent the modulus and viscosity of the Kelvin spring and dashpot, respectively. In the Kelvin unit, the two elements are connected in parallel and instantaneous deformation is restricted because the presence of the dashpot. Therefore,  $E_K$  and  $\eta_K$  are associated with the mechanical properties of the amorphous regions in the resin. They cannot exhibit effective instantaneous response to an applied load, but provide time-delayed support to the network through slow reorientation. Figure 4.23(b) and (d) show that LCERs generally exhibited increased values of both  $E_K$  and  $\eta_K$ . A possible reason for this improvement is the increased crosslink density of the LCER system. In a previous work, it was found that the LCER system had higher total enthalpy of curing reaction compared to that of the non-LCER system and the formation of a LC phase led to a decrease in activation energy of the reacting system, which was considered to facilitate the curing reaction and result in higher degree of reaction. Additionally, the curve of  $\eta_K$  is similar to the loss modulus ( $E''$ ) curve determined by DMA. Both parameters are related with the time-dependent viscous response of the resin to external forces. The parameter  $\eta_K$  represents regions with slow deformation.  $E''$  represents the energy dissipated in cyclic loading. Since both slow deformation (related with  $\eta_K$ ) and permanent deformation (related with  $\eta_M$ ) are considered to be out-of-plane responses, they result in energy dissipation. However, in highly crosslinked thermosets, permanent deformation is restricted and slow deformation is the main cause for energy dissipation. Therefore, the curve of  $\eta_K$  and the curve of  $E''$  exhibited similar shapes.

Among the four Burgers model parameters,  $\eta_M$  is probably most important because it represents the irrecoverable deformation of the material. Figure 4.23(c) compares this parameter for the LCER and the non-LCER. It can be seen that LCER systems exhibited increased values of  $\eta_M$ , indicating the resistance to viscous flow, which was attributed to the crosslinking effect of the LC phase. Unlike in nanoparticle reinforced polymer matrix composites, which often have insufficient particle-matrix bonding, the LC domains in this system had covalently bonded with the amorphous matrix, because the rigid mesogens were physically involved in the crosslinking reaction and became an inseparable part of the resin system. Under an applied load, the LC domains can act as crosslinks, tying the amorphous regions together, and greatly restricting the mobility of the network. This reinforcing effect is more effective at temperatures above  $T_g$  because the LC domains do not relax or become soft at elevated temperatures. Therefore, the LCER systems were more resistant to permanent creep deformation compared to the non-LCER system.

Long-term performance and durability are of particular importance for structural materials; however, it is impractical to perform creep experiment covering the entire service life time. The prediction of long-term properties based on relatively short-term experimental data is necessary and favorable. The time-temperature superposition (TTSP) principle is commonly used to study the time-dependent mechanical properties of polymers. It is worth mentioning that TTSP exhibits limitations when multi-phase systems are studied, especially in inhomogeneous systems. However, TTSP can be applied to multi-component systems which are homogeneous and isotropic. Our previous studies on this LCER system showed that there was no observable phase separation. Although local orientation was present in individual LC domains, the whole system is isotropic. Therefore, the TTSP can be applied to the current LCER system. According to the TTSP principle, a creep experiment conducted at an elevated temperature is equivalent to one performed for an extended period of time. Therefore, the short-term creep test data collected at different temperature isotherms can be used to construct a master curve that provides a prediction for long-term performance of a polymeric material.

The dependence of creep compliance on actual experiment duration for a LCER cured at 170 °C is shown in **Figure 4.24**. The time intervals between two creep temperatures represent the recovery process and the equilibrium time used to reach the desired temperature. The creep compliance data were then manually shifted to construct a master curve at a reference temperature of 215 °C on a log-time scale, as shown in **Figure 4.25**. For the creep experiments carried out at the temperatures higher than 215 °C, the data were shifted to the right, representing the creep behavior for an extended period of time.

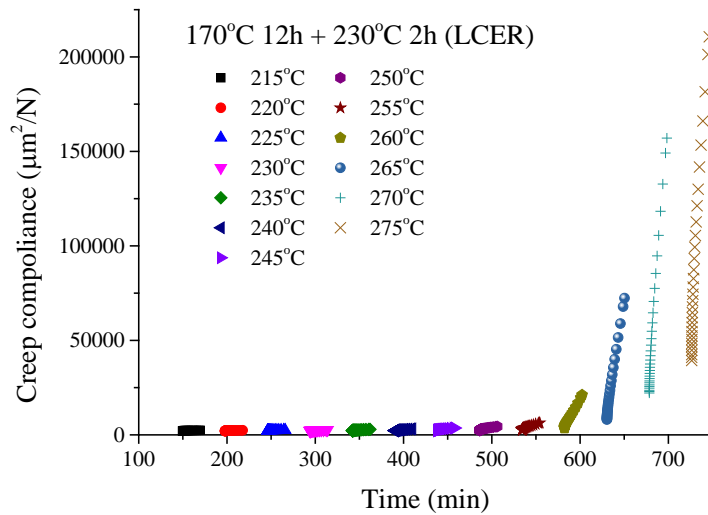


**Figure 4.24** Dependence of creep compliance on creep time at different temperature intervals for LCER cured at 170 °C.

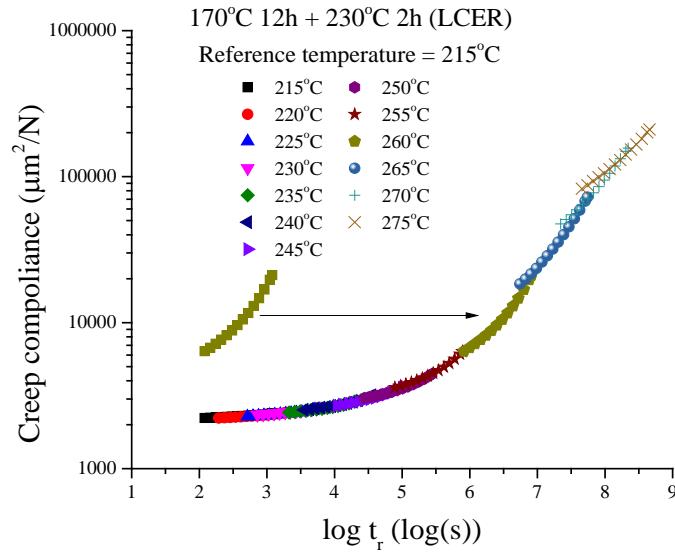


**Figure 4.25** Manually shifted creep compliance data for the LCER cured at 170 °C at a reference temperature of 215 °C.

In order to determine the long-term performance of the resins, the master curves generated for all systems at a reference temperature of 215 °C are shown in **Figure 4.26** with lines representing times of 1 month, 1 year, and 10 years, respectively. As can be seen, the LCER systems exhibited a lower values of predicted creep compliance, illustrating the reinforcing effect of the LC phase on the creep resistance of the material.

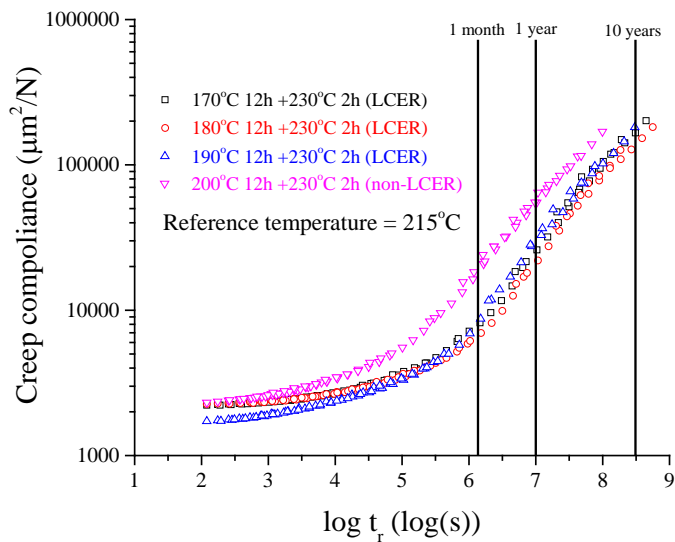


**Figure 4.26** Master curves generated from manually shifted creep compliance data for the LCER and non-LCER systems.

## 4.4 Conclusions

A biphenyl-based epoxy monomer BP was synthesized and characterized using various experimental techniques. Results show that BP is not a liquid crystalline epoxy monomer itself and an irreversible crystal transition exists in the temperature range of 120 °C - 140 °C. However, upon reacting with SAA, a smectic LC phase starts forming after 20 minutes of the curing reaction. Cure temperature has a great influence on the formation and development of LC phase and an isotropic network is obtained for cure temperatures greater than 200 °C. A rate acceleration of the curing reaction was observed for the resins cured in the LC phase. The curing reaction of BP with SAA was investigated in detail. DSC studies showed that the curing condition had a significant influence on the structure of the epoxy resins. At low heating rates (1 - 4 °C /min), the formation of a LC phase was observed upon curing. While at heating rates of 10 °C /min and higher, the LC phase was absent and resins had an amorphous structure. Friedman's isoconversional method was used to analyze the dynamic DSC data. Based on the ICM results, multi-step reaction models were developed to model the curing reaction for both LCERs and non-LCERs. It was found that the formation of a LC phase led to a decrease in activation energy, facilitating the curing reaction and resulting in higher degree of reaction. The effects of the presence of LC phase on the thermal and mechanical properties of the resins were also investigated. LCERs showed higher values of storage modulus in both glassy region and rubbery plateau region compared to non-LCERs, which is due to the rigid structure of the LC domains and reduced viscosity of the system. The glass transition temperature of the resins cured in LC and non-LC state was studied using DMA, DSC, and TMA respectively. All the results show that LCERs have higher  $T_g$  because of the rigid filler and crosslink effects of the LC domains, which results in lower mobility of the polymer chain. The presence of LC phase does not have a significant influence on the coefficient of thermal expansion and thermal stability of the resins, possibly due to the random distribution and orientation of the LC domains. The creep behavior of a LCER and a non-LCER prepared from the epoxy monomer was investigated at different temperature isotherms. The Burger model was used to simulate the creep performance of both systems. The long-term creep compliance was evaluated using the time-temperature superposition principle. The study revealed that the presence of a LC phase can improve creep resistance of the resins. The experimental results showed that, compared to the non-LCER, the LCER systems exhibited a decrease in both creep strain and creep rate at the same temperature. The modeling revealed that the introduction of the LC phase into the resin network is an effective approach to reinforce the viscoelastic properties of the resin, including instantaneous elasticity, retardant elasticity, and permanent deformation resistance. The rigid filler effect and the crosslinking effect of the LC phase are considered to be two important self-reinforcing mechanisms. In addition, the resins cured in LC phase showed improved long-term performance and durability.

## **Chapter 5: Magnetic Field Processing of Highly Crosslinked Liquid Crystalline Epoxy Resins with tailor thermomechanical properties**

### **5.1 Introduction**

Orientation is a phenomenon of great theoretical and technical importance in polymer science. Oriented polymers are usually highly anisotropic and possess excellent physical properties. Various techniques have been utilized to induce molecular orientation in polymers, including surface field orientation, electric field orientation, and magnetic field orientation. Low molecular weight thermotropic liquid crystals exhibit temperature-dependent phase behavior and show active response to magnetic fields because of the molecular anisotropy of their diamagnetic susceptibility. When these liquid crystalline (LC) molecules are combined with appropriate functional groups, they become reactive and can be polymerized into networks to retain their LC structure and molecular orientation. Liquid crystalline epoxy resins (LCER) are a special class of thermosetting polymers; they combine the characteristics of thermally reactive epoxies and magnetically responsive liquid crystals, and can be oriented using various techniques. Thermomagnetic processing is an innovative technology that combines the application of magnetic fields with conventional high frequency electromagnetic thermal processing. It allows the customization of the structure of the material at micro-scale and nano-scale levels in order to tailor the properties and performance of the material. Thermomagnetic processing technology has been successfully used with alloys to selectively control microstructure stability and phase transformation kinetics<sup>91-93</sup>. However, the utilization of this technology with polymeric materials has not been fully explored, and therefore the ability to control molecular orientation of the polymer matrix in advanced composites is expected to enable unique mechanical, thermal, and electric properties of structural and functional composites. In the work reported herein, the use of thermomagnetic processing with a biphenyl-based LCER system was investigated. The structure of the oriented LCER was characterized using two dimensional X-ray diffraction (2D-XRD), and it was correlated with mechanical and thermomechanical properties determined by nanoindentation tests and thermomechanical analysis.

### **5.2 Methodology**

#### **5.2.1 Materials**

Benzyltrimethylammonium bromide, 4,4'-dihydroxybiphenyl with 97% purity, and sulfanilamide (SAA) were purchased from Sigma-Aldrich (Milwaukee, WI). Epichlorohydrin with 99% purity was obtained from Acros Organics (Belgium). Sodium hydroxide, isopropyl alcohol, chloroform, methanol, and acetone were supplied by Fisher Scientific (Fair Lawn, NJ). All chemicals were used as received without further purification. The epoxy monomer, 4,4'-diglycidyloxybiphenyl (BP), was synthesized according to a procedure reported in the previous chapter.

#### **5.2.2 Thermomagnetic processing**

Thermomagnetic processing of the LCER was conducted at Oak Ridge National Laboratory using a superconducting magnet system, schematically shown in **Figure 5.1**. The magnetic field was created by coils of superconducting wires. A metallic susceptor was used as the heat source, converting electromagnetic energy into thermal energy, and therefore allows simultaneous curing and alignment of the LCER. Thermomagnetic processing was performed in a 9 Tesla superconducting magnet with a 127 mm diameter horizontal warm bore. Electromagnetic energy was supplied by a 9 kW power supply set to resonate at 175 kHz when coupled with an applicator. The thickness of the susceptor was 10x the skin depth in order to shield the samples from the intense radiofrequency energy and to make sure they were heated only by radiant energy supplied uniformly by the tubular heating element. Thermomagnetic processing was performed using actively controlled thermal profiles that were designed to reproduce the transient conditions experienced by samples. The AC electromagnetic energy that was coupled to the susceptor was below 300 W during thermomagnetic processing.

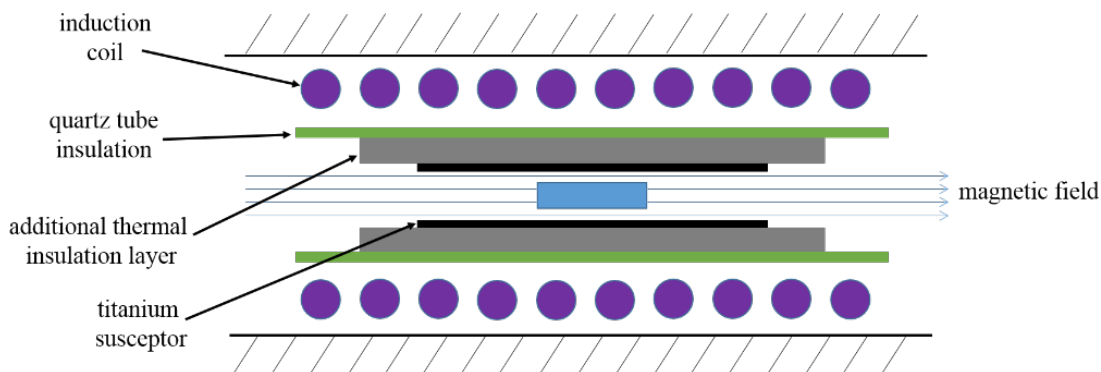


**Figure 5.1** Schematic representation of the thermomagnetic processing system.

In the experiment, the epoxy monomer was placed in a beaker and heated in an oil bath to 170 °C (melting point of BP is 156 °C and melting point of SAA is 165 °C). After the monomer was fully melted, the curing agent was added under a stoichiometric ratio, followed by vigorous stirring for approx. 45 s. The liquid mixture was poured into a PTFE mold and was immediately transferred to the magnetic bore, which was preheated to 140 °C for alignment and curing. Because the reaction is highly exothermic, the pre-heating temperature of 140 °C was chosen to prevent overheating. After 10 min, the temperature was ramped to 170 °C at a rate of 2 °C/min. The oriented LCER was prepared by curing the sample under 9T at 170 °C for 4 h. Unoriented LCER was prepared using the same procedure without a magnetic field.

### 5.2.3 Characterization

The curing behavior and the thermal properties of the LCERs were studied using a Q2000 differential scanning calorimetry (DSC, TA Instruments, Inc.). The DSC cell was purged with helium gas at a flow rate of 25 ml/min. For the glass transition temperature measurements, the first heating scan was used to erase the thermal history. While the second heating scan was recorded to evaluate  $T_g$ .

Rheological measurements of the curing reaction were conducted using an AR2000ex stress-controlled rheometer (TA Instruments, Inc.) with parallel plate geometry and an aluminum plate fixture with a diameter of 25 mm. The aluminum plates were preheated to the curing temperature. Approximately 0.5 g of the powder mixture was placed on the bottom plate, and then the top plate was lowered to a gap of ca. 1mm. Oscillatory experiments were carried out at an isotherm of 150 °C with an amplitude of 1000 Pa and at a frequency of 1 Hz.

The structure and degree of orientation of the LCER were investigated using 2D-XRD. Diffraction patterns were collected using a Bruker D8 Advance Diffractometer in transmission mode. The system was equipped with a HI-STAR area detector and controlled via Bruker software (GADDS version 4.1.44). The X-ray source used in the experiments consisted of a chromium X-ray tube energized via a Kristalloflex 760 generator and maintained at 30 kV and 50 mA. A graphite monochromator was used to tune the source to Cr K $\alpha$  radiation. In the experiment, a 0.8 mm collimator was used to control the divergence of the primary X-ray beam. A 6 x 4 mm specimen was mounted in the transmission fixture at a distance of 40 mm from the collimator assembly. A beam stop was placed 25 mm behind the test specimen. The detector was positioned 15 cm from the specimen. Data was collected by moving the detector in three individual increments (0°, 17° and 34°) in the positive 2 $\theta$  direction. A counting time of 300 s was used for each step. Data was corrected for spatial and flood field aberrations using the GADDS software.

Mechanical properties of the LCERs, both cured with and without magnetic field, were studied using a Hysitron TI 900 nanoindentation system equipped with a Berkovich diamond indenter. A typical load-hold-unload cycle was used for indentation experiments as shown in **Figure 5.2**. Once the indenter tip contacted the sample surface, the load was increased at a constant strain rate of 0.05 s<sup>-1</sup> to 9.5 mN. Then the load was kept constant for 60 s to study the creep behavior of the resins. During the unloading phase, the indenter was withdrawn from the sample at a constant rate of 2 mN/s. A total of 25 indents were made on each sample and the distance between each indent was 40  $\mu$ m to avoid interactions.

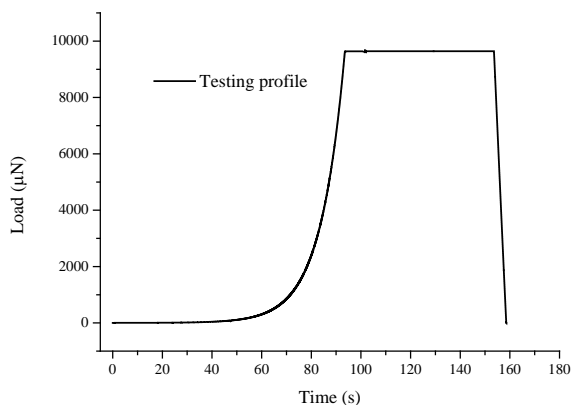


**Figure 5.2** Testing profile used in the nanoindentation experiments.



Thermomechanical properties of the LCERs were studied by measuring the coefficient of thermal expansion (CTE) of the samples using a model Q400 thermomechanical analyzer (TA Instruments). The measurements were conducted in expansion mode with a heat-cool-heat cycle at 5 °C/min. The second heating scan was used to calculate the value of the CTE.

Fracture surfaces of the samples were examined using a scanning electron microscope (FEI Quanta 200F FE-SEM) to evaluate the effect of LC orientation on the fracture morphology of the resin. Samples were sputter-coated with a layer of Au, and SEM images were collected at a 20 kV accelerating voltage.

Dynamic mechanical properties of the LCERs cured with and without magnetic field were studied using a model Q800 dynamic mechanical analyzer (DMA, TA Instruments, Inc.). All the samples were heated from room temperature to 280 °C at 3 °C/min, at a frequency of 1 Hz and an amplitude of 25  $\mu$ m in three-point bending mode.

The thermal stability of the LCERs was investigated using a thermogravimetric analyzer (TGA) on a model Q50 TGA (TA Instruments, Inc.). About 10 mg of resins was placed in an alumina pan and heated from 25 °C to 800 °C at a rate of 20 °C/min under an air purge of 60 ml/min.

## 5.3 Results and Discussion

### 5.3.1 Rheological properties

An isothermal DSC scan was performed to study the curing behavior of BP with SAA. Unlike the curing reaction of conventional epoxy resins which is characterized by a single exothermic peak, two peaks were observed as shown in **Figure 5.3**. The first exothermic peak results from the reaction between an epoxy group of BP and the aromatic amine group of SAA. While the second peak is related to the formation of the LC phase that develops with increasing molecular weight, which has been confirmed in our previous investigation. In order to study the effect of LC formation on the curing reaction, a parallel plate rheology experiment was carried out to examine the phase transition of the curing system. The evolution of complex viscosity, storage modulus ( $G'$ ), and loss modulus ( $G''$ ) during cure is also shown in **Figure 5.3**.

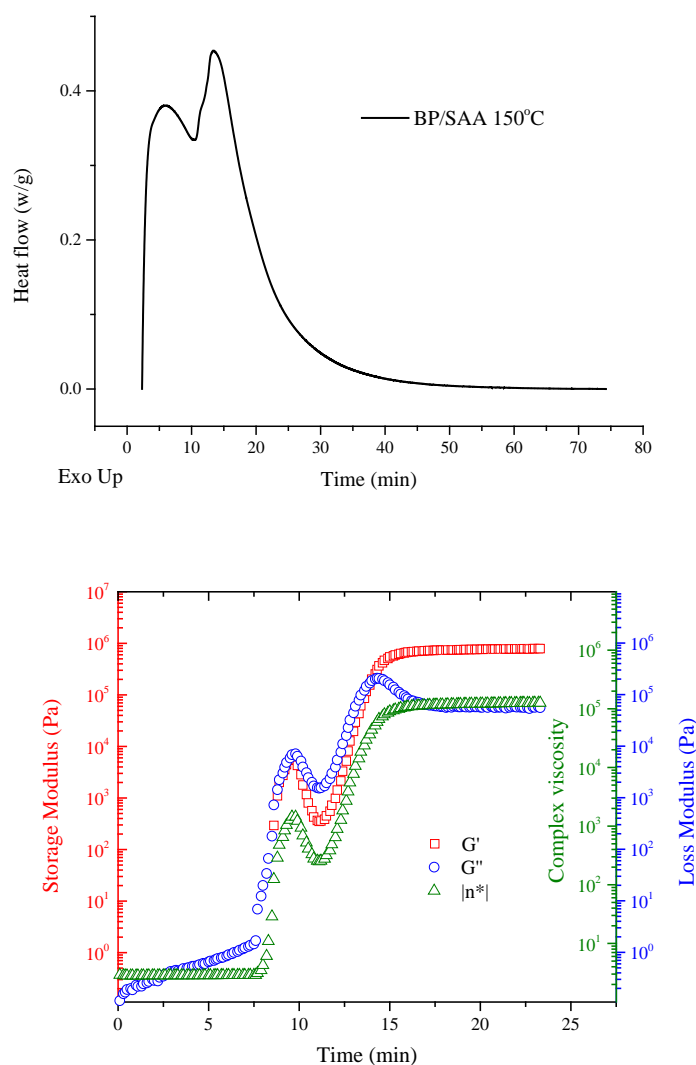


**Figure 5.3** Isothermal DSC curve showing the exothermic cure of BP with SAA at 150 °C (up). Evolution of the complex viscosity, storage ( $G'$ ), and loss ( $G''$ ) moduli as a function of the reaction time at 150 °C (down).

The curing reaction starts immediately after the melting of the two components and the system is initially isotropic. Reaction in the early stage of cure (0-8 min) involves the growth and branching of the polymer chains. In this study, the chain branching is substantially reduced by using SAA as the curing agent, because the two amine groups have unequal reactivity. At this time in the cure, the reacting system behaves like a viscoelastic liquid, therefore only the loss modulus representing the liquid-like part of the system can be observed. As the reaction proceeds (8-10 min), the molecular weight of the polymer chains increases rapidly, leading to a dramatic increase in viscosity of the system as shown in **Figure 5.3**. However, unlike the curing reaction in traditional epoxy resins, which exhibits a continuous increase in viscosity with time, a decrease of viscosity was

observed in the curing process of BP with SAA from ca. 10 min to 12 min. Of particular note is that in the isothermal DSC curing study, the second exothermic peak starts forming after about 10 min of the curing reaction. Concomitant evidence from temperature controlled polarized optical microscopy confirm these findings and were reported in our previous work. Therefore, the decrease of viscosity is readily related to the LC formation. The complex viscosity, storage modulus, and loss modulus of the curing system continue to increase after the formation of LC phase. Further curing leads to gelation, where the reacting system transforms from a viscous liquid to an elastic gel. The gel time can be determined from the crossover point of the storage and loss moduli. For the present system, the gel time was determined to be 15 min. Additionally, the vitrification time of the system is determined from the time when the loss modulus curve reaches its maximum, indicating the transformation of LCERs from a rubbery state to a glassy state, due to the increase of  $T_g$  with time during the curing reaction. After 20 min of cure, both  $G'$  and  $G''$  level off, indicating that no significant additional reaction takes place at this isothermal cure temperature. Based on the DSC and rheology experiments, we could conclude that the formation of the LC phase leads to a decrease in viscosity of the reacting system, thereby facilitating the curing reaction, and resulting in an additional cure exotherm.

### 5.3.2 Structure and morphology

Orientation of LC domains in LCERs usually needs to be carried out before gelation when the mesogens are still able to response to the applied field. Although the gel time of curing reaction between BP with SAA is relatively short, the extremely low initial viscosity of the system is able to facilitate the alignment of the LC domains. The principle of LC orientation under magnetic field is extensively described in the literature. The anisotropy of the diamagnetic susceptibility of the LC molecules and the cooperative motion of the LC mesogens are the driving force for the orientation of LC domains. The orientation of the LCERs was characterized using 2D-XRD, which is widely used to study preferred orientation in polymers. In order to record high resolution diffraction patterns of the smectic layer, the detector was set at  $2\theta = 0^\circ$  to collect inner diffractions. The sample-to-film distance was chosen to be 15 cm. The detector was then moved to  $2\theta = 34^\circ$  to collect outer diffractions. Two samples with different LC orientations were investigated and the original 2D-XRD patterns are shown in **Figure 5.4**. The data was quantified by integrating along the  $2\theta$  direction and the results are shown in **Figure 5.5**.

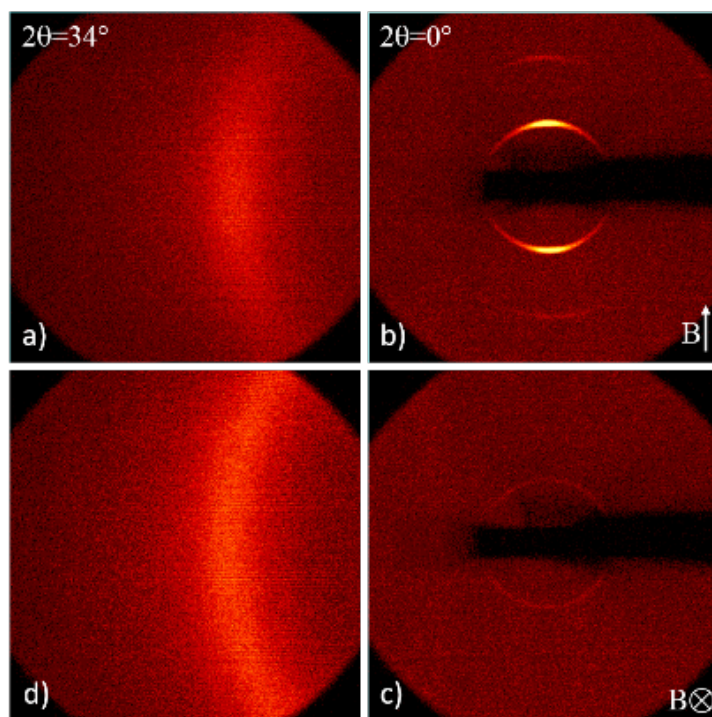


**Figure 5.4** 2D-XRD patterns of oriented LCER with different directions of LC orientation. (a) and (b): incident X-ray beam is perpendicular to the magnetic field direction, (c) and (d): incident X-ray beam is parallel to the magnetic field direction.

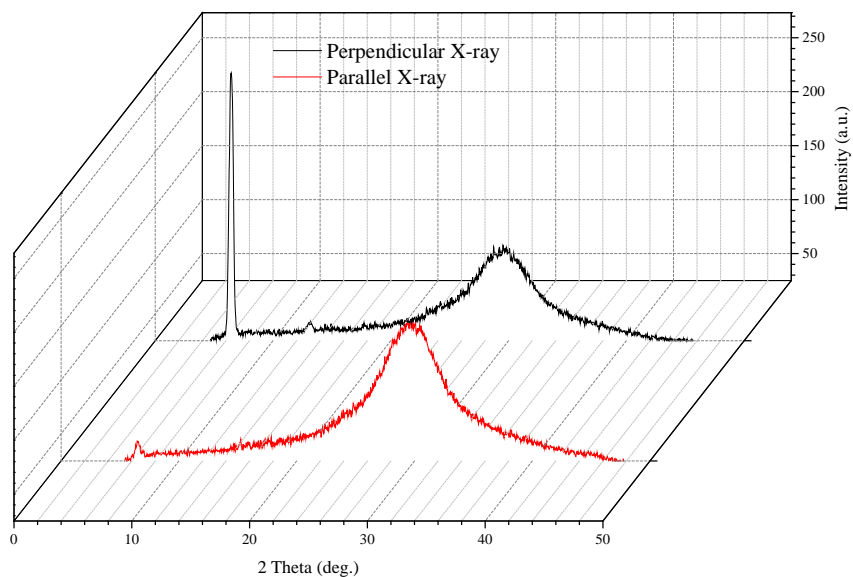


**Figure 5.5** Quantified diffraction spectra after  $2\theta$  integration.

The diffraction behavior was highly dependent on sample orientation, indicating that macroscopic orientation of the LC domains had been achieved. For example, when the incident X-ray beam was perpendicular to the magnetic field direction (**Figure 5.5a, b**), sharp diffraction arcs were observed in the meridional direction at a Bragg angle of  $6.45^\circ$ , caused by the layered smectic LC structure. The d-spacing was calculated to be  $20.3 \text{ \AA}$  according to Bragg's law. The value is quite close to the thickness of the smectic layer calculated from molecular simulation. In addition, a second-order diffraction was observed at a Bragg angle of approx.  $13^\circ$ , suggesting that most of the smectic LC domains were oriented along the applied magnetic field. The samples also showed a diffraction arc in the equatorial direction at a Bragg angle of  $29.5^\circ$  which corresponded to the diffraction from lateral-packed biphenyl mesogens. Because the mesogens within a smectic layer are less regulated, the diffraction arc appeared to be more diffuse compared to the diffraction by the smectic layer. On the other hand, when the X-ray beam was parallel to the field direction (**Figure 5.5c, d**), a very weak diffraction ring was observed in the meridional direction. In the equatorial direction, a diffused diffraction ring was observed instead of a diffraction arc. Under such configuration, the diffraction condition for the smectic layer is no longer satisfied, and the arrangement of the mesogens became effectively isotropic and showed uniform intensity distribution in the diffraction pattern. An explanation for this behavior is schematically shown in **Figure 5.6**. It is worth mentioning that the d-spacing values of oriented LCERs were very close to those of unoriented LCERs, indicating that the application of the magnetic field only affected direction, not the internal structure of the LC domains.

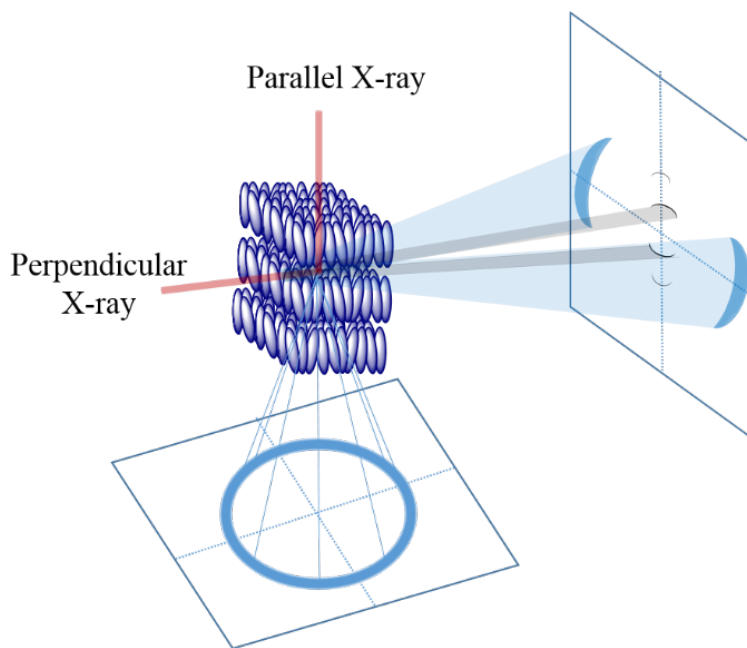


**Figure 5.6** Schematic illustration of the diffraction patterns of a smectic LC domain.

The degree of orientation of the LCER was evaluated based on the azimuthal intensity distribution of the inner diffraction arc from the smectic layer. An order parameter  $S$  was calculated according to Herman's method:

$$S = \frac{1}{2}(3\langle \cos^2 \alpha \rangle - 1) \quad (1)$$

$$\langle \cos^2 \alpha \rangle = \frac{\int_0^{\pi/2} I(\alpha) \cdot \sin \alpha \cdot \cos^2 \alpha \cdot d\alpha}{\int_0^{\pi/2} I(\alpha) \cdot \sin \alpha \cdot d\alpha} \quad (2)$$

where  $\alpha$  is the angle between the smectic layer normal and the magnetic field.  $I(\alpha)$  is the intensity distribution of the sample; it can be directly calculated from the azimuthal intensity distribution of the diffraction arc. The degree of orientation of the LCER after thermomagnetic processing was determined to be 0.32, which was assumed to have significant influence on the mechanical properties of the material.

As discussed in the previous section, the mesogens within a smectic layer were mainly connected by van der Waals forces, whereas the mesogens in different layers were connected through covalent bonds. Therefore, the fracture behavior of the resin was expected to be influenced by the LC orientation. As shown in **Figure 5.7**, the fracture morphology of the resin was highly dependent on fracture direction. When the resin was fractured in the direction perpendicular to its orientation direction (**Figure 5.7b**), crack propagation was redirected and changes to the direction of orientation so that the propagating cracks had to overcome only relatively weak van der Waals bonds rather than primary covalent bonds.

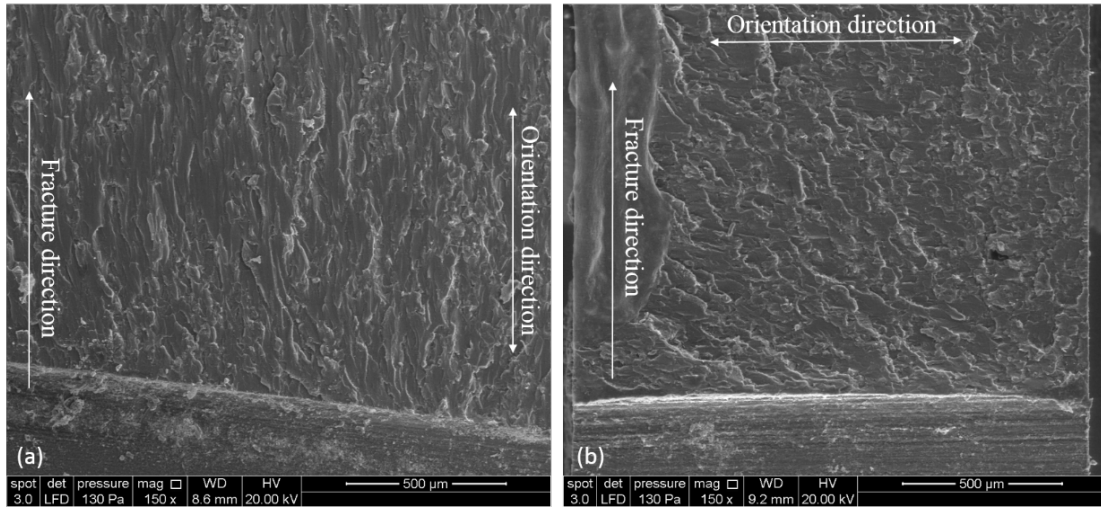


**Figure 5.7** Effect of LC orientation on fracture morphologies of the LCERs. (a) Fracture direction is parallel to LC orientation; (b) Fracture direction is perpendicular to LC orientation.

In general, smectic LC phases exhibited layered structures. During the SEM experiments, several layered structures were observed on the fracture surface, shown in **Figure 5.8**. These layers were stacked along the direction of orientation and were

independent of fracture direction. It was concluded that these layered structures were related to the oriented smectic LC domains after magnetic field processing.

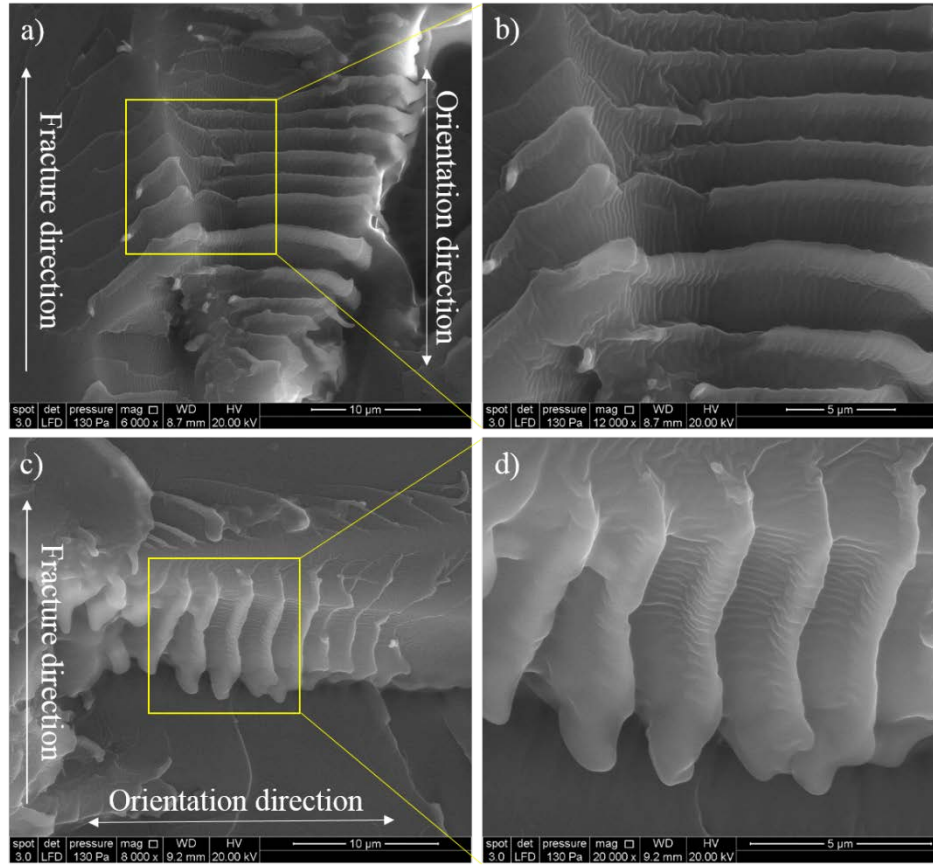


**Figure 5.8** Effect of LC orientation on fracture morphologies of the LCERs. (a) and (b): Fracture direction is parallel to LC orientation; (c) and (d): Fracture direction is perpendicular to LC orientation.

### 5.3.3 Thermal and mechanical properties

The mechanical properties of the LCERs were studied using nanoindentation. For the sample prepared by thermomagnetic processing, the mechanical behavior, both in longitudinal and transverse direction, was investigated and compared to that of unoriented LCERs. The load-displacement profiles of the samples are shown in **Figure 5.9(a), (b), and (c)**, depicting the behavior of unoriented LCER, and of oriented LCER in the longitudinal direction, and the transverse direction, respectively. The figure shows that the three samples exhibited different mechanical responses under the same loading profile, illustrating the influence of molecular orientation on mechanical properties of the resin. The load-displacement curves of unoriented LCER were more consistent than those of oriented LCERs. This was attributed to the random orientation and distribution of the LC domains, which resulted in a material with isotropic and homogeneous properties. In the case of oriented LCERs, the use of a magnetic field caused macroscopic orientation. However, the orientation process was affected by several factors, such as the thermal

agitation of the LC molecules and the crosslinking reaction with the curing agent. The LC domains may not have been perfectly aligned along the field direction, and each domain may exhibit a different angle with respect to the magnetic field direction. This localized inhomogeneity in terms of LC orientation resulted in the variation of indentation behavior observed in **Figure 5.9(b)** and (c).

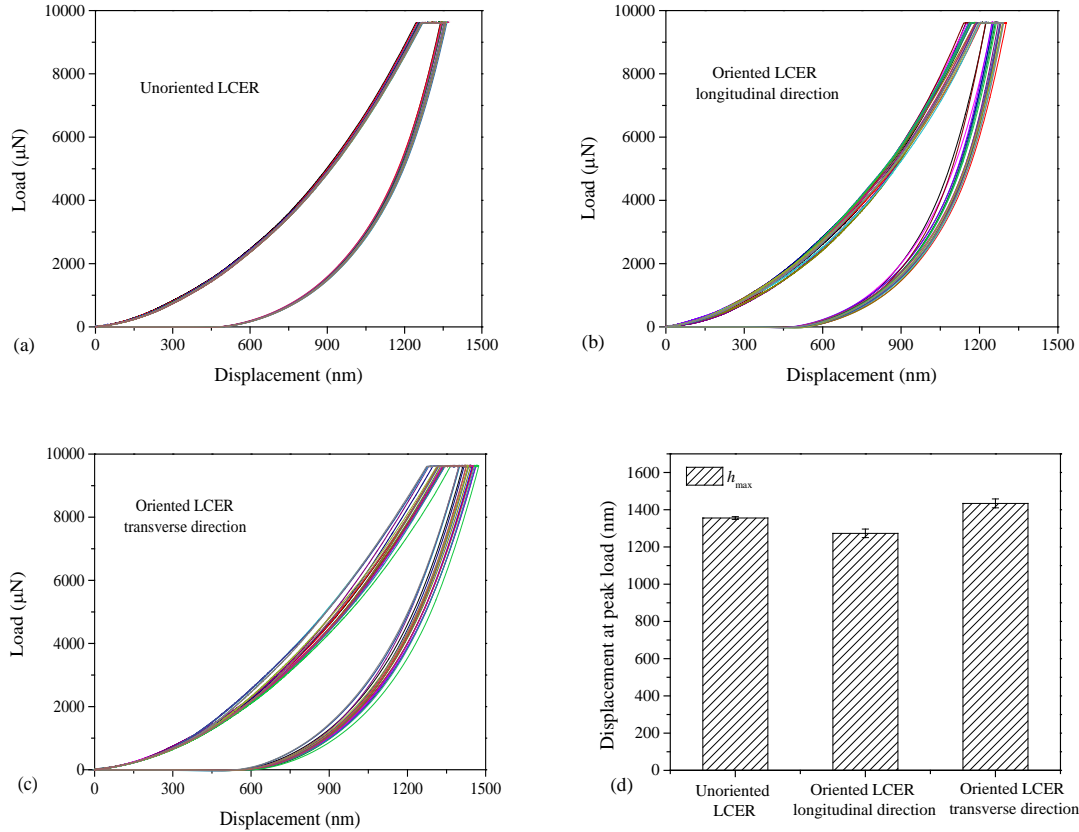


**Figure 5.9** Load-displacement profiles and indentation displacement of LCER samples. (a) Unoriented LCER; (b) Oriented LCER longitudinal direction; (c) Oriented LCER transverse direction; (d) Displacement of LCER samples at peak indentation load.

An important parameter in nanoindentation experiments is the displacement at peak load,  $h_{max}$ , which represents the resistance of a material to mechanical deformation. The displacement results for all samples are plotted in **Figure 5.9(d)**. Here the LCER oriented in the longitudinal direction showed the lowest value of  $h_{max}$  under the same loading profile, indicating higher resistance to deformation in the direction of orientation. The existence of rigid and oriented LC domains contributed to this behavior to be further discussed in the next section.



A detailed analysis of the nanoindentation data was carried out according to a procedure developed by Oliver and Pharr, fitting the unloading curves using a power-law equation:

$$P = \alpha(h - h_f)^m \quad (3)$$

where  $P$  is the indentation load,  $h$  is the displacement,  $m$  and  $\alpha$  are fitting parameters. Then the contact stiffness ( $S$ ) was determined from the initial slope of the unloading curve.

$$S = \frac{dP}{dh}(h = h_{\max}) \quad (4)$$

The contact area ( $A$ ) was determined using the shape function of the Berkovich indenter:

$$A(h_c) = 24.56h_c^2 + C_1h_c^1 + C_2h_c^{1/2} + \dots + C_6h_c^{1/32} \quad (5)$$

where  $h_c$  is the contact depth.  $C_i$ s are parameters determined from calibration. The first term describes the contact area of a perfect Berkovich indenter; the others are correcting terms reflecting tip-blunting. The reduced elastic modulus was calculated and correlated to the sample modulus by the following equations:

$$E_r = \frac{1}{\beta} \frac{\sqrt{\pi}}{2} \frac{S}{A} \quad (6)$$

$$\frac{1}{E_r} = \frac{1 - \nu_s^2}{E_s} + \frac{1 - \nu_i^2}{E_i} \quad (7)$$

where  $E_i$  (1141 GPa) and  $\nu_i$  (0.07) are the elastic modulus and Poisson's ratio for the diamond indenter.  $E_s$  and  $\nu_s$  are the same properties for the sample. In this experiment, the Poisson's ratio of the resin was set to be 0.35 to calculate the elastic modulus.

The hardness of the sample was defined as the peak load divided by contact area and was calculated as

$$H = \frac{P_{\max}}{A} \quad (8)$$

The elastic modulus and hardness of the LCERs are shown in **Figure 5.10**. After magnetic processing the LCER exhibited anisotropic mechanical behavior. In the longitudinal direction, the resin showed an improvement of 24.6% in elastic modulus and an improvement of 7.4% in hardness compared to the unoriented LCER. In the transverse direction, however, modulus and hardness of the oriented LCER showed a decrease of 13.5%

and 7.8%, respectively. These changes were closely related to the orientation of the LC molecules. As shown in **Figure 5.6**, the smectic LC domain consisted of laterally packed, layered biphenyl mesogens. The mesogens in different layers were covalently connected through sulfanilamide molecules, whereas the mesogens in the same layer were bonded by van der Waals forces such as pi stacking. Therefore, the modulus and hardness of a single LC domain were expected to be anisotropic. In the unoriented LCER, the LC domains were randomly distributed, and the anisotropy of the LC domains was neutralized. After magnetic processing, however, the original properties of the LC domains were retained and transferred from the micro-scale to the macro-scale, resulting in a resin network with anisotropic mechanical behavior. Other mechanical properties investigated using the nanoindentation tests are summarized in **Table 5.1**.

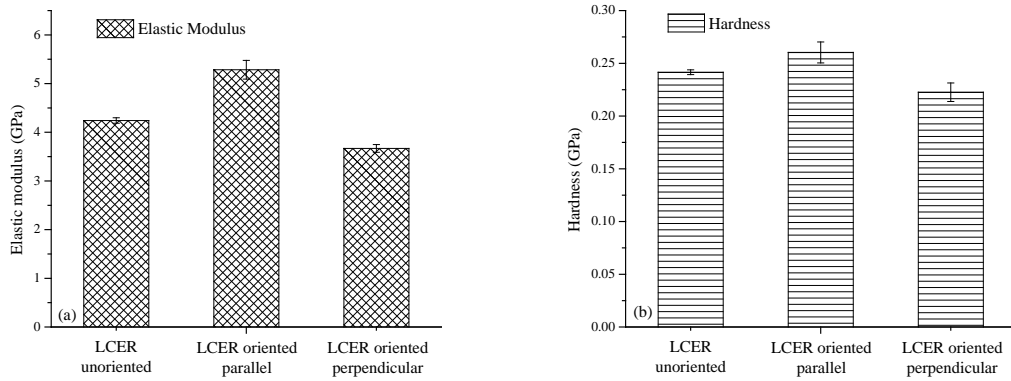


**Figure 5.10** Effect of LC orientation on (a) modulus and (b) hardness of the LCERs.

**Table 5.1** Mechanical properties of the LCERs determined by nanoindentation experiments.

	Maximum displacement (nm)	Contact stiffness ( $\mu\text{N}/\text{nm}$ )	Elastic modulus (GPa)	Hardness (GPa)	Average creep displacement ( $\mu\text{m}$ )
Unoriented LCER	1355.4 $\pm$ 7.3	34.3 $\pm$ 0.3	4.242 $\pm$ 0.064	0.242 $\pm$ 0.002	93.33 $\pm$ 1.14
Oriented LCER, longitudinal direction	1273.1 $\pm$ 22.9	41.1 $\pm$ 1.3	5.284 $\pm$ 0.192	0.260 $\pm$ 0.009	88.66 $\pm$ 6.98
Oriented LCER, transverse direction	1433.9 $\pm$ 23.6	30.9 $\pm$ 0.7	3.669 $\pm$ 0.079	0.223 $\pm$ 0.009	115.10 $\pm$ 6.08

The effect of LC orientation on the viscoelastic properties of LCERs was investigated by studying their creep behavior. The resins were deformed under a constant load of 9.5 mN for 60 s after the initial loading. The creep displacements of the samples are shown in **Figure 5.11**. Similar to the results for modulus and hardness, anisotropic creep behavior was observed for the LCERs after orientation. A decrease of 5% in creep displacement in the longitudinal direction and an increase of 23% in the transverse

direction compared to the LCER with random orientation was observed. In previous investigation, the creep performance of this LCER was studied and compared with the same resin cured into an amorphous phase. The resin showed an improvement in creep resistance after incorporating the LC domains, even when they were randomly oriented. As shown in **Figure 5.11**, this resistance can be further improved through magnetic processing.

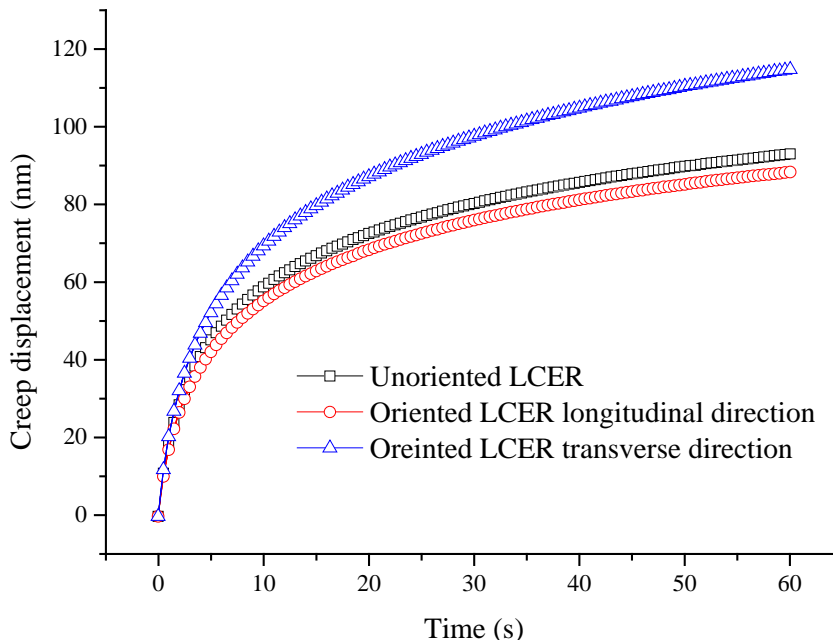


**Figure 5.11** Effect of LC orientation on creep behavior of the LCERs.

The magnetic orientation also significantly affected the thermomechanical properties of the resins. The CTE values of the LCERs were measured using TMA and the results are shown in **Figure 5.12** and **Table 5.2**. In the glassy region (60 - 80 °C), the oriented LCER exhibited a CTE value of 12.11  $\mu\text{m}/^\circ\text{C}$  in the longitudinal direction and a CTE value of 92.74  $\mu\text{m}/^\circ\text{C}$  in the transverse direction. This effect was also attributed to the structure and orientation of the LC domains. In the direction of orientation, the thermal expansion was highly restricted by the rigid, covalently bonded LC mesogens, whereas in the transverse direction, the van der Waals forces were less effective in holding the mesogens together. Interestingly, in the rubbery region (220 - 240 °C), a negative CTE value was observed for the oriented LCER in the longitudinal direction. Similar behavior was observed for highly oriented fibers, such as Kevlar, which also showed strong covalent bonding in the longitudinal direction and weak bonding through van der Waals forces in the transverse direction.

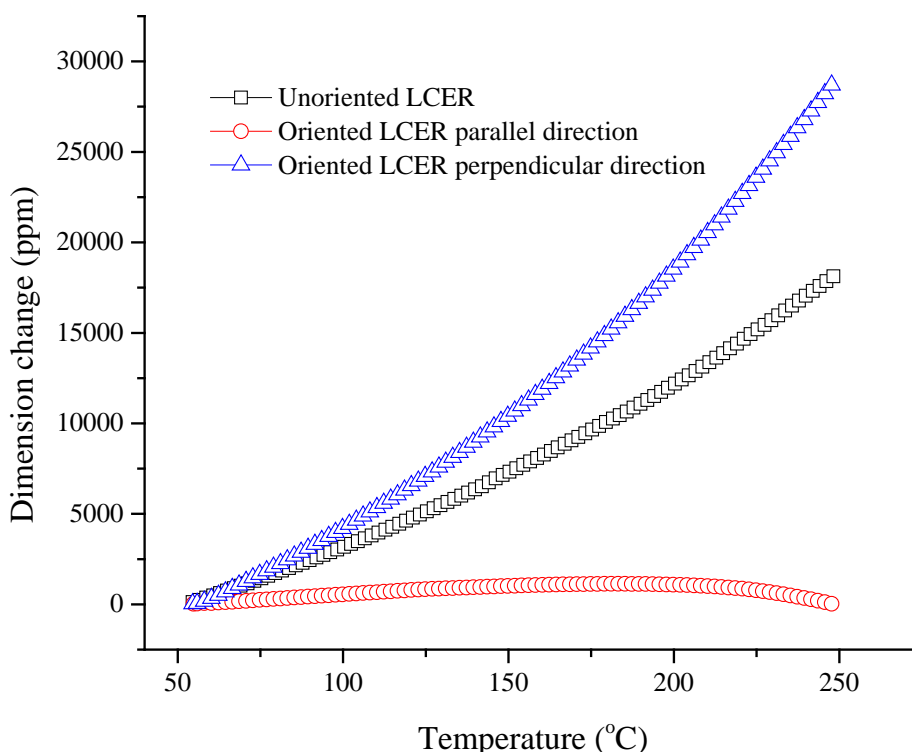


**Figure 5.12** Effect of LC orientation on thermal expansion of the LCERs.

**Table 5.2** CTE values of the LCERs determined by thermomechanical analysis.

	Glassy region CTE ( $\mu\text{m}/^\circ\text{C}$ )	Rubber region CTE ( $\mu\text{m}/^\circ\text{C}$ )
Unoriented LCER	66.75	126.9
Oriented LCER, longitudinal direction	12.11	-27.44
Oriented LCER, transverse direction	92.74	217.7

Dynamic mechanical properties of the LCERs cured with and without a magnetic field were investigated using DMA. The results are shown in **Figure 5.13**. Oriented LCERs exhibit higher values of glassy storage modulus, rubbery storage modulus, and glass transition temperature. For the oriented LCERs, in the direction parallel to the orientation, the applied force largely acts on the rigid LC domains, while in the direction perpendicular to the orientation the force is mostly applied to the relatively soft crosslinks between LC mesogens. Therefore, in the orientation direction, oriented LCERs show significantly higher values of storage modulus and loss modulus. In addition, compared to unoriented LCER, oriented LCER exhibits lower  $\tan \delta$  characteristic in the rigid direction of orientation. Moreover, the  $T_g$  was determined from the peak of the mechanical damping curve ( $\tan \delta$ ). Oriented LCERs have a higher  $T_g$ , possibly due to the decrease in free volume during the magnetic field processing.

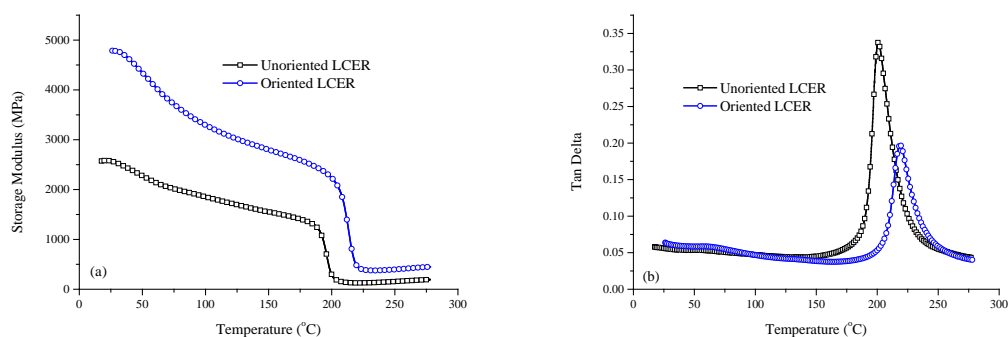


**Figure 5.13** Dynamic mechanical properties of oriented and unoriented LCERs. (a) Oriented LCER; (b) Unoriented LCER.

The thermal stability of the LCERs cured with and without a magnetic field was also examined. The thermal decomposition temperature was defined as the temperature when the samples lost 5% of their initial weight. The results show that the orientation of the LC domains does not have an influence on the thermal stability of the LCERs, which indicates that the major factor that affects thermal stability of the resins is chemical bonding rather than morphologies and orientation. All the thermomechanical properties of the oriented and unoriented LCERs are summarized in **Table 5.3**.

**Table 5.3** Thermal and dynamic mechanical data obtained from DMA and TGA.

	Oriented LCERs	Unoriented LCERs
E' at 30°C (MPa)	4774.9	2532.1
E' at 280°C (MPa)	396.8	155.2
T <sub>g</sub> DMA (°C)	219.0	201.0
T <sub>d</sub> (°C) at 95% weight	305.2	307.2

## 5.4 Conclusions

The curing behavior of the LCERs is studied using various experimental techniques. DSC and rheological results show that the formation of the LC phase leads to a decrease in viscosity of the system, resulting in a rate acceleration the curing reaction between BP with SAA. The synthesized LCERs were successfully oriented under a high strength magnetic field, and the effects of orientation on the thermomechanical properties of the LCERs were investigated. XRD results showed that the LC domains were successfully oriented along the magnetic field direction. An order parameter of 0.32 was achieved. The effect of orientation on mechanical properties of the LCERs was studied using nanoindentation. Compared to unoriented LCERs, oriented samples showed anisotropic mechanical behavior with improved modulus, hardness, stiffness, and creep resistance in the longitudinal direction. The alignment of the LC domains also resulted in an epoxy network with anisotropic thermal expansion.

## **Chapter 6: Synthesis and Characterization of Lightly Crosslinked Liquid Crystalline Epoxy Resins with Tunable Shape Memory Behavior**

### **6.1 Introduction**

Shape memory polymers (SMP) are a category of smart materials that are able to return to their original shape from a deformed state when exposed to external stimuli. SMPs generally consist of crosslinked polymer networks, which determine the permanent shape of the material, and switching segments, which can be oriented and solidified to fix a temporary shape<sup>94-95</sup>. The shape recovery is driven by the entropic force of the switching domains which tend to gain entropy and return to a random conformation when undergoing phase transitions, such as glass transition, liquid crystalline (LC) transition, and melting transition. Liquid crystalline elastomers (LCE) represent a special class of SMPs that are defined by a reversible LC phase transition and a unique coupling between LC mesogens and polymer networks<sup>96-99</sup>. They exhibit reversible shape change when exposed to external stimuli, such as heat<sup>96, 100-105</sup>, light<sup>106-112</sup>, or magnetic field<sup>113-114</sup>, which makes them excellent candidates for artificial muscles, sensors, lithography substrates, and shape memory materials. A number of LCEs with different LC phases and network structures have been synthesized and characterized, including nematic main-chain, smectic main-chain, nematic side-chain, and smectic side-chain LCEs. These materials exhibit a wide variety of shape memory and actuating behaviors. However, in spite of their promising properties and remarkable potential, practical applications of LCEs are limited because of the difficulties encountered when tailoring thermal transition temperatures and thermomechanical properties of the materials for end-use applications. In the work reported herein, a smectic main-chain LCE was produced by polymerizing a biphenyl-based epoxy monomer with an aliphatic carboxylic acid curing agent. By adjusting the stoichiometric ratio between the monomer and the curing agent, it was possible to control liquid crystallinity, crosslinking density, and network rigidity of the LCEs, thereby providing an easy way to tailor the LC transition and thermomechanical properties of the material. The prepared LCEs exhibited significant differences in phase transition temperature, stress-strain, shape memory, and thermal degradation behavior, as well as in dynamic mechanical, thermomechanical properties that were attributed to the tailored microstructure.

### **6.2 Methodology**

#### **6.2.1 Materials**

Epichlorohydrin and 4,4'-dihydroxybiphenyl were obtained from Acros Organics (Belgium). Sebacic acid (SA), 1,5,7-triazabicyclo[4.4.0]dec-5-ene, and benzyltrimethylammonium bromide, were purchased from Sigma-Aldrich (Milwaukee, WI). Sodium hydroxide, isopropyl alcohol, chloroform, methanol, and acetone were supplied by Fisher Scientific (Fair Lawn, NJ). All chemicals were used as received without further purification. The epoxy monomer, 4,4'-diglycidyl ether biphenyl (BP), was synthesized according to a reported procedure.

#### **6.2.2 LCE preparation**

The epoxy monomer was placed in a beaker which was heated in an oil bath. After the monomer was completely melted, curing agent and catalyst were introduced, followed by vigorous stirring for approx. 1 min. The mixture was poured into a PTFE mold and cured in a convection oven at 170 °C for 6 h. The molar ratio of BP to SA was adjusted to prepare LCEs with different microstructures. Three ratios (0.5, 0.7, and 1.0) were used and the resulting LCEs were referred to as BP-SA-05, BP-SA-07, and BP-SA-10, respectively.

### 6.2.3 Characterization

The thermal properties of the LCEs were determined using a differential scanning calorimeter (Discovery DSC, TA Instruments) under a nitrogen purge of 20 ml/min. A heat-cool-heat cycle with a ramp rate of 20 °C/min was used. The glass transition temperature ( $T_g$ ) and LC-isotropic transition temperature ( $T_{lc}$ ) were determined from the second heating scan.

The dynamic mechanical properties of the LCEs were investigated using a strain-controlled rheometer (ARES G2, TA Instruments) in DMA mode with a linear film tension geometry. The LCE samples were tested in a temperature range from -50 °C to 170 °C at a heating rate of 3 °C/min, a strain of 0.065% and an oscillation frequency of 1 Hz.

Two-dimensional X-ray scattering measurements were carried out using an Anton Paar SAXSess mc<sup>2</sup>. The scattering beam was recorded on an imaging plate (Multi-sensitive Storage Phosphor) and read using an imaging plate reader. The X-rays were generated at 40 kV/50 mA and the wavelength of the used X-ray beam was  $\lambda = 1.541 \text{ \AA}$  (Cu radiation). The structure of both unaligned and aligned LCEs was examined using both small angle X-ray scattering (SAXS) and wide angle X-ray scattering (WAXS) configuration. Aligned LCE samples with strain values of 100 % and 200 % respectively were prepared by mechanical stretching using the ARES G2 rheometer in tension mode. Because of their different transition temperatures, the stretching was performed at 40 °C, 65 °C, and 75 °C for BP-SA-05, BP-SA-07, and BP-SA-10, respectively. The samples were stretched under a constant strain rate of 0.0033/s until the desired strain value was achieved. Then the temperature was decreased to 25 °C at 1 °C/min.

Fracture surfaces of the LCEs were examined using a scanning electron microscope (FEI Quanta 200F FE-SEM) to investigate the effect of liquid crystallinity on the fracture morphology. The LCE samples were immersed in liquid nitrogen for 5 min and then fractured in a three-point bending fixture. The fracture surfaces were sputter-coated with a thin layer of Au, and SEM images were collected at 20 kV accelerating voltage.

Static tensile tests were carried out using a stress-controlled dynamic mechanical analyzer (Q800 DMA, TA Instruments) in a film tension geometry. The samples were uniaxially stretched at a temperature between  $T_g$  and  $T_{lc}$  at a stress ramp rate of 0.2 MPa/min to study the polydomain-monodomain transition of the LCEs. Because of the LCEs' different transition temperatures, the tests were performed at 40 °C, 65 °C, and 75 °C for BP-SA-05, BP-SA-07, and BP-SA-10, respectively.

Cyclic thermomechanical tensile tests were carried out using a Q800 DMA in a controlled force mode. The strain of the LCEs was measured over a temperature range covering the LC phase transition (40 - 80 °C for BP-SA-05, 65 - 125 °C for BP-SA-07, and 75 - 145 °C for BP-SA-10) and under a constant stress of 0.1 MPa. Taking BP-SA-05 as an example, the sample was heated to 80 °C, and then a constant uniaxial stress of 0.1 MPa was applied. The sample was equilibrated under these conditions for 10 min. Then the temperature was decreased to 40 °C at a cooling rate of 1 °C/min. The LC domains that formed upon cooling were immediately oriented under the constant stress, resulting in an extension of the LCE film. The temperature was then increased to 80 °C again at a heating rate of 1 °C/min to examine the contraction of the film caused by the transition from the LC phase to the isotropic phase. These steps were repeated for ten times on the same sample to study the repeatability of the shape memory properties.

Cyclic thermomechanical tensile tests were also performed at different stress levels to investigate the sensitivity of the LC networks to applied stresses. Six stress levels (0.01 MPa, 0.05 MPa, 0.1 MPa, 0.2 MPa, 0.3 MPa, and 0.4 MPa) were examined. Taking BP-SA-05 as an example, tests consisted of the following steps: (1) heating the sample to 80 °C, (2) applying a constant uniaxial stress of 0.01 MPa, (3) equilibrating the sample for 10 min, (4) decreasing the temperature to 40 °C at a cooling rate of 1 °C/min, and (5) increasing the temperature to 80 °C at a heating rate of 1 °C/min. This testing procedure was repeated using the other five stress levels on the same sample.

Cyclic thermomechanical compression tests were carried out using a thermomechanical analyzer (Q400EM TMA, TA Instruments). The samples were pressed with a force of 0.05 N and the dimensional change was measured as a function of temperature. The measurements were performed using a heat-cool-heat cycle with a temperature ramp rate of 3 °C/min. The coefficients of thermal expansion (CTE) of the LCEs in different temperature regions were investigated and correlated with the change of microstructure in the samples.

Iso-strain tests of the LCEs were performed using an ARES G2 rheometer in a strain-controlled DMA mode with a linear film tension geometry. Because of the different LCE transition temperatures, the tests were performed at 40 °C, 65 °C, and 75 °C for BP-SA-05, BP-SA-07, and BP-SA-10, respectively. The samples were stretched to a strain of 100% using a constant strain rate of 0.0033/s. Then the stress required to maintain the constant strain was measured as the temperature was increased to 150 °C at 1 °C/min.

The thermal stability of the LCEs was studied using a thermogravimetric analyzer (Discovery TGA, TA Instruments). The LCE sample was placed in a platinum pan and heated from 25 °C to 800 °C at a rate of 20 °C/min under a nitrogen purge of 10 mL/min.

## **6.3 Results and Discussion**

### **6.3.1 Thermal, liquid crystalline, and dynamic mechanical properties**

Three LCEs with different compositions were prepared from the reaction between



an epoxy monomer, 4,4'-diglycidyloxybiphenyl (BP), and a curing agent, sebacic acid (SA). Three molar ratios between BP and SA (0.5, 0.7, and 1.0) were used and the resulting LCEs were referred to as BP-SA-05, BP-SA-07, and BP-SA-10, respectively. The presence of crosslinked LC domains and their reversible phase transitions upon heating and cooling determine the shape memory behavior of LCEs. Therefore, thermal and LC properties of the synthesized LCEs were investigated using differential scanning calorimetry (DSC). **Figure 6.1(a)** shows that the three LCEs exhibited different glass transition temperature ( $T_g$ ) and liquid crystalline transition temperature ( $T_{lc}$ ), indicating that the formation of the LC domains and the structure of the crosslinking network were strongly affected by the chemistry between the monomer and the curing agent.

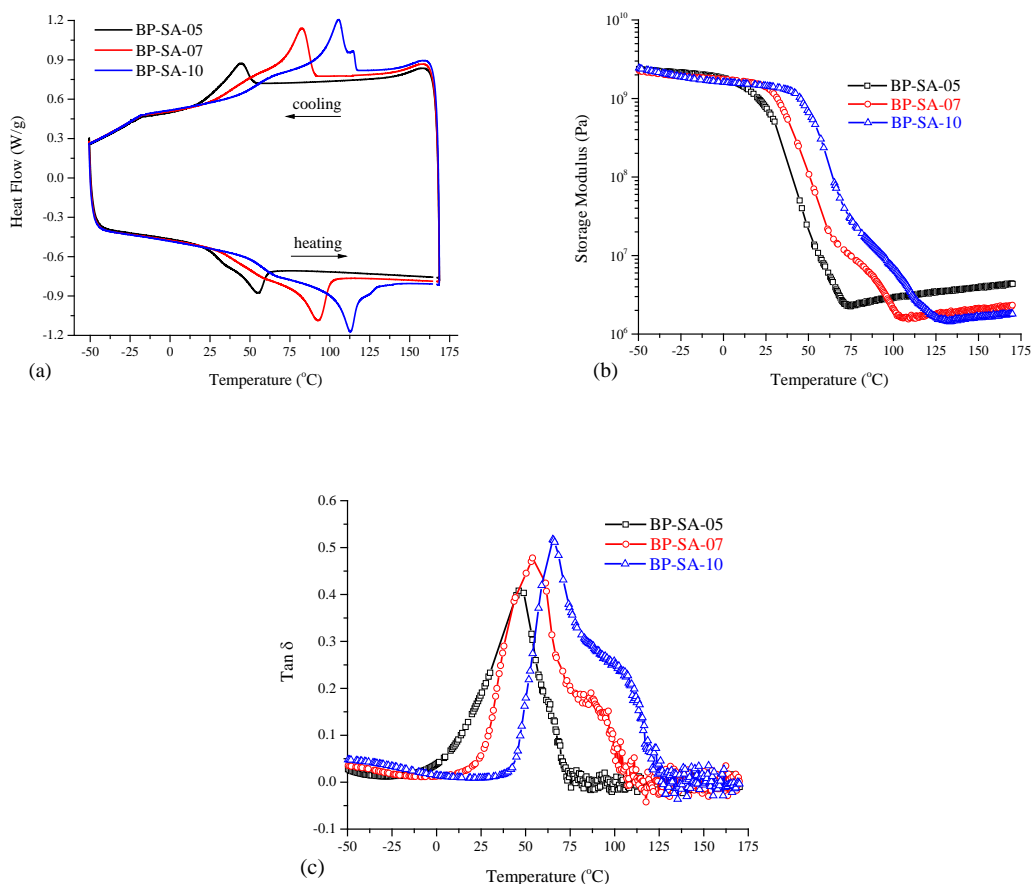


**Figure 6.1** Thermal properties, liquid crystalline behavior, and dynamic mechanical properties of LCEs with different compositions determined by DSC and DMA: (a) first cooling and second heating DSC scans, (b) storage modulus  $E'$ , and (c) dissipation factor  $\tan \delta$ .

The reaction between an epoxy and carboxylic acid is complicated, involving several parallel reactions as depicted in **Figure 6.2(a)**. The first step involves the ring-opening reaction of the epoxy by carboxylic acid, resulting in the formation of a linear oligomer with carboxylic acid groups on the end as further reaction sites. This step is

considered crucial for the LC phase formation because the aspect ratio of the BP mesogen alone is not high enough to exhibit LC behavior. The addition of SA increases the mobility of BP by introducing aliphatic chains onto the monomers, facilitating their self-organization into an ordered LC phase. The second step involves the crosslinking reaction through the hydroxyl groups formed in the previous step. They can react either with carboxylic acid through an esterification reaction or with epoxy through an etherification reaction. It was assumed that the chemical bond formation during this step was highly dependent on the stoichiometric ratio between BP and SA which greatly influenced the liquid crystallinity and network structure of the LCEs.

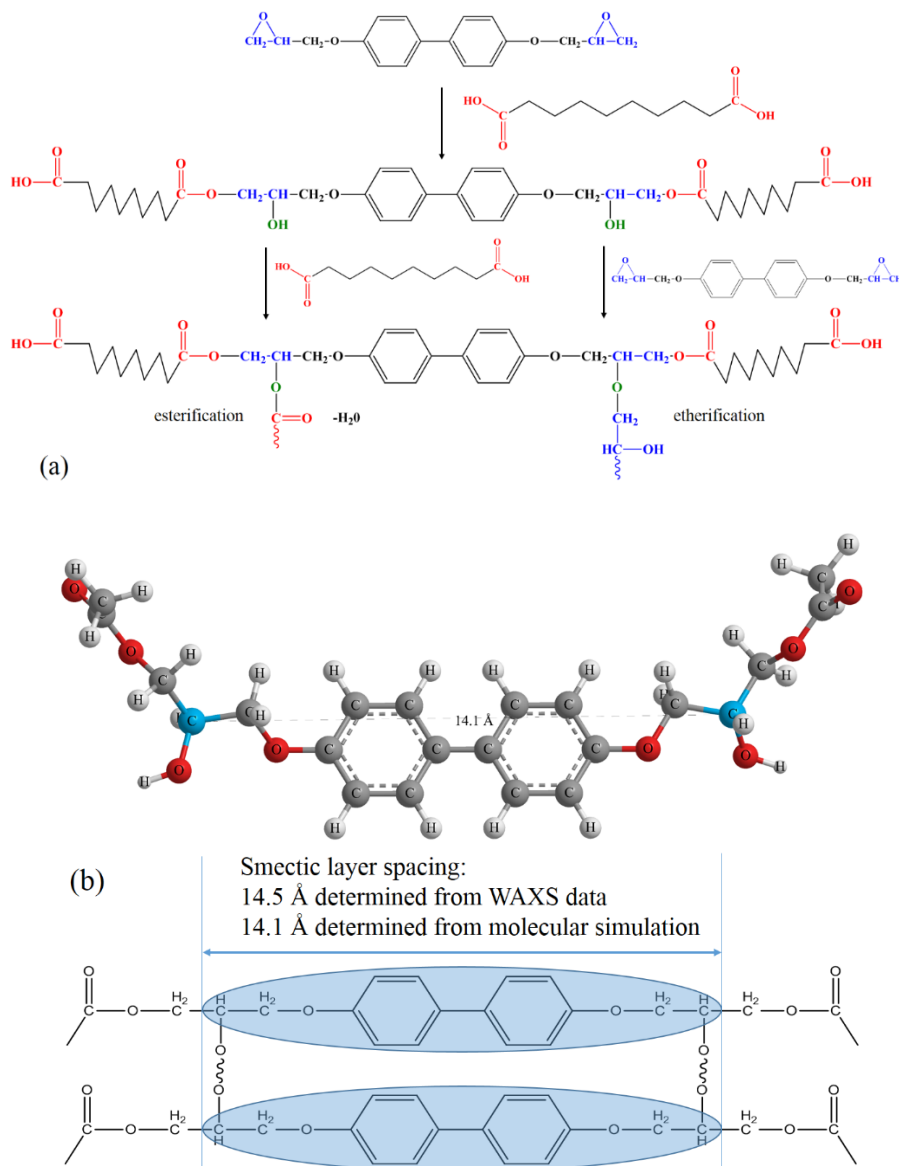


**Figure 6.2** (a) Possible chemical reactions between the epoxy monomer and the curing agent. (b) Molecular simulation of the mesogens and the LC phase formation.

**Table 6.1** Thermal properties, liquid crystalline behaviors, and dynamic mechanical properties of the LCEs determined by DSC and DMA.

LCE	$T_g^a)$ (°C)	$T_{lc}^b)$ (°C)	$\Delta H_{lc}$ (J/g)	$T_g^c)$ (°C)	$T_{lc}^d)$ (°C)	E' at -50 °C (GPa)	E' at 150 °C (MPa)
BP-SA-05	28.83	54.91	5.61	46.13	62.80	2.38	3.94
BP-SA-07	43.97	92.52	14.67	53.89	84.79	2.26	2.14
BP-SA-10	57.18	112.80	15.43	65.27	101.29	2.45	1.62

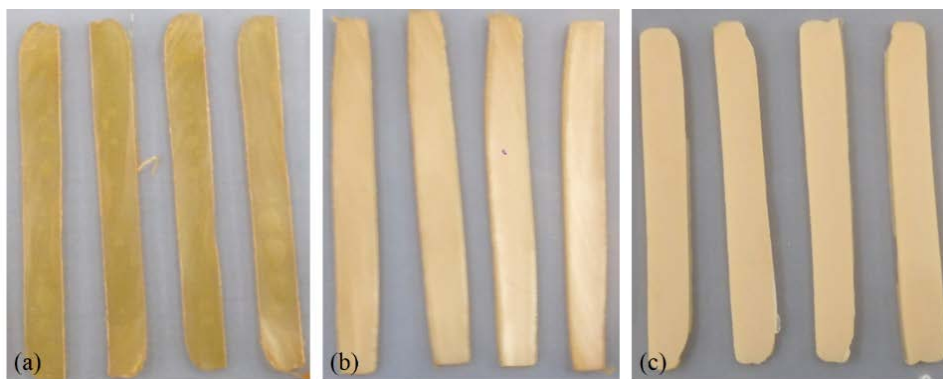
<sup>a)</sup> Measured from the midpoint of the step change in the second heating DSC scan.

<sup>b)</sup> Measured from the peak of the second heating DSC scan.

<sup>c)</sup> Measured from the first peak of the  $\tan \delta$  curve after peak deconvolution.

<sup>d)</sup> Measured from the second peak of the  $\tan \delta$  curve after peak deconvolution.

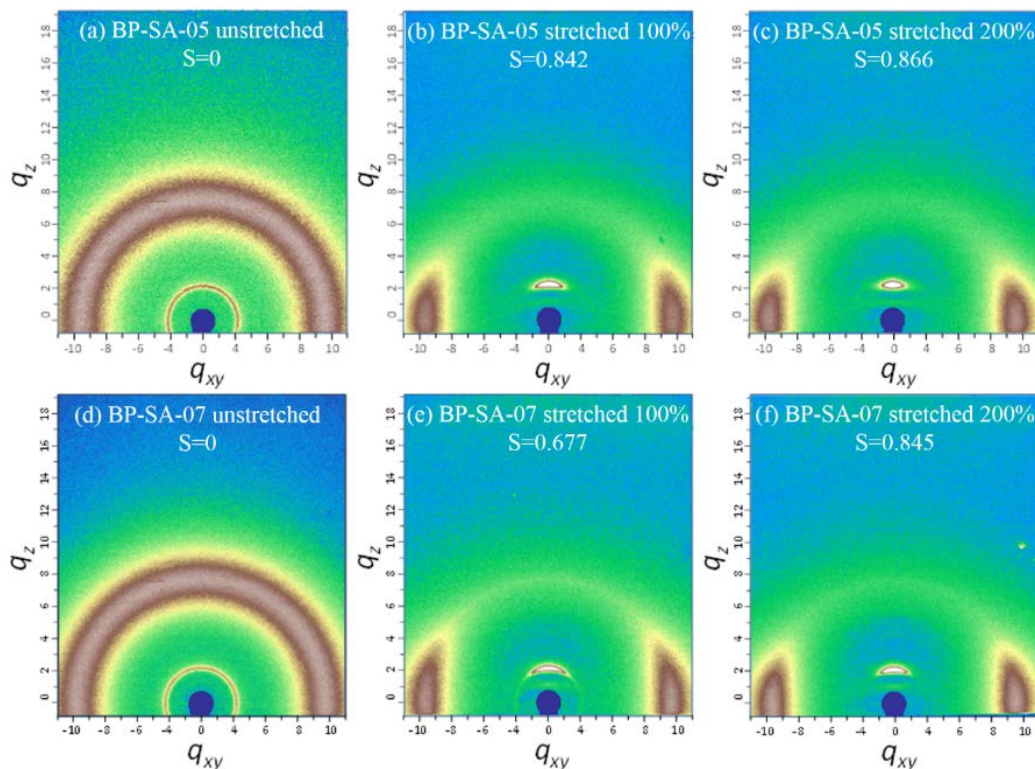
The values of  $T_g$ ,  $T_{lc}$ , and  $\Delta H_{lc}$  were determined by DSC and DMA and are listed in **Table 6.1**. The degree of liquid crystallinity (related to  $\Delta H_{lc}$ ) decreased with increasing amounts of SA, indicating that the formation of a LC phase was highly affected by the crosslinking reaction of the system. In the case of BP-SA-05, the hydroxyl groups formed in the first step immediately formed crosslinks because of the abundant supply of SA molecules, leading to highly branched oligomer chains that were difficult to be rearranged to form an LC phase. A visual comparison of the LCEs with different compositions is provided in **Figure 6.3**, in which BP-SA-07 and BP-SA-10 samples appeared more opaque because of their higher degrees of liquid crystallinity that causes light scattering. In contrast, BP-SA-05 appeared more transparent because of the limited number of LC domains in the network. Additionally, small air bubbles were observed on the bottom surface of sample BP-SA-05, suggesting a higher degree of esterification reactions between the hydroxyl groups and carboxylic acid. As can be seen in **Table 6.1**, the thermal stability of the LC phase ( $T_{lc}$ ) was also dependent on the stoichiometric ratio. For thermotropic LC polymers, the thermal stability of the LC phase was closely related to the morphology of the LC lamellae. LC domains with thinner lamellae generally exhibited lower melting temperatures. As the number of SA molecules increased, the integrity of the LC lamellae was adversely affected, leading to LC domains with loosely-packed mesogens that resulted in a lower transition temperature of the LC phase. The glass transition of the LCEs was also influenced by the stoichiometric ratio, as shown in **Table 6.1**. The LCEs showed a decrease in  $T_g$  as more SA molecules were incorporated into the system, indicating a softened network. Figure 1b and 1c show the storage modulus (E') and dissipation factor ( $\tan \delta$ ) of the LCEs as determined by DMA. Two thermal relaxations were observed from the E' and  $\tan \delta$  curves, corresponding to the glass and LC-isotropic transition of the LCEs, respectively. The dynamic mechanical data determined by DMA are also summarized in **Table 6.1**. Similar to the DSC results,  $T_g$  and  $T_{lc}$  of the LCEs decreased with increasing number of SA molecules. Of particular note is that BP-SA-05 exhibited the highest value of E' in the rubbery plateau region, indicating a higher crosslinking density resulted from the higher reaction content of hydroxyl groups. These differences in LC properties were expected to significantly influence the shape memory properties of the LCEs.



**Figure 6.3** Photos of the LCEs with different compositions: (a) BP-SA-05, (b) BP-SA-07, and (c) BP-SA-10. The difference in liquid crystallinity was reflected by the optical appearance of the LCEs.

### 6.3.2 Structure and morphology

To investigate the macro- and micro-structure of the LCEs, both SAXS and WAXS were used to explore the arrangement of the LC domains in the network and the molecular ordering inside a single LC domain. **Figure 6.4** shows the 2-dimensional X-ray scattering patterns of LCEs with different compositions and degree of orientation. The patterns were quantified through radial integration along the scattering vectors and the results are shown in **Figure 6.5**.



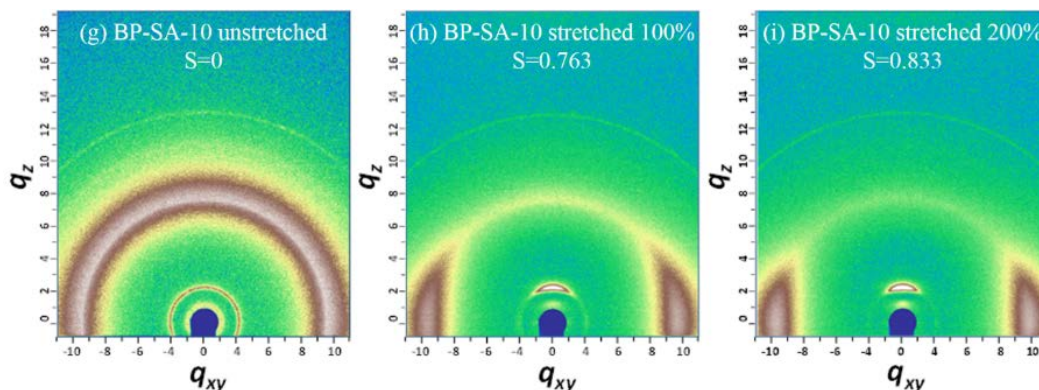


**Figure 6.4** SAXS/WAXS patterns of LCEs with different compositions and degree of orientation: (a-c) BP-SA-05, (d-f) BP-SA-07, and (g-i) BP-SA-10.

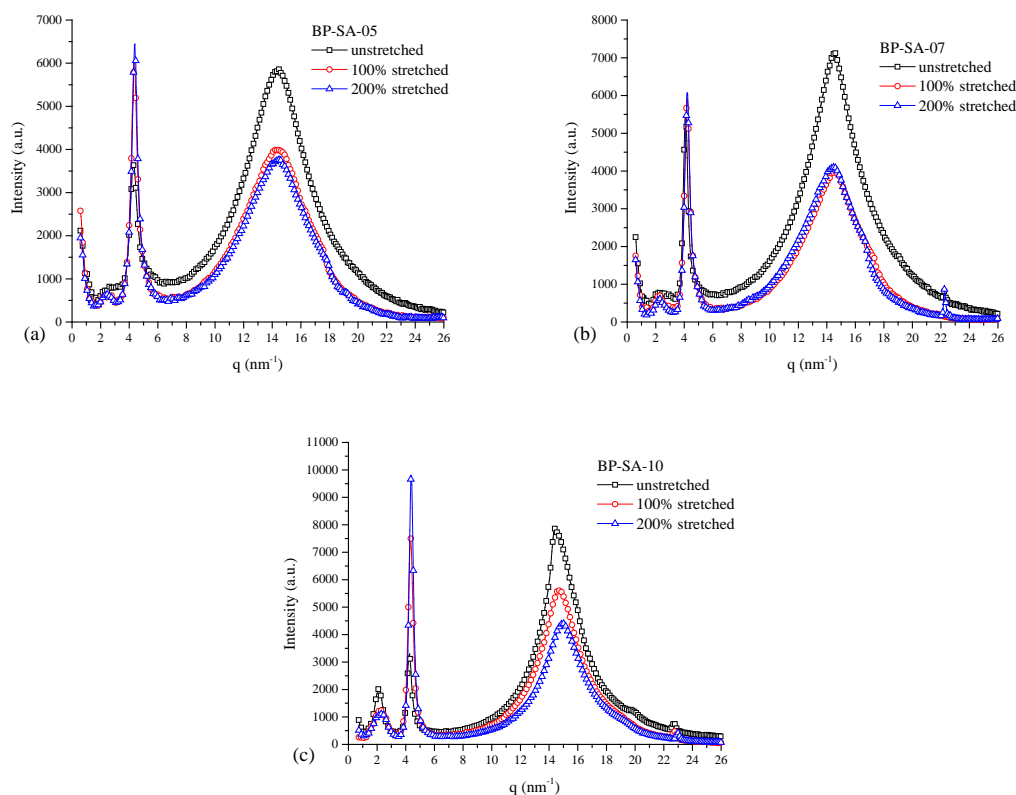


**Figure 6.5** Quantified SAXS/WAXS data of the LCEs with different composition: (a) BP-SA-05, (b) BP-SA-07, and (c) BP-SA-10.

**Figure 6.4(a), (d), and (g)** show that in the case of un-stretched LCEs, two major concentric rings indicated the presence of a smectic LC phase. The inner, sharp scattering ring ( $q = 4.3 \text{ nm}^{-1}$ ,  $d = 14.5 \text{ Å}$ ) was attributed to the periodic layers of the smectic LC structure with an average layer thickness of  $14.1 \text{ Å}$ . This value was compared to the value obtained by a molecular simulation of the mesogens performed using ChemBio 3D



software, shown in **Figure 6.2(b)**. The results from SAXS/WAXS and molecular simulation indicated that the thickness of the smectic layer was controlled by the branching/crosslinking points at which hydroxyl groups were formed. The outer, diffuse scattering ring ( $q = 14.8 \text{ nm}^{-1}$ ,  $d = 4.2 \text{ \AA}$ ) resulted from the scattering of neighboring mesogens in the smectic layers. It also can be seen in **Figure 6.4(a), (d), and (g)** that all LCEs exhibited very similar scattering patterns, indicating that the microstructure of the LC domains was not affected by their composition; rather composition affected their morphology such as domain size and number. For BP-SA-10, an additional scattering ring was observed near the beam stop ( $q = 2.2 \text{ nm}^{-1}$ ,  $d = 27.8 \text{ \AA}$ ). This additional ring was attributed to the stacking of separated LC domains into an ordered superstructure, which resulted from the high degree of liquid crystallinity of these LCEs, while such scattering was not observed for BP-SA-05 and BP-SA-07 because of their relatively lower degree of liquid crystallinity. In order to examine the morphology of the LC domains, the LCE samples were cryofractured and the fracture surfaces were examined using SEM. Fracture surfaces of LCEs with different compositions are shown in **Figure 6.6**. As the stoichiometric ratio increased, an increase in roughness of the fracture surfaces was observed. Considering the fact that LC domains deviate crack propagation and result in rough fracture surfaces, the SEM results indicated a higher number of LC domains in BP-SA-10. Similar results were also observed for densely crosslinked liquid crystalline epoxy resins, where rougher fracture surfaces were observed for resins cured into an LC phase compared to those cured into an amorphous phase.

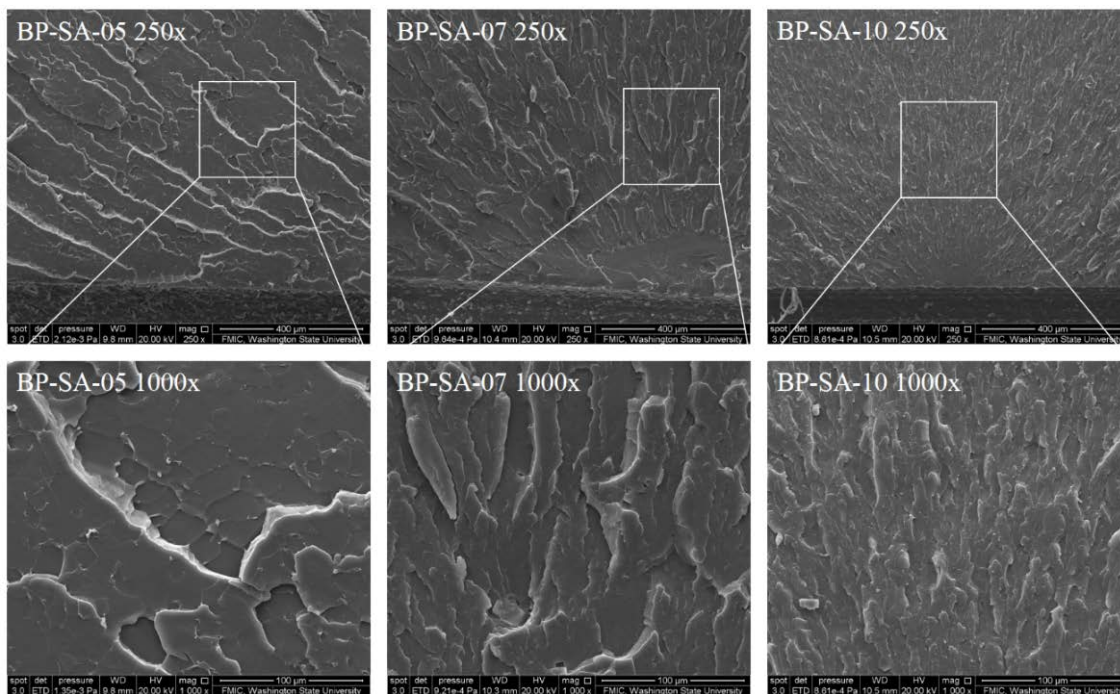


**Figure 6.6** Fracture surfaces of LCEs with different composition.

LCEs are known to exhibit large dimension change upon mechanical stretching because of the macroscopic orientation of the LC domains. In order to determine the correlation between the degree of orientation and mechanical deformation of the LCEs,

SAXS/WAXS experiments were performed on samples with different strain values and the scattering patterns are shown in **Figure 6.4**. Quantified scattering data are shown in **Figure 6.5**. The LC domains became highly oriented after mechanical stretching as indicated by the scattering arcs with non-uniform intensity distributions. In particular, the inner scattering ring turned into a pair of scattering arcs in the meridional direction, indicating that the LC molecules were aligned along the direction of the mechanical stretching and the incident X-rays were perpendicular to the layer normal of the smectic LC domains. A significant increase in scattering intensity resulting from the smectic layers was observed because of the macroscopically oriented LC domains (Figure 6.5). On the other hand, the laterally packed mesogens after orientation were indicated by a pair of scattering arcs in the equatorial direction. It is noteworthy that the position of the scattering peaks was not affected by mechanical stretching, indicating that the elongation of the LCE samples was caused by the rotation of the LC domains instead of their deformation. Stretching did change neither smectic layer thickness nor mesogen-spacing.

The degree of orientation was evaluated based on the azimuthal intensity distribution of scattering pattern resulted from the layered smectic ordering as shown in **Figure 6.7**. An order parameter  $S$  was calculated according to Herman's method:

$$\cos(\alpha) = \cos(\chi)\cos(\theta)$$

$$\langle \cos^2 \alpha \rangle = \frac{\int_0^{\pi/2} I(\alpha) \cdot \sin \alpha \cdot \cos^2 \alpha \cdot d\alpha}{\int_0^{\pi/2} I(\alpha) \cdot \sin \alpha \cdot d\alpha}$$

$$S = \frac{1}{2}(3\langle \cos^2 \alpha \rangle - 1)$$

where  $\alpha$  is the angle between the smectic layer normal and the direction of mechanical stretching,  $\chi$  is the azimuthal angle of the scattering ring, and  $\theta$  is the scattering angle.  $I(\alpha)$  is the intensity distribution of the sample; it can be directly calculated from the azimuthal intensity distribution  $I(\chi)$ . The calculated order parameters of LCEs with different compositions and degree of orientation are shown in **Figure 6.4** with their respective scattering patterns. Each LCE exhibited a significant increase in order parameter after mechanical stretching. Interestingly, a slight difference in the degree of orientation was observed for the stretched LCEs. In more detail, under a deformation of 100 %, BP-SA-05 reached a highly ordered state with an order parameter of 0.842, while BP-SA-07 and BP-SA-10 showed a relatively lower degree of orientation. After stretched to a deformation of 200 %, a relatively large increase in order parameter was observed for BP-SA-07 and BP-SA-10, compared to BP-SA-05. These indicated that degree of liquid crystallinity significantly influenced the degree of mechanical deformation of the LCEs as the elongation of the samples resulted from the rotation of the LC domains. Thus, LCEs with higher degrees of liquid crystallinity were expected to exhibit a higher degree of mechanical deformation.

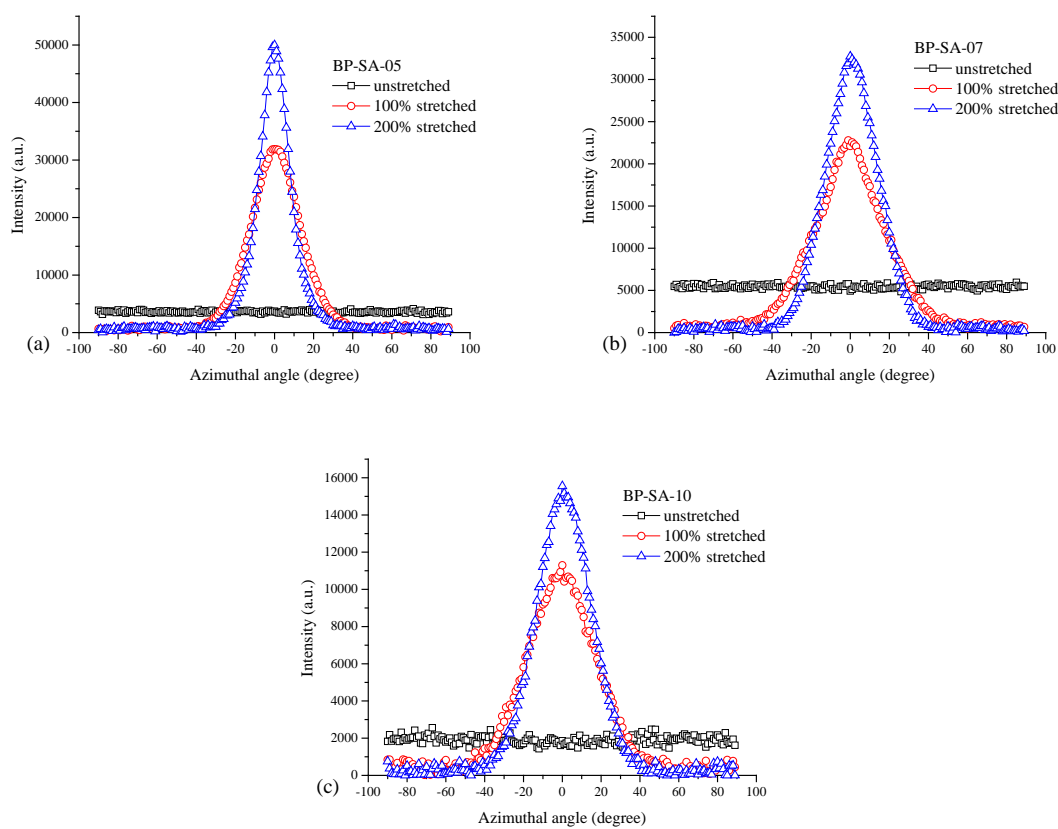


**Figure 6.7** Azimuthal intensity distribution of the scattering ring resulted from the smectic ordering. The scattering intensity resulted from the smectic layers increased dramatically after the mechanical stretching, indicating that the LC domains had been macroscopically aligned.

### 6.3.3 Thermomechanical properties

**Figure 6.8(a)** shows the static tensile behavior of LCEs with different compositions. The stress-strain curves of all LCEs exhibited a plateau region, indicating a polydomain-monodomain (P-M) transition of the LC phase. However, the difference in liquid crystallinity resulted in plateau regions with different widths for the three LCEs. In BP-SA-10, the high number of LC domains that were able to align caused a longer P-M transition. In addition, compared to the other two LCEs, BP-SA-10 required the highest critical stress to induce the P-M transition, which was attributed to the relatively rigid network created by the high content of biphenyl molecules. **Figure 6.9** shows the LCEs after static tensile testing. The relatively transparent central region of the LCE samples indicated the macroscopic orientation of the LC domains.



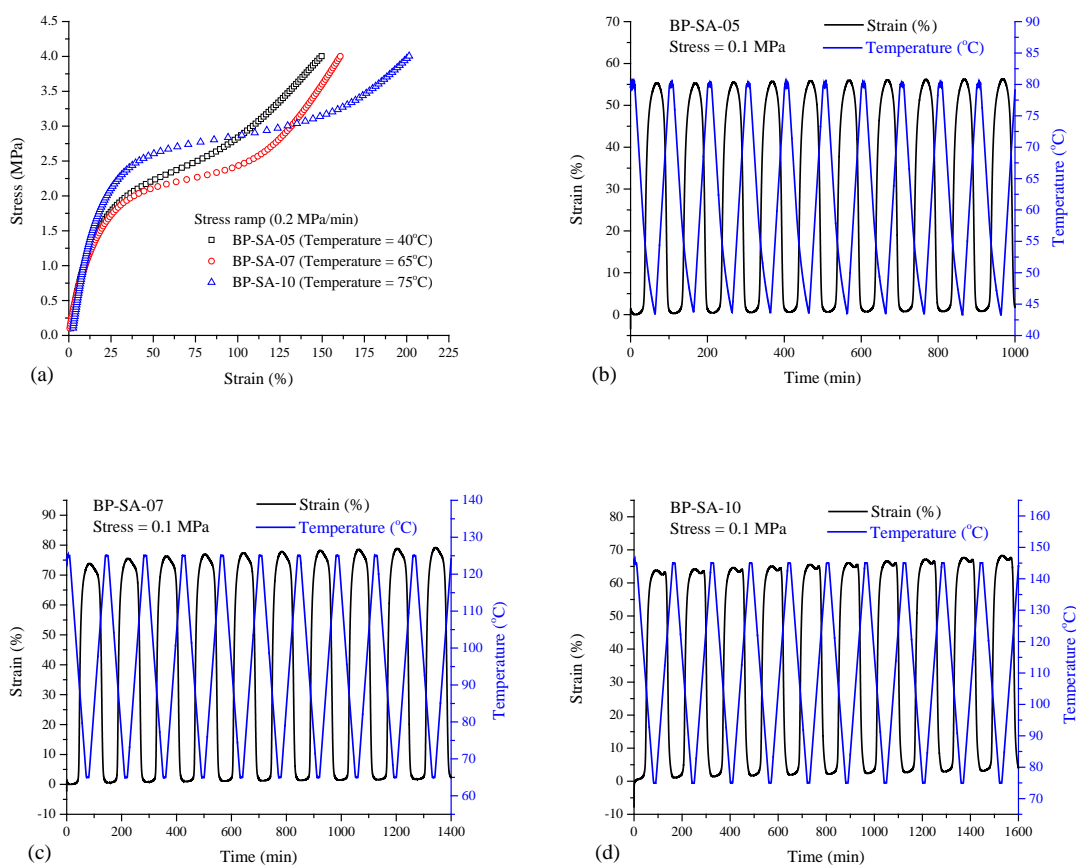


**Figure 6.8** Static tensile behavior and cyclic actuating behavior of LCEs with different compositions: (a) Stress-strain curves of the LCEs and (b-d) Cyclic thermomechanical tensile tests of the LCEs.



**Figure 6.9** Photos of the LCEs after the static tensile tests: (a) BP-SA-05, (b) BP-SA-07, and (c) BP-SA-10.

The investigated LCEs exhibited reversible shape change characteristics that were facilitated by the reversible phase transition of their LC domains. **Figure 6.10** illustrates triple shape memory behavior of the investigated LCEs. Cyclic thermomechanical tensile tests were employed to study the effects of liquid crystallinity, crosslinking density, and

network rigidity on the shape memory behavior of the LCEs. **Figure 6.8(b), (c) and (d)** show the thermally-induced actuating behavior of the LCEs under a constant stress of 0.1 MPa. The experiments were carried out at different temperature ranges that reflect the different  $T_{lc}$  of the LCEs. In general, the strain of the LCEs increased during the cooling process, indicating that the smectic LC domains formed upon cooling were immediately aligned. However, during the heating process, the strain decreased, indicating a contraction of the LCEs caused by the transition of the LC domains from the smectic phase to an isotropic phase. Interestingly, BP-SA-07 exhibited the highest strain value of 75 % under the applied stress, compared to 55 % and 65 % for BP-SA-05 and BP-SA-10, respectively. This was attributed to the combined effects of liquid crystallinity and crosslinking density. In the case of BP-SA-05, the liquid crystallinity was greatly reduced by the crosslinking reaction and therefore the LCE was not able to exhibit large dimensional change. In contrast, the high ratio of BP to SA resulted in a relatively rigid network in BP-SA-10, and the stress required to achieve the same strain value was increased. In the case of BP-SA-07, the network was less rigid while a sufficient degree of liquid crystallinity remained, and this resulted in higher strain values observed during cyclic thermomechanical tensile testing. However, it is worth mentioning that the shape memory effect is not only evaluated by the capability of reversible shape change, but also by the repeatability of the actuating behavior. **Figure 6.8** shows that although BP-SA-05 exhibited the smallest dimensional change, the repeatability of the actuating behavior was improved, which was attributed to the improved network integrity. The permanent deformation after 10 cycles was less than 1 % for BP-SA-05, whereas BP-SA-07 and BP-SA-10 showed a permanent deformation of 5 % and 4 %, respectively. Detailed strain values for the studied LCEs during each cycle are summarized in **Table 6.2**.

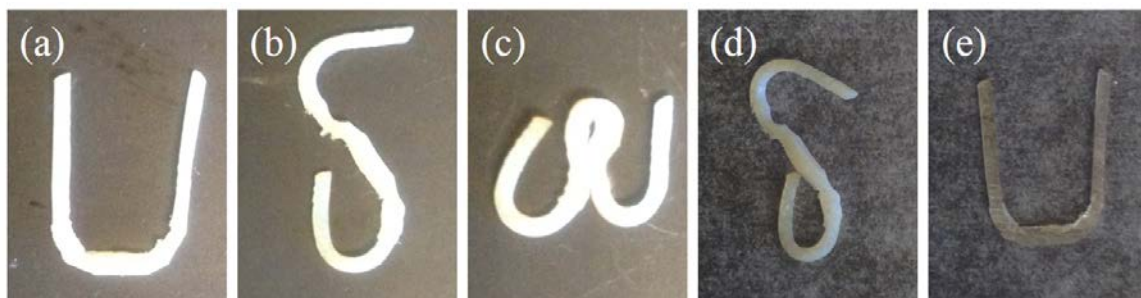


**Figure 6.10** A triple shape memory behavior of the LCEs: (a) Permanent shape, (b) deformed at 160 °C to temporary shape 1 and cooled to room temperature, (c) deformed at 85 °C to a secondary temporary shape 2 and cooled to room temperature, (d) heated to 85 °C to retrieve the temporary shape 1, and (e) heated to 160 °C to retrieve the permanent shape.

**Table 6.2** Actuating strains of the LCEs determined from the cyclic thermomechanical tensile tests.

LCE Cycle	BP-SA-05	BP-SA-07 Actuating Strain (%)	BP-SA-10
1	55.3	74.8	63.8
2	55.3	75.5	64.2
3	55.5	76.3	64.6
4	55.7	76.9	65.1
5	55.9	77.4	65.6
6	56.0	77.8	66.1
7	56.1	78.2	66.6
8	56.2	78.5	67.2
9	56.2	78.9	67.7
10	56.2	79.1	68.3

The stress sensitivity of the LCEs was expected to be different given their structural differences. Thus, the cyclic thermomechanical tensile tests were performed at several different stress levels and the results are shown in **Figure 6.11**. Again, BP-SA-05 exhibited the highest repeatability of the actuating behavior, even at the highest stress level (0.4 MPa), at which BP-SA-07 and BP-SA-10 exhibited large permanent deformations caused by the slippage of polymer chains. However, BP-SA-07 showed the highest sensitivity at lower stress levels (from 0.01 MPa to 0.1 MPa) caused by the balance between liquid crystallinity and network rigidity, as mentioned earlier. In the case of BP-SA-10, the LCE sample exhibited the largest dimensional change at higher stress levels (above 0.2 MPa) which was attributed to its high degree of liquid crystallinity. The change in shape of both BP-SA-05 and BP-SA-07 was limited by their relatively low number of LC domains that were able to undergo orientation. Detailed strain values for the studied LCEs at each stress level are summarized in **Table 6.3**.

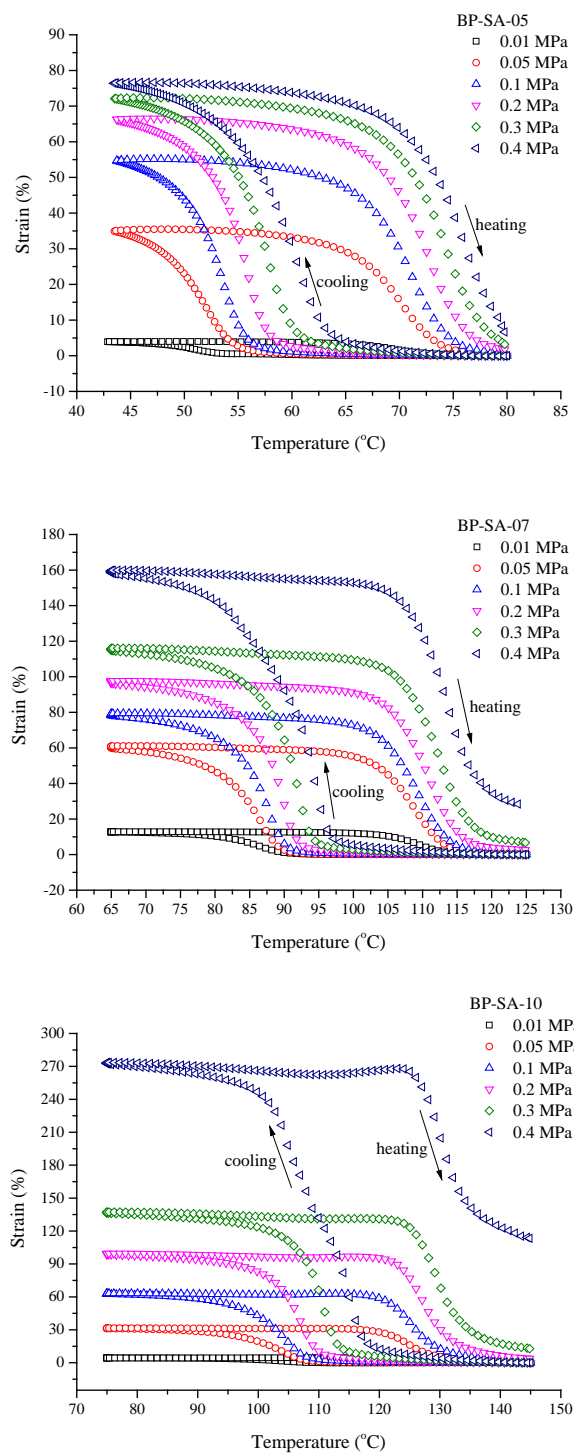
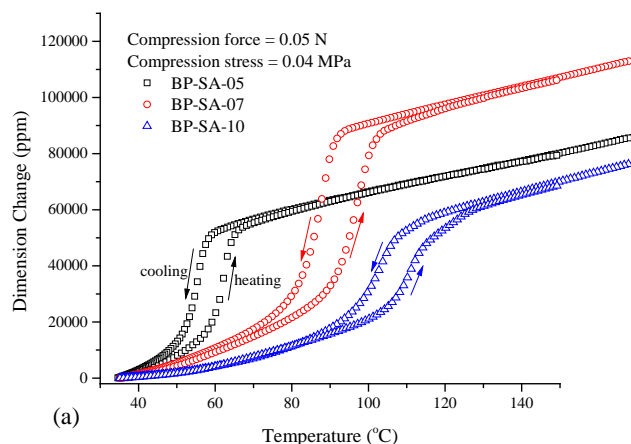


**Figure 6.11** Cyclic thermomechanical tensile tests of LCEs at different stress levels.

**Table 6.3** Actuating strains of the LCEs determined by cyclic thermomechanical tensile tests at different stress levels.

LCE Stress (MPa)	BP-SA-05	BP-SA-07	BP-SA-10
Actuating strain (%)			
0.01	3.9	12.8	4.3
0.05	34.9	60.9	31.3
0.1	54.8	78.7	63.2
0.2	66.3	96.9	99.5
0.3	72.1	115.2	137.2
0.4	76.4	159.8	273.6

**Figure 6.12(a)** shows the results of cyclic thermomechanical compression tests used to characterize the shape memory behavior of the LCEs. All LCEs exhibited a reversible shape change, although here the LC domains were not aligned in a specific direction, suggesting that the LC domains formed during the cooling process were able to adopt any conformation in response to the external force. During the heating process, entropic forces allowed the LC domains to return to random conformation. The higher sensitivity of BP-SA-07 to small stresses was further confirmed by the larger dimensional changes observed. The coefficient of thermal expansion (CTE) of the LCEs was determined by the second heating process of the cyclic thermomechanical compression test, and the results are shown in **Figure 6.12(b)**. The difference in CTE values provided additional information on the structural differences of the LCEs. For example, BP-SA-10 had the lowest CTE values in the glassy region (below 60 °C), indicating the relatively rigid characteristic of the material caused by the high ratio of rigid biphenyl molecules that resisted dimensional change. In the rubbery region (above 140 °C), however, BP-SA-05 exhibited the lowest CTE values because of the high crosslinking density that provided additional support to the network against thermal expansion.



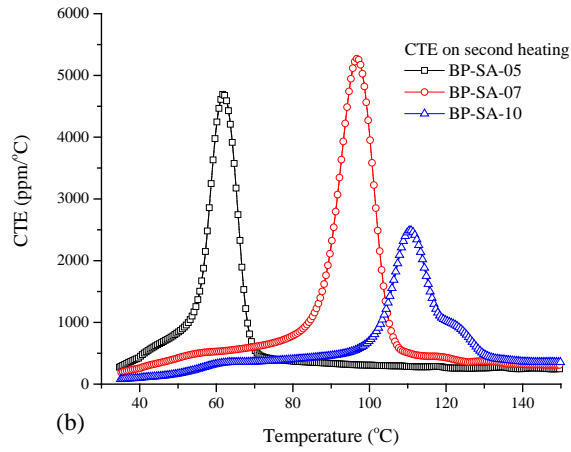


**Figure 6.12** (a) Cyclic thermomechanical compression tests of LCEs with different compositions. (b) Coefficient of thermal expansion of the LCEs determined from the second heating processing.

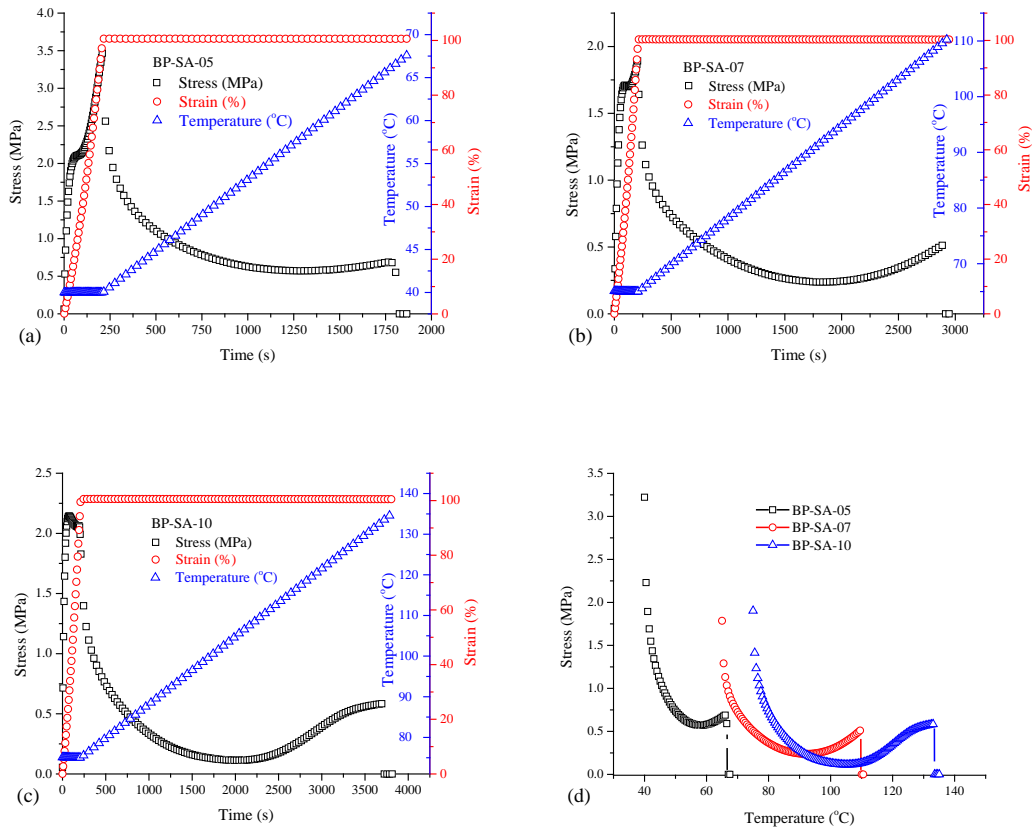


**Figure 6.13** Iso-strain tests of LCEs with different compositions: (a-c) original iso-strain tests and (d) comparison of the generated stress in the three LCEs.

Iso-strain tests were carried out to evaluate the retractive forces generated by the aligned LCEs when they are heated through the LC-isotropic phase transition. In this experiment, the LCE samples were stretched to a strain of 100 %, and then the stress required to maintain the constant strain was measured as a function of temperature, see **Figure 6.13(a), (b), and (c)**. **Figure 6.13(d)** compares the stress evolution of the LCEs during the heating process. Initially, a decrease in stress was observed, suggesting a relaxation of the crosslinking network. When the temperature approached the LC-isotropic phase transition temperature, the stress increased, an indication of the retractive force generated by the aligned LCEs. However, the LCEs did not show identical relaxation behavior, which was attributed to the differences in the degree of liquid crystallinity. In order to better understand the evolution of LCE microstructures during relaxation, detailed *in-situ* SAXS/WAXS experiments were performed, as shown in **Figure 6.14**. One end of the LCE sample was fixed on the sample stage and scattering patterns were collected at different relaxation temperatures. An increase in orientation was observed when the LCE was relaxed at temperatures below  $T_{lc}$ , which was attributed to the release of internal stresses in the crosslinking network. As mentioned earlier, mechanical stretching of the LCE samples caused a rotation of the LC domains and led to the elongation of the samples. Because the LC mesogens were directly incorporated into the backbone of the polymer chains, the rotation of the LC domains was expected to result in large deformation of the crosslinking network, which restricted the initial orientation of the LC domains to some extent and resulted in residual stress. With increasing temperature, the network softened relieving the residual stress and resulted in a perfection of the orientation. **Figure 6.14(b)** to **e** also show that the increase in regularity not only caused an increase in scattering intensity by the smectic layers, but also stronger scattering by the superstructure formed by the LC domains (the scattering arc near the beam stop). This indicated a cooperative motion of the LC domains during the thermal relaxation process because there was no external forces to further align them. When the temperature increased beyond  $T_{lc}$ , the LCE started losing its orientation as shown in **Figure 6.14(f), (g), and (h)**. Of particular interest is the fact that the disruption of the LC domains originated from the LC mesogens rather than the smectic layers. As can be seen in **Figure 6.14(f)**, the ordered smectic structure was still present even though the ordering between mesogens was lost. Once the temperature reached 155 °C, the LC ordering completely disappeared. However, after cooling to room temperature, the LCE exhibited a smectic LC phase again.

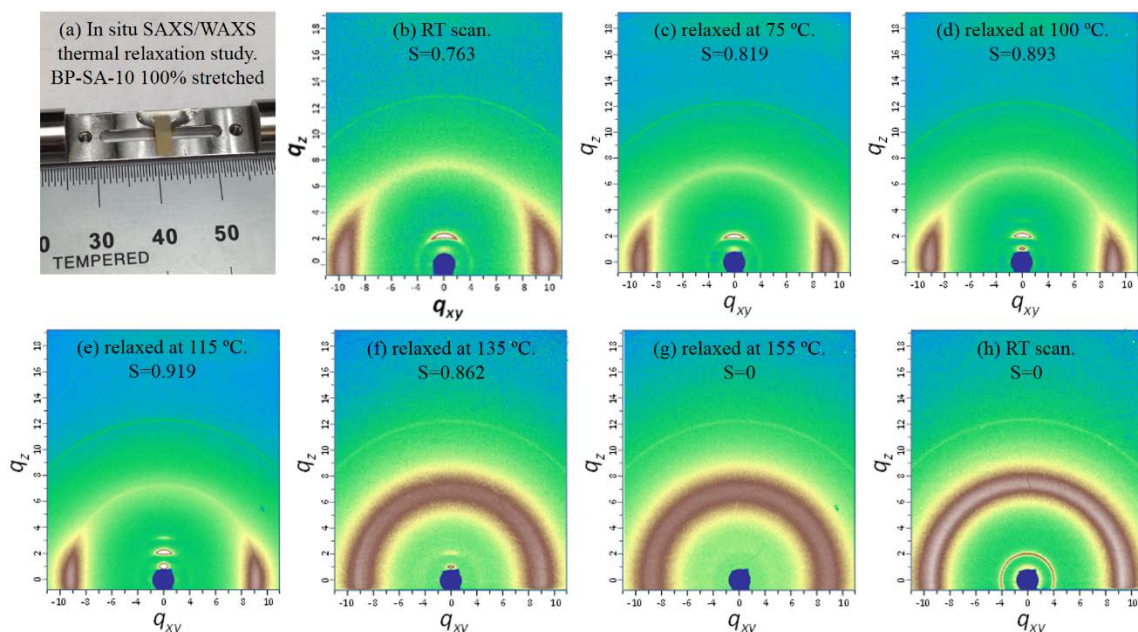


**Figure 6.14** *In-situ* SAXS/WAXS thermal relaxation study of a 100% stretched BP-SA-10: (a) Photo of LCE sample with one end fixed on the sample stage, (b-h) scattering patterns of LCE at different relaxation temperatures.

### 6.3.4 Thermal stability

The thermal stability of the LCEs was investigated to determine their structural differences; the results are shown in **Figure 6.15** and **Table 6.4**.  $T_1$ ,  $T_5$ , and  $T_{10}$  represent the temperatures at which a sample lost 1%, 5%, and 10% of its initial weight, respectively. BP-SA-10 exhibited better thermal stability in the low temperature region ( $<350$  °C), indicating that the disruption of the network was restricted by the relatively rigid LC domains. However, as the temperature further increased, crosslinking density played a more important role than morphology, which was reflected in the higher  $T_5$  and  $T_{10}$  observed for BP-SA-05. When comparing the residual weight percent of the LCEs, BP-SA-10 exhibited the highest values, indicating a high percentage of BP molecules, because during the thermal decomposition of polymers, char formation is generally promoted by aromatic structures.



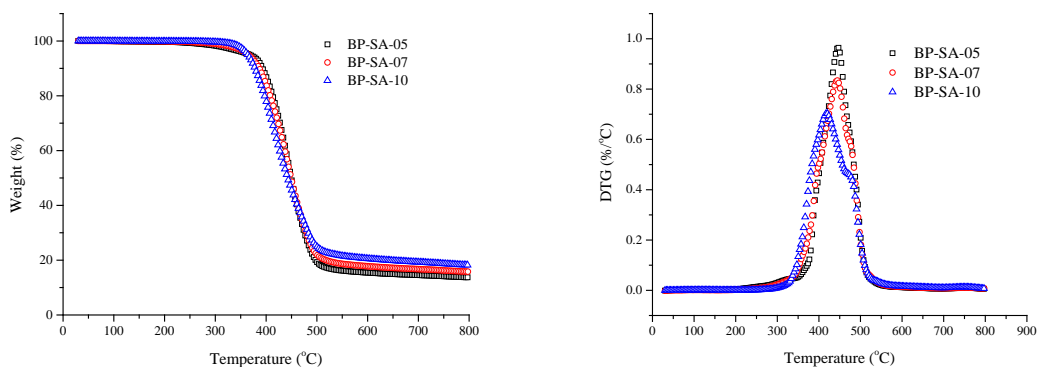


**Figure 6.15** Thermal degradation of LCEs with different compositions.

**Table 6.4** Thermal stability of the LCEs determined by TGA.

LCE	$T_1$ (°C)	$T_5$ (°C)	$T_{10}$ (°C)	Residual weight (%)
BP-SA-05	268.4	366.9	390.4	13.7
BP-SA-07	298.4	364.6	386.8	15.8
BP-SA-10	331.5	363.8	378.2	18.2

## 6.4 Conclusions

Smectic, main-chain LCEs were synthesized by polymerizing an epoxy monomer with a di-carboxylic curing agent. By changing the stoichiometric ratio of monomer to curing agent, LCEs with different degrees of liquid crystallinity, crosslinking density, and network rigidity were prepared. Because of these structural differences, the LCEs exhibited significant differences in thermomechanical properties and shape memory behavior. The thermal relaxation of aligned LCEs was studied in-depth to explore the evolution of the LCE microstructures during deformation. The result will contribute to the fundamental knowledge of LCEs in general and in the future will aid in the design and application of practical shape memory LCE systems.

## Chapter 7: Summary

This work discussed the development of zirconium tungstate ( $\text{ZrW}_2\text{O}_8$ ) nanoparticles with negative coefficient of thermal expansion (CTE) and liquid crystalline epoxy resins (LCERs) with different functionalities for advanced composites applications. The important results and conclusions of this work are highlighted below:

1. Nano-sized  $\text{ZrW}_2\text{O}_8$  particles were synthesized using a hydrothermal method. The effect of reaction conditions on morphology and crystallite size of the  $\text{ZrW}_2\text{O}_8$  nanoparticles was characterized through careful selection of initial reactants, acid types and concentration, reaction time, and temperature. Three types of  $\text{ZrW}_2\text{O}_8$  nanoparticles with distinct morphologies and crystallite size-scales were prepared and characterized to compare thermal and physical properties. Nano-sized  $\text{ZrW}_2\text{O}_8$  particles for two of the morphologies exhibited a negative CTE that is about 30% larger than the CTE of bulk  $\text{ZrW}_2\text{O}_8$  in the  $\alpha$ -phase (ca. -11.4 vs. -8.8 ppm/ $^{\circ}\text{C}$ ). It was also found that the morphology of the zirconium tungstate had a significant effect on the pore structure and level of hydration in the nanoparticles.
2. The synthesized  $\text{ZrW}_2\text{O}_8$  nanoparticles were used in an epoxy matrix to develop  $\text{ZrW}_2\text{O}_8$ /Epoxy nanocomposites. The effect of morphology and thermal expansivity of zirconium tungstate nanoparticles on the rheological, thermo-mechanical, dynamic-mechanical, and dielectric properties of the nanocomposites were investigated. Nanoparticles with a smaller particle size and larger surface area led to a more significant reduction in gel-time and glass transition temperature of the epoxy nanocomposites, while a higher initial viscosity and significant shear thinning behavior was found in pre-polymer suspensions containing  $\text{ZrW}_2\text{O}_8$  with larger particle sizes and aspect ratios. The thermo- and dynamic-mechanical properties of epoxy-based nanocomposites improved with increasing loadings of the three types of  $\text{ZrW}_2\text{O}_8$  nanoparticles. In addition, the introduced  $\text{ZrW}_2\text{O}_8$  nanoparticles did not negatively affect the dielectric constant or the breakdown strength of the epoxy resin, suggesting potential applications of  $\text{ZrW}_2\text{O}_8$ /Epoxy nanocomposites in the microelectronic insulation industry.
3. A biphenyl-based epoxy monomer of 4,4'-diglycidylbiphenyl (BP) was synthesized and cured with a tetra-functional amine, sulfanilamide (SAA), to produce novel LCERs. The thermal properties, liquid crystalline morphologies, and cure behavior of the monomer were studied. The effects of curing condition on the glass transition temperature, thermomechanical, and dynamic mechanical properties of the resins were investigated. The effects of liquid crystalline (LC) phase formation on cure kinetic and creep behavior of the resins were also studied. The results showed that BP was not a liquid crystalline epoxy monomer. However, the use of SAA resulted in the formation of a smectic LC phase. Compared to the resins cured into an amorphous network, the LCERs exhibited a polydomain structure with individual LC domain distributed in the resin matrix. Kinetic analysis showed that compared to the resins cured in amorphous phase, LCERs exhibited higher values of reaction enthalpy and a complex dependence of activation energy on the degree of cure. The formation of the LC phase resulted in a decrease in activation energy, leading to higher degree of reaction. Creep tests revealed that the introduction of an LC

phase into the resin network can reduce creep strain and creep strain rate of the material, especially at elevated temperatures. Parameters extracted from the simulation indicated that instantaneous elasticity, retardant elasticity, and permanent flow resistance of the resins were enhanced by the presence of the LC phase. A rigid filler effect and a crosslinking effect are proposed to explain the reinforcing mechanisms.

4. The properties of the synthesized LCERs were further tailored using a thermomagnetic processing method to induce molecular orientation. The orientation of the LCERs was confirmed and quantified using two-dimensional X-ray diffraction. The effect of molecular alignment on mechanical and thermomechanical properties of the LCERs was investigated using nanoindentation and thermomechanical analysis, respectively. The effect of orientation on fracture behavior was also examined. The results showed that macroscopic orientation of the LC domains was achieved, resulting in an epoxy network with anisotropic modulus, hardness, creep behavior, and thermal expansion. In the direction of orientation, the resin showed an increase of 24.6 % in elastic modulus and a decrease of 81.9 % in CTE.

5. A smectic main-chain liquid crystalline elastomer (LCE), with controlled shape memory behavior, was synthesized by polymerizing the synthesized epoxy monomer with an aliphatic carboxylic acid curing agent. Microstructures of the LCEs, including their liquid crystallinity and crosslinking density were modified by adjusting the stoichiometric ratio of the reactants to tailor the thermomechanical properties and shape memory behavior of the material. Thermal and liquid crystalline properties of the LCEs, characterized using differential scanning calorimetry and dynamic mechanical analysis, and structural analysis, performed using small-angle and wide-angle X-ray scattering, showed that liquid crystallinity, crosslinking density, and network rigidity are strongly affected by the stoichiometry of the curing reaction. With appropriate structural modifications it was possible to tune the thermal, dynamic mechanical, and thermomechanical properties, as well as the shape memory and thermal degradation behavior of LCEs.

## References

- (1)Badrinarayanan, P.; Rogalski, M.; Wu, H.; Wang, X.; Yu, W.; Kessler, M. R., Epoxy Composites Reinforced with Negative-Cte  $\text{ZrW}_2\text{O}_8$  Nanoparticles for Electrical Applications. *Macromolecular Materials and Engineering* **2013**, 298, 136-144.
- (2)Miller, W.; Smith, C. W.; Dooling, P.; Burgess, A. N.; Evans, K. E., Tailored Thermal Expansivity in Particulate Composites for Thermal Stress Management. *Physica Status Solidi B-Basic Solid State Physics* **2008**, 245, 552-556.
- (3)Chu, X. X.; Huang, R. J.; Yang, H. H.; Wu, Z. X.; Lu, J. F.; Zhou, Y. A.; Li, L. F., The Cryogenic Thermal Expansion and Mechanical Properties of Plasma Modified  $\text{ZrW}_2\text{O}_8$  Reinforced Epoxy. *Materials Science and Engineering A-Structural Materials Properties Microstructure and Processing* **2011**, 528, 3367-3374.
- (4)Chen, M. Y.; Chen, C. G., Zirconium Tungstate/Bismaleimide Composite. *Polymers for Advanced Technologies* **2012**, 23, 958-966.
- (5)Sullivan, L. M.; Lukehart, C. M., Zirconium Tungstate ( $\text{ZrW}_2\text{O}_8$ )/Polyimide Nanocomposites Exhibiting Reduced Coefficient of Thermal Expansion. *Chemistry of*

*Materials* **2005**, *17*, 2136-2141.

(6)Tani, J.; Kimura, H.; Hirota, K.; Kido, H., Thermal Expansion and Mechanical Properties of Phenolic Resin/ZrW<sub>2</sub>O<sub>8</sub> Composites. *Journal of Applied Polymer Science* **2007**, *106*, 3343-3347.

(7)Badrinarayanan, P.; Mac Murray, B.; Kessler, M. R., Zirconium Tungstate Reinforced Cyanate Ester Composites with Enhanced Dimensional Stability. *Journal of Materials Research* **2009**, *24*, 2235-2242.

(8)Badrinarayanan, P.; Kessler, M. R., Zirconium Tungstate/Cyanate Ester Nanocomposites with Tailored Thermal Expansivity. *Composites Science and Technology* **2011**, *71*, 1385-1391.

(9)Badrinarayanan, P.; Rogalski, M. K.; Kessler, M. R., Carbon Fiber-Reinforced Cyanate Ester/Nano- ZrW<sub>2</sub>O<sub>8</sub> Composites with Tailored Thermal Expansion. *ACS Applied Materials & Interfaces* **2012**, *4*, 510-517.

(10)Gennes, P. G. d.; Prost, J., *The Physics of Liquid Crystals*. Clarendon Press: **1995**.

(11)Barclay, G. G.; Ober, C. K., Liquid-Crystalline and Rigid-Rod Networks. *Progress in Polymer Science* **1993**, *18*, 899-945.

(12)Douglas, E. P., Liquid Crystalline Thermosets. In *Encyclopedia of Polymer Science and Technology*, John Wiley & Sons, Inc.: **2002**.

(13)Shiota, A.; Ober, C. K., Rigid Rod and Liquid Crystalline Thermosets. *Progress in Polymer Science* **1997**, *22*, 975-1000.

(14)Carfagna, C.; Amendola, E.; Giamberini, M., Liquid Crystalline Epoxy Based Thermosetting Polymers. *Progress in Polymer Science* **1997**, *22*, 1607-1647.

(15)Mallon, J. J.; Adams, P. M., Synthesis and Characterization of Novel Epoxy Monomers and Liquid-Crystal Thermosets. *Journal of Polymer Science Part A-Polymer Chemistry* **1993**, *31*, 2249-2260.

(16)Lee, J. Y.; Jang, J. S., Synthesis and Curing of Liquid Crystalline Epoxy Resin Based on Naphthalene Mesogen. *Journal of Polymer Science Part A-Polymer Chemistry* **1999**, *37*, 419-425.

(17)Shiota, A.; Ober, C. K., Synthesis and Curing of Novel Lc Twin Epoxy Monomers for Liquid Crystal Thermosets. *Journal of Polymer Science Part A-Polymer Chemistry* **1996**, *34*, 1291-1303.

(18)Broer, D. J.; Lub, J.; Mol, G. N., Synthesis and Photopolymerization of a Liquid-Crystalline Diepoxide. *Macromolecules* **1993**, *26*, 1244-1247.

(19)Cho, S. H.; Lee, J. Y.; Douglas, E. P.; Lee, J. Y., Synthesis and Thermal Properties of Liquid Crystalline Thermoset Containing Rigid-Rod Epoxy. *High Performance Polymers* **2006**, *18*, 83-99.

(20)Lee, J. Y.; Jang, J. S., The Effect of Mesogenic Length on the Curing Behavior and Properties of Liquid Crystalline Epoxy Resins. *Polymer* **2006**, *47*, 3036-3042.

(21)Lee, J. Y., The Effect of Substituent on the Anisotropic Orientation of Liquid Crystalline Epoxy Compounds. *Polymer Bulletin* **2006**, *57*, 983-988.

(22)Hong, S. M.; Hwang, S. S.; Lee, J. Y., The Effect of the Curing Agent Content on the Curing and Liquid-Crystalline Phase of Liquid-Crystalline Epoxy Resin. *Journal of Polymer Science Part B-Polymer Physics* **2001**, *39*, 374-379.

(23)Hikmet, R. A. M.; Lub, J.; Vanderbrink, P. M., Structure and Mobility within Anisotropic Networks Obtained by Photopolymerization of Liquid-Crystal Molecules. *Macromolecules* **1992**, *25*, 4194-4199.

- (24)Holter, D.; Frey, H.; Mulhaupt, R.; Klee, J. E., Liquid Crystalline Thermosets Based on Branched Bismethacrylates. *Macromolecules* **1996**, *29*, 7003-7011.
- (25)Mormann, W.; Kuckertz, C., Liquid Crystalline Cyanurate Thermosets through Cyclotrimerisation of Novel Triaromatic Dicyanates. *Macromolecular Chemistry and Physics* **1998**, *199*, 845-851.
- (26)Korner, H.; Shiota, A.; Ober, C. K., Mixtures of Liquid-Crystalline and Amorphous Dicyanates: Unusual Curing Behavior and Mechanical Properties. *Chemistry of Materials* **1997**, *9*, 1588-1597.
- (27)Mormann, W.; Zimmermann, J., Synthesis and Mesogenic Properties of Diaromatic Cyanates and Isocyanates-Monomers for Liquid-Crystalline Thermosets. *Liquid Crystals* **1995**, *19*, 227-233.
- (28)Hoyt, A. E.; Benicewicz, B. C., Rigid Rod Molecules as Liquid-Crystal Thermosets .1. Rigid Rod Amides. *Journal of Polymer Science Part A-Polymer Chemistry* **1990**, *28*, 3403-3415.
- (29)Hoyt, A. E.; Benicewicz, B. C., Rigid Rod Molecules as Liquid-Crystal Thermosets .2. Rigid Rod Esters. *Journal of Polymer Science Part A-Polymer Chemistry* **1990**, *28*, 3417-3427.
- (30)Shiota, A.; Ober, C. K., Analysis of Smectic Structure Formation in Liquid Crystalline Thermosets. *Polymer* **1997**, *38*, 5857-5867.
- (31)Lin, Q. H.; Yee, A. F.; Sue, H. J.; Earls, J. D.; Hefner, R. E., Evolution of Structure and Properties of a Liquid Crystalline Epoxy During Curing. *Journal of Polymer Science Part B-Polymer Physics* **1997**, *35*, 2363-2378.
- (32)Harada, M.; Ando, J.; Hattori, S.; Sakurai, S.; Sakamoto, N.; Yamasaki, T.; Masunaga, H.; Ochi, M., In-Situ Analysis of the Structural Formation Process of Liquid-Crystalline Epoxy Thermosets by Simultaneous Saxs/Waxs Measurements Using Synchrotron Radiation. *Polymer Journal* **2013**, *45*, 43-49.
- (33)Lin, Q. H.; Yee, A. F.; Earls, J. D.; Hefner, R. E.; Sue, H. J., Phase-Transformations of a Liquid-Crystalline Epoxy During Curing. *Polymer* **1994**, *35*, 2679-2682.
- (34)Rosu, D.; Mititelu, A.; Cascaval, C. N., Cure Kinetics of a Liquid-Crystalline Epoxy Resin Studied by Non-Isothermal Data. *Polymer Testing* **2004**, *23*, 209-215.
- (35)Vyazovkin, S.; Mititelu, A.; Sbirrazzuoli, N., Kinetics of Epoxy-Amine Curing Accompanied by the Formation of Liquid Crystalline Structure. *Macromolecular Rapid Communications* **2003**, *24*, 1060-1065.
- (36)Ortiz, C.; Ober, C. K.; Kramer, E. J., Stress Relaxation of a Main-Chain, Smectic, Polydomain Liquid Crystalline Elastomer. *Polymer* **1998**, *39*, 3713-3718.
- (37)Hsu, S. H.; Wu, M. C.; Chen, S.; Chuang, C. M.; Lin, S. H.; Su, W. F., Synthesis, Morphology and Physical Properties of Multi-Walled Carbon Nanotube/Biphenyl Liquid Crystalline Epoxy Composites. *Carbon* **2012**, *50*, 896-905.
- (38)Sue, H. J.; Earls, J. D.; Hefner, R. E.; Villarreal, M. I.; Garcia-Meitin, E. I.; Yang, P. C.; Cheatham, C. M.; Plummer, C. J. G., Morphology of Liquid Crystalline Epoxy Composite Matrices Based on the Diglycidyl Ether of 4,4 '-Dihydroxy-Alpha-Methylstilbene. *Polymer* **1998**, *39*, 4707-4714.
- (39)Punchaipetch, P.; D'Souza, N. A.; Brostow, W.; Smith, J. T., Mechanical Properties of Glass Fiber Composites with an Epoxy Resin Modified by a Liquid Crystalline Epoxy. *Polymer Composites* **2002**, *23*, 564-573.

- (40)Dingemans, T. J.; Iqbal, M., Liquid Crystal Thermoset Resins for High Temperature Composites and Adhesives. *Plastics Rubber and Composites* **2010**, *39*, 189-194.
- (41)Bae, J.; Jang, J.; Yoon, S. H., Cure Behavior of the Liquid-Crystalline Epoxy/Carbon Nanotube System and the Effect of Surface Treatment of Carbon Fillers on Cure Reaction. *Macromolecular Chemistry and Physics* **2002**, *203*, 2196-2204.
- (42)Carfagna, C.; Meo, G.; Nicolais, L.; Giamberini, M.; Priola, A.; Malucelli, G., Composites Based on Carbon Fibers and Liquid Crystalline Epoxy Resins, 2 - Dynamic-Mechanical Analysis and Fracture Toughness Behavior. *Macromolecular Chemistry and Physics* **2000**, *201*, 2639-2645.
- (43)Carfagna, C.; Acierno, D.; Di Palma, V.; Amendola, E.; Giamberini, M., Composites Based on Carbon Fibers and Liquid Crystalline Epoxy Resins, 1 - Monomer Synthesis and Matrix Curing. *Macromolecular Chemistry and Physics* **2000**, *201*, 2631-2638.
- (44)Hsu, S. H.; Chen, R. S.; Chang, Y. L.; Chen, M. H.; Cheng, K. C.; Su, W. F., Biphenyl Liquid Crystalline Epoxy Resin as a Low-Shrinkage Resin-Based Dental Restorative Nanocomposite. *Acta Biomaterialia* **2012**, *8*, 4151-4161.
- (45)Ochi, M.; Tsuyuno, N.; Sakaga, K.; Nakanishi, Y.; Murata, Y., Effect of Network Structure on Thermal and Mechanical-Properties of Biphenol-Type Epoxy-Resins Cured with Phenols. *Journal of Applied Polymer Science* **1995**, *56*, 1161-1167.
- (46)Iqbal, M.; Knijnenberg, A.; Poullis, H.; Dingemans, T. J., All-Aromatic Liquid Crystalline Thermosets as High Temperatures Adhesives. *International Journal of Adhesion and Adhesives* **2010**, *30*, 682-688.
- (47)Giamberini, M.; Amendola, E.; Carfagna, C., A Novel Approach to the Tailoring of Polymers for Advanced Composites and Optical Applications, Involving the Synthesis of Liquid Crystalline Epoxy Resins. *Polymer Engineering and Science* **1999**, *39*, 534-542.
- (48)Hong, S. M.; Hwang, S. S., Anisotropic Orientation of the Carbon Fiber/Liquid Crystalline Epoxy Resin Composites. *Composite Interfaces* **2006**, *13*, 145-157.
- (49)Evans, J. S. O.; Hu, Z.; Jorgensen, J. D.; Argyriou, D. N.; Short, S.; Sleight, A. W., Compressibility, Phase Transitions, and Oxygen Migration in Zirconium Tungstate,  $ZrW_2O_8$ . *Science* **1997**, *275*, 61-65.
- (50)Mary, T. A.; Evans, J. S. O.; Vogt, T.; Sleight, A. W., Negative Thermal Expansion from 0.3 to 1050 Kelvin in  $ZrW_2O_8$ . *Science* **1996**, *272*, 90-92.
- (51)Yang, X. B.; Xu, J.; Li, H. J.; Cheng, X. N.; Yan, X. H., In Situ Synthesis of  $ZrO_2/ZrW_2O_8$  Composites with near-Zero Thermal Expansion. *J. Am. Ceram. Soc.* **2007**, *90*, 1953-1955.
- (52)Holzer, H.; Dunand, D. C., Phase Transformation and Thermal Expansion of  $Cu/ZrW_2O_8$  Metal Matrix Composites. *Journal of Materials Research* **1999**, *14*, 780-789.
- (53)Yan, X.; Cheng, X.; Xu, G.; Wang, C.; Sun, S.; Riedel, R., Preparation and Thermal Properties of Zirconium Tungstate/Copper Composites. *Materialwissenschaft Und Werkstofftechnik* **2008**, *39*, 649-653.
- (54)Sun, L.; Sneller, A.; Kwon, P.,  $ZrW_2O_8$ -Containing Composites with near-Zero Coefficient of Thermal Expansion Fabricated by Various Methods: Comparison and Optimization. *Composites Science and Technology* **2008**, *68*, 3425-3430.
- (55)Broer, D. J.; Mol, G. N., Anisotropic Thermal-Expansion of Densely Cross-Linked Oriented Polymer Networks. *Polymer Engineering and Science* **1991**, *31*, 625-631.

- (56) Hikmet, R. A. M.; Broer, D. J., Dynamic Mechanical-Properties of Anisotropic Networks Formed by Liquid-Crystalline Acrylates. *Polymer* **1991**, *32*, 1627-1632.
- (57) Lee, J. Y.; Jang, J., Anisotropically Ordered Liquid Crystalline Epoxy Network on Carbon Fiber Surface. *Polymer Bulletin* **2007**, *59*, 261-267.
- (58) Evans, J. S. O.; David, W. I. F.; Sleight, A. W., Structural Investigation of the Negative-Thermal-Expansion Material ZrW<sub>2</sub>O<sub>8</sub>. *Acta Crystallogr. Sect. B-Struct. Sci.* **1999**, *55*, 333-340.
- (59) Lee, J. Y., Transverse Alignment of Liquid Crystalline Epoxy Resin on Carbon Fiber Surface. *Journal of Applied Polymer Science* **2006**, *102*, 684-689.
- (60) Barclay, G. G.; McNamee, S. G.; Ober, C. K.; Papathomas, K. I.; Wang, D. W., The Mechanical and Magnetic Alignment of Liquid-Crystalline Epoxy Thermosets. *Journal of Polymer Science Part A-Polymer Chemistry* **1992**, *30*, 1845-1853.
- (61) Korner, H.; Shiota, A.; Bunning, T. J.; Ober, C. K., Orientation-on-Demand Thin Films: Curing of Liquid Crystalline Networks in Ac Electric Fields. *Science* **1996**, *272*, 252-255.
- (62) Koerner, H.; Ober, C. K.; Ku, H., Probing Electric Field Response of Lc Thermosets Via Time-Resolved X-Ray and Dielectric Spectroscopy. *Polymer* **2011**, *52*, 2206-2213.
- (63) Shiota, A.; Ober, C. K., Orientation of Liquid Crystalline Epoxides under Ac Electric Fields. *Macromolecules* **1997**, *30*, 4278-4287.
- (64) Jahromi, S.; Mijs, W. J., Liquid-Crystalline Epoxide Thermosets. *Molecular Crystals and Liquid Crystals Science and Technology Section A-Molecular Crystals and Liquid Crystals* **1994**, *250*, 209-222.
- (65) Pottier, L.; Costa-Torro, F.; Tessier, M.; Davidson, P.; Fradet, A., Investigation of Anisotropic Epoxy-Amine Thermosets Synthesised in a Magnetic Field. *Liquid Crystals* **2008**, *35*, 913-924.
- (66) Jahromi, S., Liquid-Crystalline Epoxide Thermosets - a Deuterium Nuclear-Magnetic-Resonance Study. *Macromolecules* **1994**, *27*, 2804-2813.
- (67) Jahromi, S.; Kuipers, W. A. G.; Norder, B.; Mijs, W. J., Liquid-Crystalline Epoxide Thermosets - Dynamic-Mechanical and Thermal-Properties. *Macromolecules* **1995**, *28*, 2201-2211.
- (68) Harada, M.; Ochi, M.; Tobita, M.; Kimura, T.; Ishigaki, T.; Shimoyama, N.; Aoki, H., Thermomechanical Properties of Liquid-Crystalline Epoxy Networks Arranged by a Magnetic Field. *Journal of Polymer Science Part B-Polymer Physics* **2004**, *42*, 758-765.
- (69) Harada, M.; Ochi, M.; Tobita, M.; Kimura, T.; Ishigaki, T.; Shimoyama, N.; Aoki, H., Thermal-Conductivity Properties of Liquid-Crystalline Epoxy Resin Cured under a Magnetic Field. *Journal of Polymer Science Part B-Polymer Physics* **2003**, *41*, 1739-1743.
- (70) Barclay, G. G.; Ober, C. K.; Papathomas, K. I.; Wang, D. W., Liquid-Crystalline Epoxy Thermosets Based on Dihydroxymethylstilbene - Synthesis and Characterization. *Journal of Polymer Science Part A-Polymer Chemistry* **1992**, *30*, 1831-1843.
- (71) Lincoln, D. M.; Douglas, E. P., Control of Orientation in Liquid Crystalline Epoxies Via Magnetic Field Processing. *Polymer Engineering and Science* **1999**, *39*, 1903-1912.
- (72) Tan, C. B.; Sun, H.; Fung, B. M.; Grady, B. P., Properties of Liquid Crystal Epoxy Thermosets Cured in a Magnetic Field. *Macromolecules* **2000**, *33*, 6249-6254.
- (73) Benicewicz, B. C.; Smith, M. E.; Earls, J. D.; Priester, R. D.; Setz, S. M.; Duran,

R. S.; Douglas, E. P., Magnetic Field Orientation of Liquid Crystalline Epoxy Thermosets. *Macromolecules* **1998**, *31*, 4730-4738.

(74)Lind, C.; Coleman, M. R.; Kozy, L. C.; Sharma, G. R., Zirconium Tungstate/Polymer Nanocomposites: Challenges and Opportunities. *Physica Status Solidi B-Basic Solid State Physics* **2011**, *248*, 123-129.

(75)Badrinarayanan, P.; Ahmad, M. I.; Akinc, M.; Kessler, M. R., Synthesis, Processing, and Characterization of Negative Thermal Expansion Zirconium Tungstate Nanoparticles with Different Morphologies. *Materials Chemistry and Physics* **2011**, *131*, 12-17.

(76)Kozy, L. C.; Tahir, M. N.; Lind, C.; Tremel, W., Particle Size and Morphology Control of the Negative Thermal Expansion Material Cubic Zirconium Tungstate. *Journal of Materials Chemistry* **2009**, *19*, 2760-2765.

(77)Colin, J. A.; Camper, D. V.; Gates, S. D.; Simon, M. D.; Witker, K. L.; Lind, C., Zirconium Tungstate Hydroxide Hydrate Revisited: Crystallization Dependence on Halide and Hydronium Ions. *Journal of Solid State Chemistry* **2007**, *180*, 3504-3509.

(78)Dadachov, M. S.; Lambrecht, R. M., Synthesis and Crystal Structure of Zirconium Tungstate  $ZrW_2O_7(OH,Cl)(2)Center\ Dot\ 2h(2)O$ . *Journal of Materials Chemistry* **1997**, *7*, 1867-1870.

(79)Li, T. Q.; Zhang, M. Q.; Zhang, K.; Zeng, H. M., The Dependence of the Fracture Toughness of Thermoplastic Composite Laminates on Interfacial Interaction. *Composites Science and Technology* **2000**, *60*, 465-476.

(80)Banek, N. A.; Baiz, H. I.; Latigo, A.; Lind, C., Autohydration of Nanosized Cubic Zirconium Tungstate. *Journal of the American Chemical Society* **2010**, *132*, 8278-+.

(81)Krynetskii, I. B.; Gizhevskii, B. A.; Naumov, S. V.; Kozlov, E. A., Size Effect of the Thermal Expansion of Nanostructural Copper Oxide. *Physics of the Solid State* **2008**, *50*, 756-758.

(82)Flory, P. J.; Abe, A., Statistical Thermodynamics of Mixtures of Rodlike Particles .1. Theory for Polydisperse Systems. *Macromolecules* **1978**, *11*, 1119-1122.

(83)Flory, P. J.; Ronca, G., Theory of Systems of Rodlike Particles .2. Thermotropic Systems with Orientation-Dependent Interactions. *Molecular Crystals and Liquid Crystals* **1979**, *54*, 311-330.

(84)Vyazovkin, S.; Sbirrazzuoli, N., Mechanism and Kinetics of Epoxy-Amine Cure Studied by Differential Scanning Calorimetry. *Macromolecules* **1996**, *29*, 1867-1873.

(85)Vyazovkin, S.; Sbirrazzuoli, N., Kinetic Methods to Study Isothermal and Nonisothermal Epoxyanhydride Cure. *Macromolecular Chemistry and Physics* **1999**, *200*, 2294-2303.

(86)Sbirrazzuoli, N.; Vyazovkin, S.; Mititelu, A.; Sladic, C.; Vincent, L., A Study of Epoxy-Amine Cure Kinetics by Combining Isoconversional Analysis with Temperature Modulated Dsc and Dynamic Rheometry. *Macromolecular Chemistry and Physics* **2003**, *204*, 1815-1821.

(87)Sbirrazzuoli, N.; Vyazovkin, S., Learning About Epoxy Cure Mechanisms from Isoconversional Analysis of Dsc Data. *Thermochimica Acta* **2002**, *388*, 289-298.

(88)Sbirrazzuoli, N.; Mititelu-Mija, A.; Vincent, L.; Alzina, C., Isoconversional Kinetic Analysis of Stoichiometric and Off-Stoichiometric Epoxy-Amine Cures. *Thermochimica Acta* **2006**, *447*, 167-177.

(89)Vyazovkin, S.; Sbirrazzuoli, N., Isoconversional Kinetic Analysis of Thermally



Stimulated Processes in Polymers. *Macromolecular Rapid Communications* **2006**, *27*, 1515-1532.

(90)Vyazovkin, S., Modification of the Integral Isoconversional Method to Account for Variation in the Activation Energy. *Journal of Computational Chemistry* **2001**, *22*, 178-183.

(91)Jaramillo, R. A.; Babu, S. S.; Ludtka, G. M.; Kisner, R. A.; Wilgen, J. B.; Mackiewicz-Ludtka, G.; Nicholson, D. M.; Kelly, S. M.; Muruganath, M.; Bhadeshia, H. K. D. H., Effect of 30T Magnetic Field on Transformations in a Novel Bainitic Steel. *Scripta Materialia* **2005**, *52*, 461-466.

(92)Nicholson, D. M. C.; Kisner, R. A.; Ludtka, G. M.; Sparks, C. J.; Petit, L.; Jaramillo, R.; Mackiewicz-Ludtka, G.; Wilgen, J. B.; Sheikh-Ali, A.; Kalu, P. N., The Effect of High Magnetic Field on Phase Stability in Fe-Ni. *Journal of Applied Physics* **2004**, *95*, 6580-6582.

(93)Ludtka, G. M.; Jaramillo, R. A.; Kisner, R. A.; Nicholson, D. M.; Wilgen, J. B.; Mackiewicz-Ludtka, G.; Kalu, P. N., In Situ Evidence of Enhanced Transformation Kinetics in a Medium Carbon Steel Due to a High Magnetic Field. *Scripta Materialia* **2004**, *51*, 171-174.

(94)Behl, M.; Razzaq, M. Y.; Lendlein, A., Multifunctional Shape-Memory Polymers. *Advanced Materials* **2010**, *22*, 3388-3410.

(95)Behl, M.; Lendlein, A., Shape-Memory Polymers. *Materials Today* **2007**, *10*, 20-28.

(96)Jiang, H.; Li, C.; Huang, X., Actuators Based on Liquid Crystalline Elastomer Materials. *Nanoscale* **2013**, *5*, 5225-5240.

(97)Ohm, C.; Brehmer, M.; Zentel, R., Liquid Crystalline Elastomers as Actuators and Sensors. *Advanced Materials* **2010**, *22*, 3366-3387.

(98)Seki, T., Meso- and Microscopic Motions in Photoresponsive Liquid Crystalline Polymer Films. *Macromolecular Rapid Communications* **2014**, *35*, 271-290.

(99)Ikeda, T.; Mamiya, J.-i.; Yu, Y., Photomechanics of Liquid-Crystalline Elastomers and Other Polymers. *Angewandte Chemie International Edition* **2007**, *46*, 506-528.

(100)Sanchez-Ferrer, A.; Finkelmann, H., Polydomain-Monodomain Orientational Process in Smectic-C Main-Chain Liquid-Crystalline Elastomers. *Macromolecular Rapid Communications* **2011**, *32*, 309-315.

(101)Agrawal, A.; Chipara, A. C.; Shamoo, Y.; Patra, P. K.; Carey, B. J.; Ajayan, P. M.; Chapman, W. G.; Verduzco, R., Dynamic Self-Stiffening in Liquid Crystal Elastomers. *Nat Commun* **2013**, *4*, 1739.

(102)Ohm, C.; Serra, C.; Zentel, R., A Continuous Flow Synthesis of Micrometer-Sized Actuators from Liquid Crystalline Elastomers. *Advanced Materials* **2009**, *21*, 4859-4862.

(103)Marshall, J. E.; Gallagher, S.; Terentjev, E. M.; Smoukov, S. K., Anisotropic Colloidal Micromuscles from Liquid Crystal Elastomers. *Journal of the American Chemical Society* **2013**, *136*, 474-479.

(104)Yang, H.; Buguin, A.; Taulemesse, J.-M.; Kaneko, K.; Méry, S.; Bergeret, A.; Keller, P., Micron-Sized Main-Chain Liquid Crystalline Elastomer Actuators with Ultralarge Amplitude Contractions. *Journal of the American Chemical Society* **2009**, *131*, 15000-15004.

(105)Küpfer, J.; Finkelmann, H., Nematic Liquid Single Crystal Elastomers. *Die*

*Makromolekulare Chemie, Rapid Communications* **1991**, *12*, 717-726.

(106)Yu, Y.; Nakano, M.; Ikeda, T., Photomechanics: Directed Bending of a Polymer Film by Light. *Nature* **2003**, *425*, 145-145.

(107)Li, M. H.; Keller, P.; Li, B.; Wang, X.; Brunet, M., Light-Driven Side-on Nematic Elastomer Actuators. *Advanced Materials* **2003**, *15*, 569-572.

(108)Lendlein, A.; Jiang, H.; Junger, O.; Langer, R., Light-Induced Shape-Memory Polymers. *Nature* **2005**, *434*, 879-882.

(109)Sánchez-Ferrer, A.; Merekalov, A.; Finkelmann, H., Opto-Mechanical Effect in Photoactive Nematic Side-Chain Liquid-Crystalline Elastomers. *Macromolecular Rapid Communications* **2011**, *32*, 671-678.

(110)Ikeda, T.; Ube, T., Photomobile Polymer Materials: From Nano to Macro. *Materials Today* **2011**, *14*, 480-487.

(111)Yamada, M.; Kondo, M.; Mamiya, J.-i.; Yu, Y.; Kinoshita, M.; Barrett, C. J.; Ikeda, T., Photomobile Polymer Materials: Towards Light-Driven Plastic Motors. *Angewandte Chemie International Edition* **2008**, *47*, 4986-4988.

(112)Yamada, M.; Kondo, M.; Miyasato, R.; Naka, Y.; Mamiya, J.-i.; Kinoshita, M.; Shishido, A.; Yu, Y.; Barrett, C. J.; Ikeda, T., Photomobile Polymer Materials-Various Three-Dimensional Movements. *Journal of Materials Chemistry* **2009**, *19*, 60-62.

(113)Haberl, J. M.; Sánchez-Ferrer, A.; Mihut, A. M.; Dietsch, H.; Hirt, A. M.; Mezzenga, R., Liquid-Crystalline Elastomer-Nanoparticle Hybrids with Reversible Switch of Magnetic Memory. *Advanced Materials* **2013**, *25*, 1787-1791.

(114)Kaiser, A.; Winkler, M.; Krause, S.; Finkelmann, H.; Schmidt, A. M., Magnetoactive Liquid Crystal Elastomer Nanocomposites. *Journal of Materials Chemistry* **2009**, *19*, 538-543.

1.

**1. Report Type**

Final Report

**Primary Contact E-mail****Contact email if there is a problem with the report.**

MichaelR.Kessler@wsu.edu

**Primary Contact Phone Number****Contact phone number if there is a problem with the report**

509-335-8654

**Organization / Institution name**

Washington State University

**Grant/Contract Title****The full title of the funded effort.**

Nano-Zirconium Tungstate Reinforced Liquid Crystalline Thermosetting Composites with Near Zero Thermal Expansion

**Grant/Contract Number****AFOSR assigned control number. It must begin with "FA9550" or "F49620" or "FA2386".**

FA9550-12-1-0108

**Principal Investigator Name****The full name of the principal investigator on the grant or contract.**

Michael Kessler (Washington State University) / Kristen Constant (Iowa State University)

**Program Manager****The AFOSR Program Manager currently assigned to the award**

Joycelyn Harrison

**Reporting Period Start Date**

03/15/2012

**Reporting Period End Date**

03/14/2015

**Abstract**

One crucial factor limiting the performance of polymer matrix composites is their relatively high coefficient of thermal expansion (CTE), which impacts the dimensional stability of these materials. This report described the synthesis and characterization of zirconium tungstate ( $\text{ZrW}_2\text{O}_8$ ) nanoparticles with negative CTE and their applications in an epoxy resin to produce low CTE nanocomposites. This work also described the synthesis and characterization of a unique class of thermosets known as liquid crystalline epoxy resins (LCERs) for the development of advanced polymer matrices for high performance composites. Results showed that it was possible to control structure and the resulting functionality of the LCERs by curing the synthesized epoxy monomer with appropriate curing agents. Highly crosslinked LCERs exhibited a self-reinforcing effect because of the self-organized liquid crystalline phase and are promising candidates for the polymer matrices in structural composites. Lightly crosslinked LCERs exhibited a triple shape memory effect and are excellent candidates for the development of multifunctional polymer composites.

**Distribution Statement****This is block 12 on the SF298 form.**

Distribution A - Approved for Public Release

**Explanation for Distribution Statement**

If this is not approved for public release, please provide a short explanation. E.g., contains proprietary information.

**SF298 Form**

Please attach your [SF298](#) form. A blank SF298 can be found [here](#). Please do not password protect or secure the PDF. The maximum file size for an SF298 is 50MB.

[SF 298.pdf](#)

**Upload the Report Document. File must be a PDF. Please do not password protect or secure the PDF. The maximum file size for the Report Document is 50MB.**

[AFOSR final report.pdf](#)

**Upload a Report Document, if any. The maximum file size for the Report Document is 50MB.**

**Archival Publications (published) during reporting period:**

1. H. Wu, P. Badrinarayanan, M. R. Kessler, "Effect of Hydrothermal Synthesis Conditions on the Morphology and Negative Thermal Expansivity of Zirconium Tungstate Nanoparticles", Journal of the American Ceramic Society, 2012, 95(11), 3643-3650.
2. Y. Li, P. Badrinarayana, M. R. Kessler, "Liquid Crystalline Epoxy Resin Based on Biphenyl Mesogen: Thermal Characterization", Polymer, 2013, 54(12), 3017-3025.
3. Y. Li, M. R. Kessler, "Liquid Crystalline Epoxy Resin Based on Bisphenol Mesogen: Effect of Magnetic Field Orientation during Cure", Polymer, 2013, 54 (21), 5742-5746.
4. H. Wu, M. Rogalski, M. R. Kessler, "Zirconium Tungstate/Epoxy Nanocomposites: Effect of Nanoparticle Morphology and Negative Thermal Expansivity", ACS Applied Materials and Interfaces, 2013, 5(19), 9478-9487.
5. Y. Li, M. R. Kessler, "Cure Kinetics of Liquid Crystalline Epoxy Resins Based on Biphenyl Mesogen", Journal of Thermal Analysis and Calorimetry, 2014, 117(1), 481-488.
6. Y. Li, M. R. Kessler, "Creep-resistant behavior of self-reinforcing liquid crystalline epoxy resins", Polymer, 2014, 55(8), 2021-2027.
7. Y. Li, O. Rios, M. R. Kessler, "Thermomagnetic Processing of Liquid Crystalline Epoxy Resins and Their Mechanical Characterization Using Nanoindentation", ACS Applied Materials and Interfaces, 2014, 6(21), 19456-19464.
8. Y. Li, C. Pruitt, O. Rios, L. Wei, M. Rock, J. K. Keum, A. G. McDonald, M. R. Kessler, "Controlled Shape Memory Behavior of a Smectic Main-chain Liquid Crystalline Elastomer", Macromolecules, 2015, 48(9), 2864-2874.

**Changes in research objectives (if any):**

**Change in AFOSR Program Manager, if any:**

**Extensions granted or milestones slipped, if any:**

**AFOSR LRIR Number**

**LRIR Title**

**Reporting Period**

**Laboratory Task Manager**

**Program Officer**

**Research Objectives**

**Technical Summary**

**Funding Summary by Cost Category (by FY, \$K)**

	Starting FY	FY+1	FY+2
Salary			
Equipment/Facilities			
Supplies			
Total			

**Report Document****Report Document - Text Analysis****Report Document - Text Analysis****Appendix Documents****2. Thank You****E-mail user**

Jun 15, 2015 01:00:12 Success: Email Sent to: MichaelR.Kessler@wsu.edu